A probabilistic graphical framework fusing data for model updating and decision support

by

Mark Daniel Groden

A dissertation submitted in partial fulfillment
of the requirements for the degree of
Doctor of Philosophy
(Naval Architecture and Marine Engineering)
in the University of Michigan
2016

Doctoral Committee:

Assistant Professor Matthew D. Collette, Chair
Associate Professor Dale G. Karr
Professor Romesh Saigal
Assistant Professor David J. Singer

ACKNOWLEDGEMENTS

I would first like to thank Dr. Matthew Collette whose mentorship, guidance, and support were absolutely critical to my development during my studies. Dr. Collette began working with me in 2009 as an undergraduate sophomore and mentored me through my undergraduate studies, internship opportunities, extracurricular involvements, and transition to graduate school–all the while guiding me academically. His consistent, calm, and trusting demeanor were all invaluable to me during my development.

In addition to my advisor, I would like to thank the rest of my thesis committee: Dr. Dale Karr, Dr. Romesh Saigal, and Dr. Dave Singer for their encouragement and insightful comments. I would like to thank Dr. Ulrik Dam Nielsen for hosting and advising me during my stay at Denmark Technical University. Also, I would like to acknowledge the support of Dr. Paul Hess of the Office of Naval Research code 331.

TABLE OF CONTENTS

LIST OF FIGURES

LIST OF TABLES

LIST OF ABBREVIATIONS

CDF Cumulative Distribution Function

CPT Conditional Probability Table

DAG Directed Acyclic Graph

DBN Dynamic Bayesian Network

BN Bayesian Network

DID Dynamic Influence Diagram

FORM First Order Reliability Method

PDF Probability Density Function

PPSS Passive Peak Strain sensor

SAS Strain Amplification Sensor

VBM Vertical Bending Moment

D2D Data to Decision

ID Influence Diagram

RBI Risk Based Inspection

FPSO Floating Production Storage and Offloading

DCS Damage Control System

KDSS Knowledge-based Decision Support System

MHDSS Method-Based Decision Support System

RMS Root Mean Square

SWBM Still Water Bending Moment

Cb Block Coefficient

DAQ Data Acquisition System

FDS Fatigue Damage Sensor

CPT Conditional Probability Table

ABSTRACT

A probabilistic graphical framework fusing data for model updating and decision support

by

Mark Daniel Groden

Chair: Matthew D. Collette

There is significant uncertainty in assessing the structural health and capabilities of a marine structure during both service life and after sustaining damage. Design-stage marine structural engineering models offer limited information on the as-built structure's health during service life. Despite copious amounts of data provided by structural monitoring techniques, synthesizing these different data types to update the design-stage models remains challenging. A novel decision support graph was created by extending a parametrically encoded Bayesian network (BN) data fusion framework to influence diagrams for Data to Decision (D2D). The D2D framework combines observational and sensor through-life data to update the design-stage models. Once updated, these models provide predictions of future structural health and safety, decision support for inspection timing and extent, and decision support to emergency response teams for survival and mission objective satisfaction strategies.

To demonstrate the effectiveness of the BN parametrically encoded data fusion, a lognormal probabilistic fatigue initiation model was developed for a series of large stiffened metallic grillages; grillages consist of identical fatigue-critical details typical of vessel and platform structures. Monte-Carlo simulations were used to compare the BN's prognosis with the synthetic data. Evidence for inference includes data acquired from visual inspection, operating conditions, and an innovative stand-alone mechanical strain sensor, the Strain Amplification Sensor (SAS), developed as a part of this work. Results demonstrated that the BN produces better estimates for fatigue crack initiation through addition of various pieces of evidence. Successful prognosis led to the adaptation of the network to provide inspection guidance, and to aid in decision-making given a damaged marine structure.

CHAPTER 1

Introduction

Ninety percent of world trade by value is carried by the international shipping industry. And despite being the oldest form of cargo transport, it is still the most cost-effective method, measured by cargo weight per distance traveled. This is partially owing to the immense size of modern vessels which are often greater than 1000 feet long. Their immense size enables the movement of cargo with economies of scale unmatched by other methods of transport. The combination of exceptional length and increasingly lightweight structures produced with high tensile strength steel leads to some particular challenges in structural reliability. Recently, the MOL *Comfort*, a 1037 ft.-long container ship launched in 2008 had a catastrophic hull structural failure just five years into its expected forty-year life cycle, figure 1.1. Events like the *Comfort* disaster serve as a reminder that there is still a knowledge gap that needs to be addressed.

The problem of sensing, performing model updating, and determining the condition analysis of marine structures has been well studied over the past decade Salvino and Collette (2009). The ability to process the large amounts of data generated by monitoring systems and intelligently update models continues to be an active area of development for the marine community. One of first investigations was presented by Guedes Soares and Garbatov (1999), where a time variant formulation for reliability assessment updated by repair and accounting for corrosion and fatigue was developed. More recently, several authors have proposed frameworks for interpreting monitoring data and updating underly-

Figure 1.1: MOL Comfort broken in half of the coast of Yemen, June 17, 2013, gCaptain (2014)

ing performance models. Salvino, Farrar, Lynch, and Brady (2009) proposed a multi-tier framework for integrating monitoring data readings and prediction models for naval vessels. Extending the initial work of Salvino et al. (2009) a data-to-decision framework has recently been presented for marine structures Collette and Lynch (2013).

Using Bayesian inference to build a multivariate PDF, Zrate, Caicedo, Yu, and Ziehl (2012) presented a framework to update and predict crack length as a function of the number of cycles in structural elements subjected to fatigue. Crack length prognosis in this model is for a specific test specimen and the updating technique heavily relies on an accurate posterior stress intensity factor. Similarly, Straub (2009) proposed a Dynamic Bayesian Network (DBN) to characterize the stochastic deterioration process and determine the reliability of structural elements from updating with propagated crack lengths. Also using Bayesian analysis, Meulen and Hageman (2013) predicted fatigue accumulation using data from Fatigue Damage Sensor (FDS)s. FDSs consist of a notched sensing foil mounted to a base foil which is either spot welded or glued to the location in consideration. It has been shown that through visual inspection of the sensing foil's crack propagation that an accurate stress time history is recorded within the sensor and ultimately has been used to predict fa-

tigue lifetime estimates within 20% of those produced by traditional strain sensors and rain flow counting methods. Stull, Earls, and Koutsourelakis (2011) developed a general computational framework to enable model-based hull structural monitoring using large scale and scope condition assessment problems. Similarly, by combining BNs and structural reliability methods Straub and Der Kiureghian (2010) created a computational framework for reliability and risk analysis of engineering structures for application to decision support in near-real-time under evolving information.

Further application of BNs in the realm of Risk Based Inspection for fatigue damages has been completed by Goyet, Rouhan, L'Haridon, and Gomes (2011) who introduced a Probabilistic System Approach including economical optimization of the Floating Production Storage and Offloading (FPSO) service life based on a hierarchical model of the hull and used BNs to propagate probabilities from component level to the system level.

Heredia-Zavoni, Silva-Gonzalez, and Montes-Iturrizaga (2008) presented a general framework for integrity management of offshore steel structures allowing for the risk based planning of inspection and maintenance activities accounting for both deterioration and damage processes using a BN for decision-making. The proposed Risk Based Inspection (RBI) framework combines damage processes and uses a threshold acceptable total system failure probability to dictate optimal inspection points. Sorensen (2011) explored the use of Bayesian pre-posterior decision theory to evaluate deterioration from various sources being monitored and inspected. Further supporting the use of BNs in application to RBIs of vessel structural health, Tammer and Kaminski (2013) reviewed the use of this methodology for determining the inspection scope, and inspection intervals of FPSOs in application to fatigue related degradation, determining it to have an inevitable role in future decision-making. Although there has been application of Bayesian statistics for evaluation of structural health and inspection periodicity, use of BNs and Influence Diagram (ID)s for synthesis of multiple data types for structural health model updating and decision-making has not been explored. Leveraging data fusion–the process of integrating multiple stochastic data

types and sources representing the same real-world object into a consistent, accurate, and useful representation Klein (2007)–is presently being overlooked.

While collecting data to analyze the structural degradation of a vessel is challenging during its life-cycle, it is an even greater challenge in the moments after an incident. Vessel crews are required to respond rapidly to address the damage state, and, if possible, mitigate the risk of losing the vessel. Assuring vessel stability is typically the primary concern as capsize inevitably leads to sinking. Next most important, and often strongly coupled to stability, is the structural state. Loss of structural integrity as was observed in the case of the MOL *Comfort* also leads to an inevitable loss of the ship. In the case of the grounding of the HMS *Nottingham*, shoring of the forward engine room bulkhead maintained the vessel stability and ultimately saved the ship. Damaged compartments were flooded and subsequently sealed, leaving the crew with very limited data for subsequent decision-making. The ability to fuse post-damage visually inspected structural data gathered with significant uncertainty for decision support does not currently exist. Further, a rapidly deployable sensor to measure strain on damaged or undamaged components to aid in post-damage assessment, also, does not exist.

Using DBNs, data synthesis can be performed in real-time. Presently, Damage Control System (DCS)s are designed to pass information to the crew in the event of fire or flooding, however, their extension to decision support systems to ensure the safety and operational stability of modern ships is limited Calabrese, Corallo, Margherita, and Zizzari (2012). These systems primarily address stability Bole (2007) and there is a lack of investigation into support for a damaged vessel's route planning. A hybrid Knowledge-based Decision Support System (KDSS) was presented by Calabrese et al. (2012) for management of crew endangering events. Pollution prevention and risk were investigated by Balmat, Lafont, Maifret, and Pessel (2011) using a fuzzy logic approach. To manage stability in the event of flooding Hu, Ma, and Ji (2013) presented a M-H Method-Based Decision Support System (MHDSS) to provide real-time decision-making assistance. Present work does not address

a vessel's structure in DCS decision support strategies and a D2D framework does not exist.

1.1 Motivation

From design, to as-built, to in-service, a vessel's structural condition becomes increasingly less certain. Damage to the ship's structure during its service-life further compounds this uncertainty. Not only is an accurate understanding of a vessel's structure critical to its operational safety, it can also expand its operational capabilities and yield cost-reducing maintenance decisions. Service life extension and deployment directly rely upon an accurate understanding of the state of structural health. Further, in the event of damage, accurate structural assessment is critical to the decision-making that ensues in the moments after the event and up until the vessel is repaired. Decisions presently are made with limited information pertaining to the present and future vessel state.

Our ability to sense and record structural performance characteristic data has improved dramatically over the past several decades by using new sensor and data acquisition systems Wang, Lynch, and Sohn (2014). These new systems afford the user with high accuracy and sampling rates; however, we are left with a plethora of data but remain thirsty for information Collette and Lynch (2013). Additionally, these new sensing systems are not well suited for application to details within the expansively located set of watertight compartments that make up a marine structure. Thus, we are left with two major challenges. First, develop a framework to interpret and synthesize data related to structural reliability characteristics of a vessel during its operation. This framework should ideally be capable of accurate updating with evidence that need not be acquired by the monitoring systems unsuitable for marine application. Second, should the framework require updating with evidence that cannot be ascertained from physical, visual observation, develop a sensing method that provides data to the framework for more accurate updating while being compatible with the marine structure's particular configuration and operating requirements.

1.2 Research Overview

Using the BN framework, a data fusion approach is developed to interpret the evidence observed from a deteriorating ship. Deterioration can be characterized as that which occurs during the normal operational profile throughout the life cycle or that which occurs much more rapidly after the vessel's structure has undergone significant damage. Common-cause failures and fleet operation enable the network technique to be adapted to either deterioration case.

During evaluation of the updating power from visually observable permanent set, it was discovered that for the pressure regime in which permanent set is not experienced, that there lacks sufficient model updating power. This led to the development of a measurement instrument, SAS, that can record the maximum experienced strain on a marine structure with minimal installation and operational requirements.

1.3 Research Contribution

In this dissertation, a framework for interpreting evidence acquired with uncertainty from different observations to produce a more accurate understanding of underlying design-stage engineering models has been proposed. Considered evidence comprises only of physical observation and a novel strain gauge invented herein for marine structural monitoring. The more accurate engineering models produced for assessing structural reliability are leveraged during the vessel's service life for inspection decision-making and post-damage for route planning decision-making. Structural reliability focused on fatigue life characteristics are used in both the route planning method, damaged state, and in the risk based inspection approach as a proxy for safety. The fatigue approach was based on both stress life (S-N) and fracture mechanics. The primary contributions of this thesis can be summarized as:

1. A fleet-wide structural monitoring data fusion D2D technique is developed utilizing parametrically encoded BNs to synthesize distinct physical structural observation

and sensor input for structural reliability prognosis and maintenance decision support. This framework represents the first time successful data fusion has been shown. Leveraging common-cause failures such as corrosion or cyclic loading, it is possible to synthesize observation of the resulting degradation mechanisms for one vessel and across vessels operating in a fleet. Static BNs for each vessel within the fleet are established at both the present point in time from which evidence is acquired and a future point at which inspection is being considered. Using Monte Carlo simulated data as evidence to varying numbers of ships within the fleet, for those ships which evidence is not provided, the updating accuracy is assessed and demonstrated significant updating power and data synthesis capability.

2. A D2D data fusion framework is developed which produces real-time decision-making support for route planning after sustaining damage. This fusion framework represents the first post-damage decision support tool accounting for structural integrity. Amalgamating the before damage structural state with both operating conditions and post-damage assessment from the rapidly deployable strain gauge invented and developed herein, the novel data fusion technique is extended for real-time decision support. The BN framework is extended from static to dynamic; and by addition of decision and utility nodes creates a Dynamic Influence Diagram (DID). Evidence is provided from physical observation of deterioration by way of crack growth, with measurement uncertainty, and the strain gauge data. Data fusion capabilities are demonstrated from common-cause visually observable failures and by way of multi-ship synthesis.

3. Invention and testing of SAS for integration into the above-mentioned frameworks Groden and Collette (2016b). The SAS is the first completely 3D printable strain gauge. It is mechanical, stand-alone, cost-effective, rapidly deployable, non-destructive and capable of recording real-time and maximum experienced strain about multiple

axes with optical data output requiring no electrical input or data acquisition system. The same characteristics that make SAS well suited to the shipboard environment are also valuable in the fabrication process in the shipyard. SAS was tested to measure residual stress and distortion during and after weld processes benchmarked against conventional piezoelectric strain gauges.

CHAPTER 2

Background of Bayesian Methods

2.1 Introduction

The data synthesis framework explored throughout this body of work relies upon BNs and their extension to IDs as a decision support tool. This chapter aims to introduce BNs, their construction, updating approaches, extension to Influence Diagrams, and finally utility function construction which Influence Diagrams heavily rely upon.

2.2 Bayesian Networks

A BN is a probabilistic graphical model representing a set of random variables and their conditional dependencies via a Directed Acyclic Graph (DAG) compactly encoding full joint probability distributions Kjaerulff and Madsen (2008). Random variables are represented by nodes connected by edges indicating the flow and direction of conditional dependence. The causal relationship between variables represented by nodes is easily ascertained from the graph. Figure 2.1 demonstrates a simple BN model to determine the probability of being late for work. It can be seen that being late for work is dependent upon the probability of missing the bus, rising late, alarm clock failure, and oversleeping.

Each node contains a Conditional Probability Table (CPT) including the probabilities that the random variable represented by the node assumes each of its possible states given

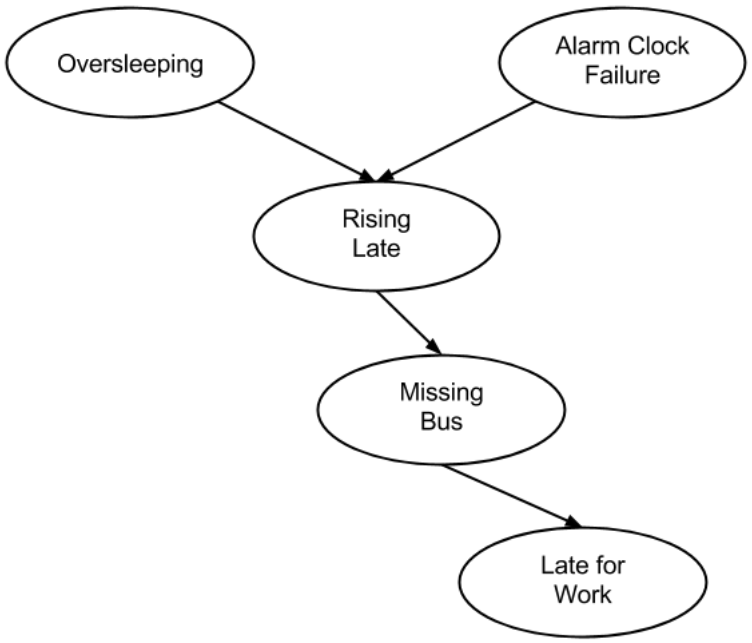

Figure 2.1: BN example

all combinations of its parent nodes. For example, the alarm clock failure and oversleeping are parent nodes to getting up late.

Example CPTs for the network are provided in tables 2.1 through 2.5.

Alarm Clock Failure	
Yes	0.5
No	0.5

Table 2.1: Oversleeping CPT

Oversleeping	
Yes	0.1
No	0.9

Table 2.2: Alarm Clock Failure CPT

BNs are fundamentally based on Bayes' theorem which include likelihood, prior, and

		Rising Late	
Oversleeping	Alarm Clock Failure	Yes	No
Yes	No	0.9	0.1
Yes	Yes	1	0
No	No	0.05	0.95
No	Yes	0.8	0.2

Table 2.3: Rising Late CPT

	Rising Late	
Missing Bus	Yes	No
Yes	0.7	0.2
No	0.3	0.8

Table 2.4: Missing Bus CPT

	Missing Bus	
Late for Work	Yes	No
Yes	0.9	0.3
No	0.1	0.7

Table 2.5: Late for Work CPT

conditional probabilities to produce the posterior probability.

$$P(A|B) = \frac{P(B|A)P(A)}{P(B)} \tag{2.1}$$

Using the chain rule, equation 2.2, we can find the probability density function for any random variable for an assumed state using the defined conditional probability tables. If we consider random variables A and B to be parent nodes to variable C we can find a probability density function for any state of C.

$$P(A_n, ..., A_1) = P(A_n|A_{n-1}, ..., A_1) * P(A_{n-1}, ..., A_1) \tag{2.2}$$

$$P(C) = \sum_B \sum_A P(A, B)P(B|A)P(A) \tag{2.3}$$

2.3 Bayesian Inference

Realizing the utility of a BN requires inference. Inference of a BN is an NP-hard problem Cooper (1990) with many solution algorithms. This work utilizes the *HUGIN Expert* software package which employs the junction tree algorithm, one of the most widely used exact inference algorithms developed by Jensen, Lauritzen, and Olesen (1990) and Lauritzen and Spiegelhalter (1988). Using message passing derived from the network structure the junction tree algorithm achieves efficient inference over large networks. Madsen and Jensen (1999) go into great depth describing the construction of the junction tree algorithm which can be concisely explained by the following steps:

1. Moralize the graph. A moral graph is one without directed edges. All directed edges are thereby changed to undirected. Additionally, if an edge does not already connect a set of parents, an undirected edge is added between them.

2. Create clusters. This step is known as triangulation and produces the structure which

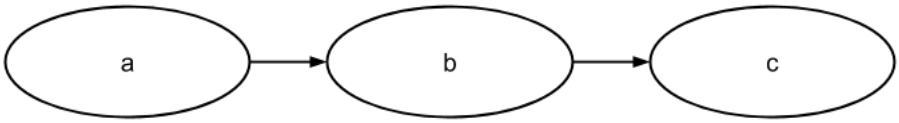

Figure 2.2: Simple BN

can be used for propagation for all information scenarios. By determining the node with minimum weight, its neighbors and itself become a cluster. Once the cluster is identified, the node with minimum weight is removed and process is repeated until no nodes remain. A node's weight is defined as the number of edges that need to be added to its neighbors to ensure that a complete subgraph is created. A subgraph is one in which every pair of distinct nodes is connected by an edge. Finally, a subgraph must not be contained in any larger complete subgraph.

3. Creation of a junction tree. All clusters that are a subset of another cluster are removed from the list of clusters. The remaining clusters (n) are then connected by $(n-1)$ edges governed by coinciding subsets. A subset between two clusters is required to establish an edge. Separators are established as common subsets between the clusters. Each edge between clusters includes an intermediate separator chosen as the largest subset between the adjacent clusters.

4. Propagation in junction tree. By message passing between clusters, evidence is collected and distributed throughout the framework. Marginal distributions for each node are established by using the the cluster's potential and assembly of incoming messages. Thereby the posterior distribution of each node is determined.

Propagation is the most involved on the steps and the *HUGIN* Software relies on the so called *HUGIN* architecture which is very time efficient Jensen et al. (1990). To understand how this works we will consider a simple BN as depicted in figure 2.2.

The junction tree of the above BN can be seen in figure 2.3 where the rectangular node is the separator and the two ovular nodes are clusters. We will denote the cluster comprising

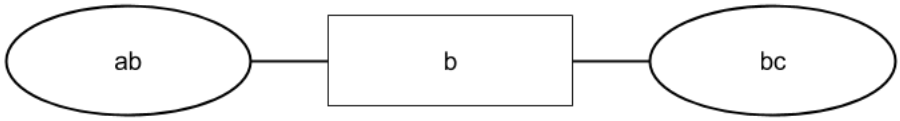

Figure 2.3: Simple BN's junction tree

of a and b as cluster x and the cluster comprising of b and c as y; the separator comprising of b will be denoted as separator s. A potential field is defined as a function over a set of variables where an instantiation of these variables is mapped to a non-negative number. To establish the basis for message passing between the clusters x and y we must establish the potential tables, which are defined as:

$$\psi_x = P(B|A)P(A) \tag{2.4}$$

$$\psi_y = P(C|B) \tag{2.5}$$

If evidence is observed on one of the random variables, we must account for this in the potential tables. For example, if evidence is observed on either node b or node c, we must update the cluster, x and the potential s accordingly. These can be obtained:

$$\psi_x^* = \psi_x \frac{\phi_s^*}{\phi_s} \tag{2.6}$$

$$\phi_s^* = \sum_{w/s} \psi_y \tag{2.7}$$

Where $*s$ indicate updated potentials. Updated probabilities can then be found from their associated clusters:

$$P(A) = \sum_B \psi_x^* \tag{2.8}$$

$$P(B) = \sum_C \psi_y^* \tag{2.9}$$

$$P(C) = \sum_{B} \psi_y^* \tag{2.10}$$

Message passing within a junction tree requires the collection of evidence and the distribution of evidence, which are done in separate steps. Clusters may only send a message after they have received messages from all of their neighbors. The passed separator potentials are combined with the potentials of clusters to which they are passed. Their combination can then be passed onward until the message reaches the cluster containing the random variable being queried. Full propagation is completed after this collection and distribution of evidence is performed. For queries on random variables other than the initial, the joint probability distribution on the cluster containing the variable can be found by joining its incoming messages and the cluster's potential.

The difficulty in solving the junction tree algorithm can be characterized by the size of the conditional probability tables on each of the random variable nodes which grow exponentially with the number of parents, the number and length of each cycle in the junction tree graph and the use of continuous or discrete random variable nodes. This is because evaluation of the junction tree requires the computation of the posterior probability distributions for all random variable nodes given the evidence, the probability of the evidence set, and the joint probability distributions.

2.4 Bayesian Networks to Interpret Structural Monitoring Data

2.4.1 Bayesian Network Construction

The BN in figure 2.4 is called a diverging connection. This means that evidence from either child node may be transmitted through the parent so long as the state of the parent is not known. If both edges were reversed, the connection would be converging and evidence can only be transmitted if ΔS or a descendant is the variable on which it was observed. If

one edge were reversed, the connection would be serial. Here evidence can be transmitted unless the state of ΔS is known. By using diverging connections, data synthesis is readily facilitated for underlying characteristics using probabilistically dependent observations. It is important to recognize that data flow from evidence within a BN is therefore not governed by the direction of the edges. The connection type and location of the evidence observed within the DAG structure govern the flow of data through the network. Edge direction only indicates causality.

The goal of the BNs within this work are to develop revised parameter estimates of the independent variables from the structural models being encoded. A parametric encoding technique was used within this work. Parametric encoding requires far fewer observations than non-parametric methods in order to accurately estimate the underlying distribution James, Witten, Hastie, and Tibshirani (2013). Additionally, the variable ranges modeled by parametric encoding are larger, increasing the considered space. Inspection evidence is provided to the network to update the independent structural model parameters through inference; a more accurate representation of the reliability model is realized for prognosis and decision support.

2.4.2 Structural Health Monitoring Data Synthesis

BNs afford the user with great flexibility in data synthesis and forecast updating from observations with and without certainty. Bayes' rule provides the basis to determine the degree of belief in a hypothesis based on the considered evidence. Providing a BN with evidence and performing inference produces a set of posterior probability distributions for the related variables. These posterior distributions represent hypothesis beliefs for the applied evidence and can be used to reassess the distributions for the nodes on which evidence is applied. Thus, if a considered structural degradation mechanism is considered a child node of some set of structural characteristics, when evidence is observed and provided to the network's degradation node, the structural characteristics' distribution driving the degradation

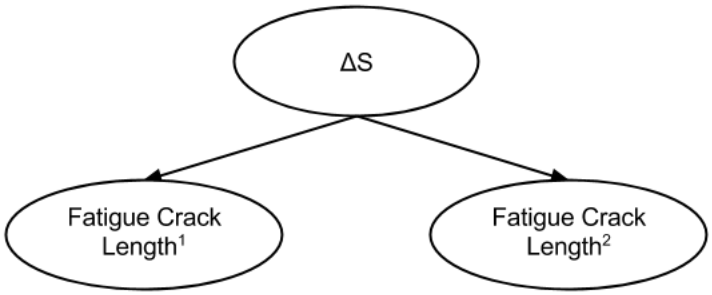

Figure 2.4: BN demonstrating structural reliability prognosis capability

is updated to better reflect the present state of the vessel's structure. Some of these characteristics are time-invariant which improves the prognosis of the framework significantly. Figure 2.4 depicts this phenomenon simply. The stress range probability distribution governing fatigue crack length is time-invariant. Observation of the fatigue crack length at the first timestep produces, through inference, an updated distribution for ΔS, which yields a more accurate prognosis of crack length at the future timestep given a number of expected cycles of stress.

Revised parameter estimates can be achieved through updating with one observed piece of evidence such as crack length or can be updating with multiple pieces of evidence, as can be seen in figure 2.5. Permanent set is a result of the extreme stress placed on a member. Thus, there is causality from the underlying stress range distribution and the observed permanent set. Using inference once again, the distribution of the stress range is updated, but with both pieces of evidence to further improve the underlying actual in-service stress distribution. Thereby, the BN framework serves as a tool for synthesizing pieces of evidence with uncertainty.

2.5 Dynamic Bayesian Networks

Adapting the BN framework to model a dynamic system requires a special class of BNs called DBNs. Dynamic systems operating with real-time feedback require adaptation of

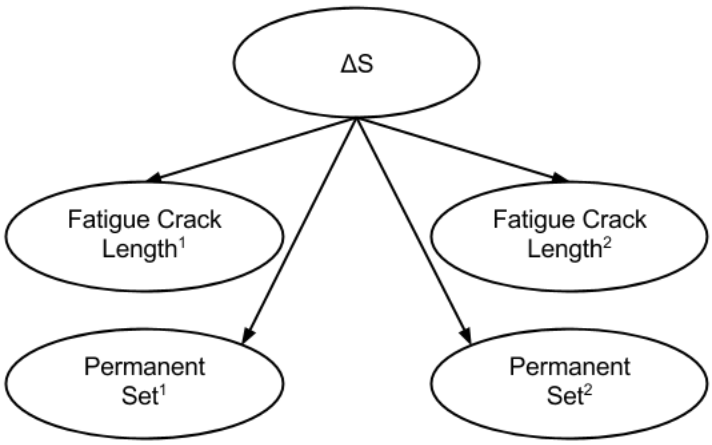

Figure 2.5: BN demonstrating structural reliability prognosis capability with data synthesis from permanent set and fatigue crack length

the conventional DAG to produce relevant information. A DBN interprets multiple past static networks and as time progresses, adds new networks for each time slice.

Each timestep's static network relates random variables to their adjacent timestep static networks. Links between variables to adjacent time-slices are know as temporal links. The interface of a time-slice is considered the set of variables that have parents in the previous time-slice. For example, in figure 2.6, variables a and b are both considered a part of the interface and the edges which connect them are temporal links.

This depicted representation is known as unrolling the dynamic model for the desired number of timesteps. For a given point in time a DBN is static as it consists of a discrete set of static networks representing all past time slices and future points in time for which a prognosis is desired. Once the network is unrolled, conventional inference approaches such as junction tree may be applied. Within this work the *HUGIN Expert* engine is based upon an unrolling technique with junction tree inference.

After unrolling, smoothing, filtering, and prediction are solved with inference algorithms such as the junction tree. Smoothing is the process of querying about the state of the system at a previous timestep given evidence about the system at the current timestep, filtering is the process of querying about the state of the system at the current time, and pre-

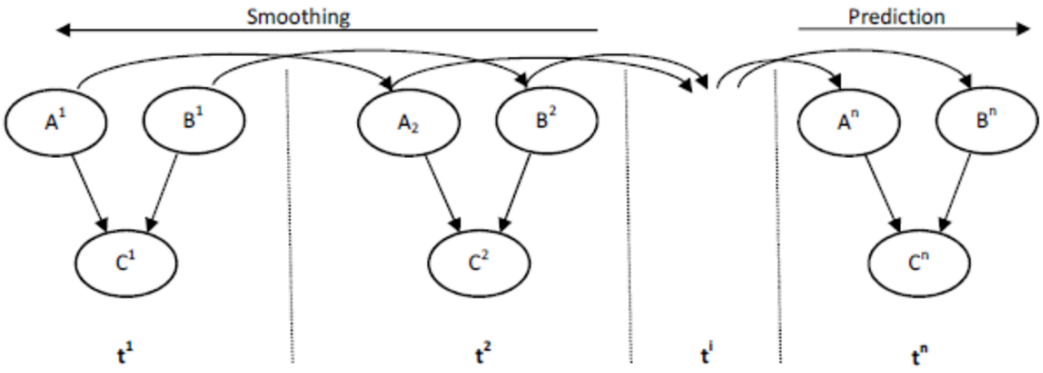

Figure 2.6: Dynamic BN time slice model

diction is the process of querying about the state of the system at a future timestep Kjaerulff and Madsen (2008), Shachter (1988), Tatman and Shachter (1990). Figure 2.6 depicts the unrolling of a basic DBN and the relationships with smoothing and prediction. Alternative inference techniques are available that can solve a DBN analytically. When all of the CPTs are linear Gaussian, Bayesian linear regression Carlin, Louis, and Carlin (2009) or a Kalman filter can be utilized for an analytical solution Kalman (1960). Additionally, more advanced methods providing ”online inference” that can solve DBNs efficiently for many timesteps using constant memory were introduced by Murphy (2002). Should the number of network timesteps become intractable for the unrolling technique, Murphy’s method can be employed.

As was demonstrated in section 2.4.2, the BN framework allows for data synthesis and input of inspection evidence for more accurate prognosis. For situations where evidence is observed in real-time, such as post-damage states, a DBN is well suited to capture and synthesize the data. By modeling crack growth parameters and crack growth itself within a DBN framework, evidence can be applied when it is observed and subsequent predictions can be updated in real-time.

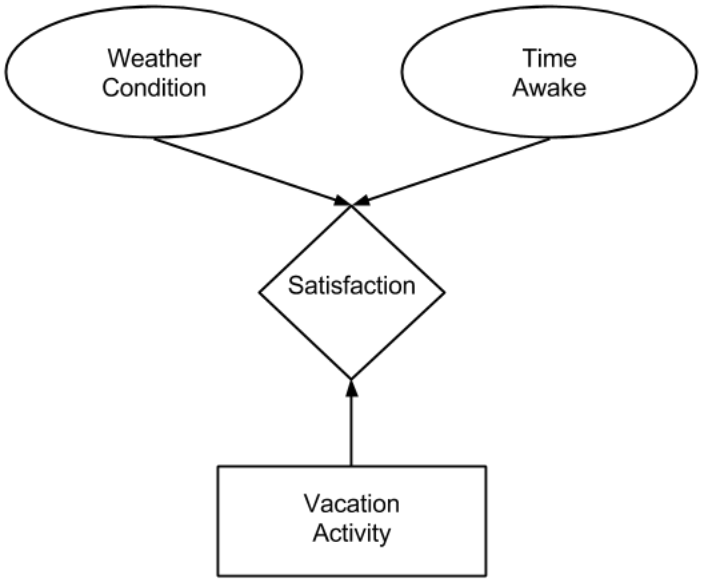

Figure 2.7: Example Influence Diagram

2.6 Influence Diagrams

Through the addition of utility functions and decision nodes, it is possible to use BNs as a decision support tool. Networks augmented with the utility and decision nodes are known as IDs and are compact representations of a joint expected utility function. The solution to a decision problem is a matter of determining the strategy that will provide the highest expected utility value to the decision maker Kjaerulff and Madsen (2008). Therefore, construction of a utility function accurately representing the value of the potential strategies is critical to the effectiveness of the ID's ability to provide decision support. An ID is a BN augmented with utility functions and decision nodes represented by diamond and rectangular shapes respectively, figure 2.7.

To properly construct an influence diagram, it is important to recognize that they model a decision scenario with a fixed sequence of decisions and a single decision maker. Edge direction is critical to the model and the sequence being considered, namely:

- Any time an edge places a decision node as a child, the nodes serving as its parents

must be known prior to making the decision

- When an edge places a decision node as a parent of a random variable node, this as per conventional BN construction indicates probabilistic dependence
- Edges placed into a utility node again indicate functional dependence

Similar to a BN, IDs rely on the chain rule for finding the expected utility as can be seen below. This demonstrates that an ID is a high level specification language for decision trees and a representation of a joint expected utility function.

$$EU(a_i) = \sum_j U(a_i, h_j) P(h_j|\epsilon) \tag{2.11}$$

Strategies are encoded by the potential states of each BN decision node. Utility functions provide a utility value for each combination of related node states. Once the maximum expected utility value is determined, the corresponding strategy states are selected and presented as the optimal decision given the evidence provided.

$$a^* = argmax EU(a) \tag{2.12}$$

Where a^* is the option which maximizes the expected utility and a is a decision belonging to the set of possible options A.

To solve an influence diagram, the $\sum -max - \sum -rule$ is used. This works by first eliminating the decision variables by maximization and then eliminating the chance variables by summation. One decision is solved at a time, thus, the network is effectively rolled-back and collapsed. Where U_D is a universe of decision variables and U_C is a universe of random variables. D_1 through D_n are the decisions existing within the framework and EU is the expected utility. $\hat{\Delta}$ is the optimal strategy which consists of one optimal policy for each decision. x_0 is the set of variables observed initially, x_i is the set of variables observed after D_i and before D_{n+1} and x_n is the set of variables never observed or

observed after D_n.

$$EU(\hat{\Delta}) = \sum_{x_0} max_{D_1} \sum_{x_1} max_{D_n} \cdots \sum_{x_n} EU(U_D, U_C) \tag{2.13}$$

The results of this method provide the user with a set of optimal policies given all combinations of evidence and a set of expected values for decisions made given any combination of evidence. Both of these can be particularly useful. In the case of decision-making in a disaster situation requiring rapid computation, the set of optimal policies can simply be parsed given the evidence data. This is of course assuming that the utility function and network structure were established prior to the event and adequately model the preferences of the situation. Expected utility values for chosen decisions are useful when determining the utility function construction and the network structure as a whole. For differing utility function constructions and weights, the distribution of expected value can be observed across all decision combination and the network behavior can be more rapidly understood. Iterating through tuning parameters and configurations can be performed more effectively by using these values as indicators.

2.7 Utility Function Construction

In order to construct an ID that serves to support decision-making, it is necessary to create a utility function that accurately represents the decision maker's preferences. Preferences are captured in a utility function which assigns a value to represent a given state of each attribute affecting utility. For models with more than one attribute, multi-attribute utility theory needs to be considered. If uncertainty is present in the attribute domains, there are additional characteristics of the utility function that need to be evaluated for independence.

In this body of work all of the utility functions are developed as a part of an Influence Diagram which is based upon a BN, thus, all attributes that are a part of the utility have uncertainty. Additionally, in all cases within these network structures utilities are

evaluated with multiple attributes. Therefore, it is necessary to consider rules governing multi-attribute preferences under uncertainty. Within utility theory, these characteristics pose the most mathematically complex type to consider and also the most restrictive in construction nature.

Utility function independence conditions include preferential independence, utility independence, and additive independence in order of increasing rigor. For sets of additive independence, preferential independence, and utility independence assumptions among the attributes $X_i; i = 1, ..., n$, imply a utility function of the form:

$$U(X_1, X_2, ...X_n) = f(u_1(x_1), u_2(x_2), ...u_n(x_n)) \tag{2.14}$$

Where x_i is a specific amount of X_i, f is a scalar valued function and u_i is a utility function over X_i, Keeney and Raiffa (1993).

Preferential independence is the most basic of the independence conditions and can be defined as follows. Two attributes, X_1 and X_2, are preferentially independent of a third attribute, X_3, if the preference between the outcomes $< x_1, x_2, x_3 >$ and $< x'_1, x'_2, x_3 >$ does not depend on the particular value x_3 of attribute X_3, Russell, Norvig, and Davis (2010).

Utility independence is slightly more restrictive than preferential independence with an extension to lotteries. For utility functions validity assurance with uncertainty in attribute domains this extension to lotteries is critical. Two attributes, X_1 and X_2, are utility independent if the preference between lotteries on attribute X_1 is independent of the particular values of the attribute X_2.

Finally, additive independence is the most restrictive of independence conditions. Two attributes X_1 and X_2 are additive independent if the paired preference comparison of any two lotteries, defined by two joint probability distributions on X_1 by X_2 depends on their marginal distributions.

There are three types of multi-attribute continuous utility function: additive, multiplicative, and multilinear. Multilinear utility functions are a generalization of both the additive and multiplicative utility functions. If some attributes are independent in preference interaction while other attributes have dependence in preference, the multilinear is well suited.

Additive utility is the simplest but also is the most restrictive of forms assuming that there is no interaction in preference between the attributes. In other words, the utility of one attribute is independent of all other attributes. Additive utility functions can be used iff both additive independence and preferential independence conditions are satisfied. Additive independence assures that for a loss of some number of utility units on one attribute and equivalent gain on another, the resulting utility remains unchanged. The general form of additive utility is below where k is a single attribute weighting constant. One equation is needed per attribute to solve weighting terms via a set of simultaneous equations.

$$U(x) = \sum k_i U_i(x_i) \tag{2.15}$$

Multiplicative utility can be used iff preferential independence and utility independence conditions are satisfied. Its general form can be seen in equation 2.16.

$$U(x) = \frac{1}{K}(\Pi[K k_i U_i(x_i) + 1] - 1) \tag{2.16}$$

With the weighting factors satisfying:

$$1 + K = \Pi(1 + K k_i) \tag{2.17}$$

K is a normalizing constant which scales $U(x)$ from 0 to 1. k_i remains the single attribute scaling constant. Multilinear's form is a combination of multiplicative and additive with dependent attributes being multiplied and all sets of independent attributes being added.

2.8 Conclusions

The BN framework presented serves as the basis for data fusion within this body of work. Data fusion produces more accurate information. Accurate information to the decision maker is important but even more so is a method for information interpretation accounting for the decision maker's preferences. Decision support is possible via augmentation of the BN framework with utility and decision nodes.

CHAPTER 3

Fusing Fleet In-Service Measurements Using Bayesian Networks

3.1 Introduction

Readiness, reliability, remaining service life, and the potential for service life extension are all critical factors in managing a fleet of vessels. Changes in the economic climate, technology developments increasing the procurement costs, and operational constraints all can result in the need to extend a vessel beyond its initial design service life. Readiness and reliability are critical to military operations and of significant cost consequence to commercial shipping. Understanding the health and state of individual vessels and the fleet they comprise is critical to making service life extensions decisions, maintenance decisions, and ultimately deployment. Decisions presently are made with limited information pertaining to the present and future vessel state. This section explores a BN approach to fusing in-service failure records to update underlying degradation models and provide enhanced estimates of future vessel states for extension to inspection extent decision support.

Our ability to sense and gather data related to the operating conditions and vessel health has recently increased. The development of monitoring systems that measure proxies for structural health has led to an abundance of data. Identifying and interpreting data to produce meaningful information is key. We have quickly realized that the challenge lies less in data acquisition; it is rather in the production of meaningful information and hence im-

proved decisions from the data. Given the current challenge of turning monitoring data into improved decisions, it is difficult to convince ship owners to place a plethora of sensors and data acquisitions systems onboard. Fortunately, vessels provide a number of innate proxies for structural health degradation that can be taken from the physical record on the ship itself. Two of such indicators are observed permanent set and initiated cracks from structural fatigue. The utility of this data has not been as extensively explored in the research community to date.

Furthermore, fusion (definition provided in Chapter 1) of different types of measurements relating to degradation processes has not yet been demonstrated in the literature. However, as many degradation mechanisms share common underlying processes (e.g. vessel loading) the ability to infer common-cause failures appears attractive. Additionally, many companies and governments operate small fleets of similar vessels which could also allow for intra-fleet vessel fusion of data. If we can effectively synthesize data across failure modes and vessel fleets, we can reduce the need for complex sensor arrays. If this data is from visually detectable sources, sensor arrays could be reduced even further. Within the following section an exploration of synthesizing visually observable deterioration with a BN framework is presented.

3.2 Literature Review

The following was largely taken from Groden and Collette (2016a) which is under review and is entirely the work of the author. Using condition assessment techniques to perform model updating has been investigated over recent years Salvino and Collette (2009). Several authors have proposed frameworks for interpreting monitoring data and updating underlying performance models. Salvino et al. (2009) proposed a multi-tier framework for integrating monitoring data readings and prediction models for naval vessels. The ability to process the large amount of data generated by monitoring systems and to intelligently

update models continues to be an active area of development for the marine community. Extending the initial work of Salvino et al. (2009) a data-to-decision framework has recently been presented for marine structures by Collette and Lynch (2013). Stull et al. (2011) developed a general computational framework to enable model-based hull structural health monitoring using large scale and scope condition assessment problems. Concurrent advances in lifetime reliability frameworks show promise for future life prediction if updated probabilistic models can be generated Ayyub, Stambaugh, McAllister, de Souza, and Webb (2015). However, efficient means of integrating through-life models with inspection data are still lacking.

Extensions of lifecycle and inspection monitoring approaches originally developed for civil engineering applications have also been recently reported. Frangopol and Soliman (2016) presented an approach for reliability updating of fatigue life on aluminum vessels. Similarly, inspection scheduling and short-term routing have also been optimized using updated reliability frameworks Dong and Frangopol (2015), Dec, Frangopol, and Zhu (2012). In a similar vein, Zrate et al. (2012) presented a framework to update and predict crack length as a function of the number of cycles in structural elements subjected to fatigue.

Meulen and Hageman (2013) used Bayesian analysis to predict fatigue accumulation using data from FDS a notched sensing foil which records site-specific fatigue damage. While these models have shown promise in including monitoring data to update design-stage predictions, the fusion of data between failure modes and the use of visual inspection results remain relatively unexplored.

BNs are an attractive technology for such fusion as they allow common-cause failures to be explicitly modeled. By combining BNs with degradation models, Straub (2009) created a computational framework multi-timestep data fusion of fatigue damage processes. This model has been further explored and efficient inference methods have been developed for low-probability events Zhu and Collette (2015), and marine applications.

This previous work has presented probabilistic frameworks for RBI of marine struc-

tures, evaluated BN topology for inspection intervals, and updated structural performance models with monitoring data. However, efforts to fuse common-cause failures in the BN, or infer over a broad class of failures on multiple similar platforms have not been attempted. The BN model presented in this work demonstrates the data fusion and updating capability that can be realized from fatigue failures, and permanent set. A fatigue failure is considered the initiation of a fatigue crack regardless of crack length (e.g. S-N approach). The fatigue capacity of the structure is modeled using a probabilistic lognormal model, which allows for efficient prediction of the probabilities of fatigue failures occurring over time Zhu, Groden, and Collette (2013). Hughes' permanent set model is used, which semi-empirically relates pressure to an approximate permanent set Hughes, Paik, and Beghin (2010). Hughes' permanent set method solves for permanent set resulting from a specified pressure. In the current work, a spline curve is fitted to the result of Hughes' model to solve for pressure given an observed permanent set. The BN model is updated based on observed failures, including crack initiation and permanent set. These failures are then used to create, through Bayesian inference, posterior distributions which more closely match the observed failures than the design-stage estimates. A range of studies, including varying load profiles and updating at different points in the service life are completed. Different types of inspection data- fatigue failures alone, permanent set alone, and the combination of the two are examined. The ability of the network to update the uninspected ships at the present point in time and update for prognosis for all vessels is demonstrated.

This section will proceed by giving a brief overview of the fatigue, probabilistic loading, and permanent set models. Then the formulation of a BN built from these models will be presented. The resulting network's ability to more accurately predict the structural health at present and future points in time is then investigated with and without imposed evidence. Different combinations of evidence and the number of vessels inspected will be explored. Finally, extension to using the more accurate updated model to inform inspection extent decision-making is investigated.

3.3 Framework Methodology

The overall methodology used includes probabilistic models of loading, fatigue failures, and permanent set in a stiffened grillage. These individual probabilistic models are integrated parametrically through a BN, which allows compact expression of conditional dependence between the different failure modes. This network is then used to interpret in-service failure histories, which are presented as evidence to the network. By performing Bayesian inference, the network can then update the underlying probabilistic models to better agree with the in-service observations. Monte-Carlo simulation is conducted to test and validate the network.

3.3.1 S-N Crack Initiation Model

Marine structures are inherently susceptible to fatigue failures. Cyclic stresses originating from wave induced sagging and hogging motions, though significantly less than that required for yielding, can cause crack initiation and growth. Without repair, these cracks grow and can cause fracture potentially resulting in catastrophic failure. Fatigue crack initiation, propagation, and ultimate failure is dependent upon the material properties, geometry of considered location, number of stress cycles, and the stress range of each cycle.

Areas surrounding weld joints are particularly susceptible to fatigue crack initiation and Fricke (2003) provides an overview of the current approaches. For marine strength predictions which require analysis of high-cycle fatigue, the stress-life (S-N) approach is the most suitable option. S is the stress range and N is the number of stress cycles. $S-N$ curves provide a life expectancy, or cycles to failure, for a given material over variable or constant amplitude cyclic loading.

This nominal stress method does not include stress concentration factors and requires testing of a similar structural configuration for each location requiring fatigue life characterization. S-N curves are established through laboratory coupon testing where specimens

are placed in sinusoidal loading until failure. Each specimen failure produces a single point on the S-N plot indicating some number number of cycles sustained until failure. Since coupons do not all fail at the same number of cycles for the same stress amplitude, a probability distribution is formed. When plotted on lognormal axes, the $S-N$ relationship is lognormal.

Owing to uncertainties in material properties, manufacturing geometry, and surface conditions, the design $S-N$ curve is conservative to ensure the majority of details exceed the design life. Vessel operating conditions and detail characteristics often deviate from the design considerations and produce undesirable fatigue life expectancy. Interpretation of inspection and monitoring data makes it possible to update the design $S-N$ curve to better match what is being observed on the operating structure. Should the $S-N$ curve be shifted such that the expected fatigue life is unacceptable, more frequent inspection or repair can be evaluated to prevent premature fatigue failure.

The fatigue capacity model used was presented previously by Collette (2011). The fatigue initiation model employs the traditional $S-N$ fatigue life approach where it is possible to predict the fatigue life of a particular detail under cyclic stress:

$$N = \frac{A}{(\Delta\sigma)^m} \tag{3.1}$$

In this equation N is the number of cycles to failure, $\Delta\sigma$ is the equivalent stress range acting on the fatigue location, and A and m are experimentally determined constants. Equation 3.1 is only relevant to constant amplitude loading. Vessel operation often cannot be characterized by constant amplitude loading; varying sea states, cargo loads and position, and high operating speeds all contribute to loading variable amplitude cyclic loading of the hull structure.

To determine the fatigue life under non-constant loading, a cumulative damage approach must be adopted. The Palmgren-Miner cumulative damage rule is most commonly

used and can be applied to the basic S-N relationship Shigley (1989). For a discrete number of stress ranges, k, summation of the ratio of cycles sustained within each stress range to the number of cycles to failure for that range, a linear accumulation of damage is realized. D_{cr} is the experimentally determined cumulative damage index and within this work considered to be one, meaning that when D_{cr} is greater than or equal to one, the considered detail will sustain fatigue failure. N_i is the number of cycles to failure for a given stress range and n_i is the number of cycles experienced at that stress. The Palmgren-Miner cumulative damage rule can be expressed as:

$$D_{cr} = \Sigma \frac{n_i}{N_i} \tag{3.2}$$

Combining equations 3.1 and 3.2, we obtain an expression for the fatigue initiation life N with the inclusion of the stress uncertainty factor k_f.

$$N = \frac{AD_{cr}}{k_f^m (\Delta\sigma)^m} \tag{3.3}$$

Since both equations 3.1 and 3.2 include experimentally determined coefficients with significant experimental scatter, the fatigue problem has significant investigation into probabilistic modeling. Therefore, the as-built vessel details have large amounts of scatter about the design S-N curve, thus, a stochastic approach to the fatigue life is necessary.

In this model, it is assumed that A, D_{cr}, and k_f all follow a lognormal distribution with $\Delta\sigma$ and m constant. The lognormal distribution is dependent upon shape and scale parameters ζ and λ respectively. Assuming the stochastic variables follow lognormal distributions, the lognormal distribution of N will follow a lognormal distribution with the following parameters:

$$\lambda = \lambda_{D_{cr}} + \lambda_A - m\Big(\lambda_{kf} + ln(\Delta(\sigma))\Big) \tag{3.4}$$

$$\zeta = \sqrt{\zeta_{D_{cr}}^2 + \zeta_A^2 + (m\zeta_{kf})^2} \tag{3.5}$$

The lognormal distribution has the following probability density function and has previously been shown to be a reasonable fit for ship-like structures fatigue data Collette and Incecik (2006):

$$p(x) = \frac{1}{\zeta\sqrt{2\pi x}} exp\Big(- \frac{(ln(x) - \lambda)^2}{2\zeta^2}\Big) \tag{3.6}$$

Under these assumptions, it can be shown that N also follows a lognormal distribution. With this distribution, an analytical solution to the crack initiation reliability problem is available without resorting to methods such as First Order Reliability Method (FORM). Importantly, both the instantaneous probability and the cumulative probability of a crack occurring at any point in time corresponding to a number of stress cycles can be readily determined and used in an updating framework.

This model is extended via an efficient formula, based upon the binomial distribution, for forecasting the expected number of fatigue cracks over time in grillage-type structures with multiple identical fatigue-prone detail is as follows:

$$P(n) = \frac{d!}{n!(d-n)!}\big[(1-p)^{(d-n)}p^n\big] \tag{3.7}$$

$P(n)$ is the probability of n cracks occurring at an instant in time, d is the number of details on the considered grillage, and p is the probability of a crack occurring at an instant in time associated with a number of experienced stress cycles from equation 3.3.

3.3.2 Probabilistic Loading

The loading for both fatigue failures and permanent set is common; in this work only lateral pressure is considered. The BN parametrically encodes a probabilistic pressure distribution

for application to the permanent set and fatigue models. The stresses considered in the fatigue model are directly proportional to the pressure described by a two-parameter Weibull distribution; independence is assumed between successive pressure peaks. A Weibull distribution was chosen for its ease of modeling different lifetime data through modification of the scale and shape parameters. Modification of the shape parameter, β, provides models with either infant mortality or failures increasing over time. A scale parameter, α, dictates the range for which the distribution is defined. The Probability Density Function (PDF) and Cumulative Distribution Function (CDF) of the Weibull distribution are given by:

$$f(x) = \frac{\beta}{\alpha}\left(\frac{x}{\alpha}\right)^{\beta-1} e^{-(x/\alpha)^{\beta}} \tag{3.8}$$

$$F(x) = 1 - e^{-(x/\alpha)^{\beta}} \tag{3.9}$$

An equivalent constant amplitude stress range can be determined by taking expected moments of the Weibull pressure distribution and used with the fatigue model presented previously. While the Weibull distribution will govern the fatigue damage process, permanent set is governed instead by the extreme pressure experienced during the entire operational lifecycle of the asset. If the individual loads follow a Weibull distribution, the highest load out of n repeated samples will approach a Gumbel extreme value distribution as n grows Gumbel (2004). Gumbel distributions are used to model the distribution of the maximum or minimum of a number of samples of various distributions, in this case Weibull. The PDF and CDF of the Gumbel distribution are given by:

$$f(x) = \frac{1}{\sigma} exp\left(- \frac{x - x_n}{\sigma} - exp\left(- \frac{x - x_n}{\sigma} \right) \right) \tag{3.10}$$

$$F(x) = exp\left(- exp\left(- \frac{x - x_n}{\sigma} \right) \right) \tag{3.11}$$

Soares and Teixeira (2000) proposed an approximate formulation to determine the parameters of the extreme value Gumbel distribution from the underlying Weibull distribution given a number of cycles, n:

$$x_n = a(ln(n))^{1/\beta} \tag{3.12}$$

$$\sigma = \frac{a}{\beta}(ln(n))^{1/(\beta-1)} \tag{3.13}$$

These relationships are used to find the Gumbel distribution's scale and shape parameters that correlate to the Gumbel distribution's extreme values, which provide distributions for the permanent set and fatigue models.

3.3.3 Permanent Set Model

Ship shell structures consist of stiffened plates, and longitudinal and transverse frames. When the pressure exerted on the external shell exceeds the elastic limit, the plate deforms permanently, known as permanent set. The ultimate pressure a plate can withstand is far greater than that experienced causing the onset of permanent set. Permanent set of plates is a common phenomenon and is of little concern except for protection against blast and collision and in serviceability requirements. Since many hull shell structures experience permanent set during operation, it is a conveniently available measure of an approximate maximum experienced pressure on the hull; permanent set serves as a record of the highest experienced load.

Visual inspection can quickly determine the permanent set of a plate and the highest load experienced can be determined and used as network evidence for updating. The onset of yield, however, does not represent the pressure limit for the plate. If permanent set is modeled with the Gumbel extreme value distribution then the individual pressure loads which cause fatigue damage will follow the associated Weibull distribution. Therefore,

from observation of permanent set, it is possible to obtain a probability density function for cyclic stress ranges from external shell pressures.

From measurement of permanent set plate dishing, the associated stress exerted on the plate needs to be determined. There does not exist a closed form analytical solution to relating permanent set to an applied uniform pressure because it is dependent upon elasto-platic behavior. The semi-empirical Hughes' method Hughes et al. (2010) was used to model permanent set. Hughes developed this method to provide designers with the approximate load required to experience a specified amount of permanent set for a uniformly distributed pressure as there is no analytical closed-form solution to this relationship. The basis for this method is shown in equation 3.15 which relates the load parameter Q, permanent deflection of the plate w_p, the plate characteristics including its dimensions and material characteristics, and the uniform pressure. Using the relationship in equation 3.14, the pressure associated with a permanent set and load parameter can be found.

$$P = \frac{\sigma_y^2 Q}{E} \tag{3.14}$$

$$Q = Q_y + T(R_w)\Big(\Delta Q_0(\beta, \frac{a}{b}) + \Delta Q_1(\beta, \frac{a}{b})R_w\Big) \tag{3.15}$$

$$\beta = \frac{b}{t}\sqrt{\frac{\sigma_y}{E}} \tag{3.16}$$

$$Q_y = \frac{2}{\sqrt{(1-\nu+\nu^2)\beta^4}}\Big(1 + 1.46\frac{b}{a}^{1.87}\Big) \tag{3.17}$$

$$-\Delta Q_0 = \frac{1 + 3.24\beta^{0.0687}\frac{b}{a}^{1.389}}{\sqrt{(1-\nu+\nu^2)\beta^4}} \tag{3.18}$$

$$-\Delta Q_1 = 1.92\frac{\frac{b}{a}^{1.86}}{\beta^{0.94}} \tag{3.19}$$

$$\Delta R_w = \frac{w_p}{w_{p0}} \tag{3.20}$$

$$\frac{w_{p0}}{t} = \frac{\beta^2}{48\sqrt{(1-\nu+\nu^2)}} \tag{3.21}$$

$$T(R_w) = (1-(1-R_w)^3)^{0.33}, \quad R_w \leq 1 \tag{3.22}$$

A nondimensional plate slenderness ratio, β, is used to characterize all four plate parameters: stiffener spacing, thickness, yield stress, and Young's modulus. The ratio of permanent set, w_p, to the edge hinge value, w_{p0}, provides a nondimensional measure of set R_w. Q_Y is the initial yielding load for which permanent set commences. The load parameter, Q, has two regimes. The first is defined by Q_Y which is non-linear, and the second being linearly proportional defined by ΔQ_0 and ΔQ_1, producing a hockey-stick relationship as can be seen in Figure 3.1. ΔQ_1 is the increase of load above Q_Y which would cause edge hinges in an infinitely long plate (Hughes 2010). ΔQ_1 provides the further increment in the load parameter at the end of the transition zone. The notch upswing in the hockey stick trend is a result of the yielding eventually penetrating completely through the plate thickness and resulting in a fully plastic hinge. In the case of marine shell structures bounded by constraining structural elements on all sides, plastic hinges form on each side.

3.4 Proposed Framework

The goal of the BN in this work is to develop estimates for future fatigue cracking and extension to decision support for the scope and interval of inspections through an inference approach based on observed failures. Failures include both those in relation to fatigue

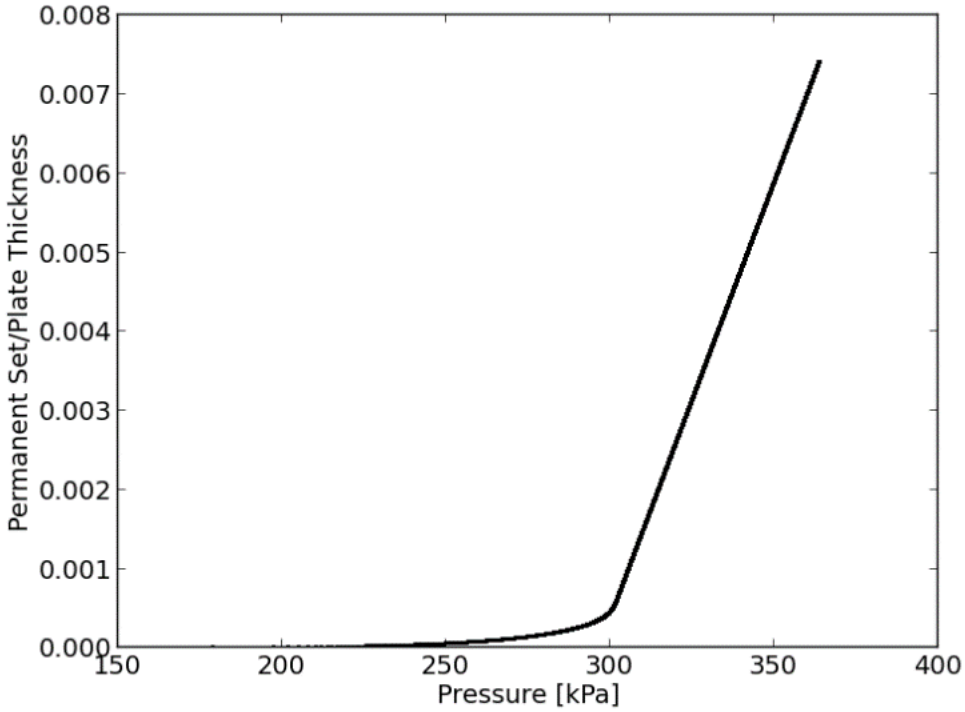

Figure 3.1: Permanent set versus pressure from Hughes' model showing two regimes of response

crack initiation and permanent set. The considered BN can be seen in figure 3.2. In this approach the BN encodes discrete possible values of the log scale parameter, λ, of the log-normal distributions governing fatigue failure in equations 3.1 through 3.3, and the Gumbel distribution scale and shape parameters for the pressure distribution in equations 3.12 and 3.13. This technique is known as parametric encoding as opposed to a conventional, direct encoding where the discrete probability bins are established within the nodes according to their respective distributions. In this work, the ability to update the shape parameter of the lognormal distribution was considered in addition to the scale parameter, comprising the mean $A * D_{cr}$, mean k_f, and the standard deviation $A * D_{cr}$, standard deviation k_f respectively.

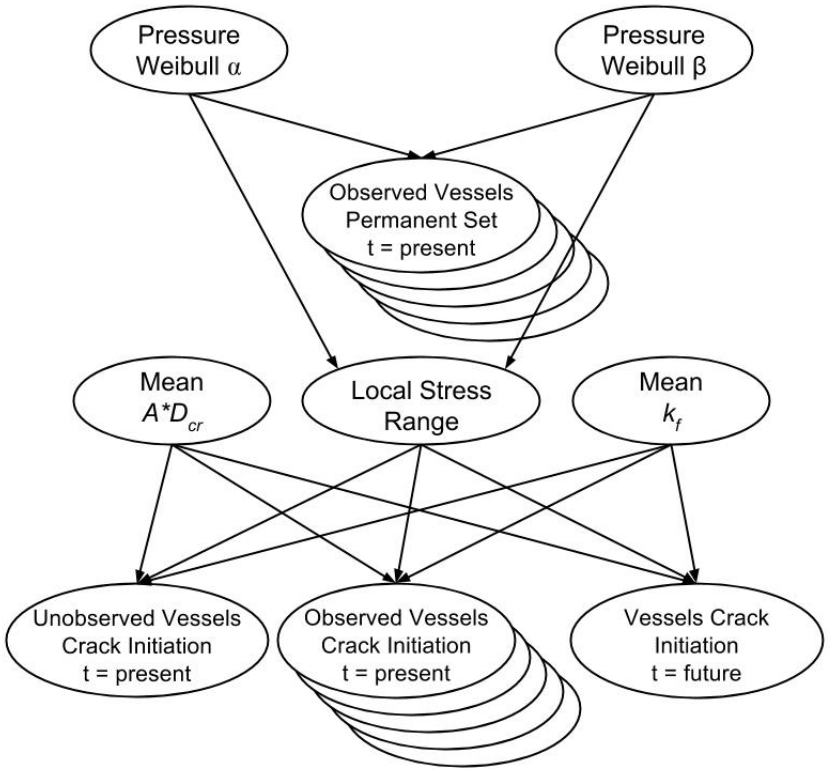

Figure 3.2: Proposed fatigue and set-updating network for observations on multiple ships

Three bins were designated for each of the root nodes. Each combination of parent node bins represents a reliability model encoded within the network. This model represents 81 potential reliability models that could describe the as-built ship. The grillage node was

given 100 statistically identical fatigue-prone details. Each detail follows the lognormal life distribution given previously, but represents a different draw from that distribution. Uniform non-informative priors were assumed for the initial network, indicating no prior preference for any of the 81 potential reliability models. Network discretization and bin boundaries are shown in table 3.1 below.

Variable	Probable Range	Number of States	Interval Boundaries
Crack Initiation	0-100	101	$0:1:100$
Permanent Set (mm)	0-12.8	9	$0:1.6:\infty$
Pressure Weibull α	0.9-1.1	3	$0, 0.9, 1.1, \infty$
Pressure Weibull β	0.071-0.21	3	$0, 0.071, 0.21, \infty$
Mean $A * D_{cr}$	$1.6 * 10^{11} - 2.88 * 10^{11}$	3	$0, 1.6 * 10^{11}, 2.8 * 10^{11}, \infty$
Mean k_f	0.9-1.1	3	$0, 0.9, 1.1, \infty$

Table 3.1: Fleet Fatigue Network Dicretization

By supplying in-service failure statistics to the network in the form of the number of details that have cracked and experienced permanent set, it is possible to update the underlying variables, synthesize the data, and thereby refine the crack initiation prediction.

Updating this networks was accomplished by:

1. With uniform prior distributions on the parent nodes, provide evidence on either fatigue or permanent set on the observed vessel nodes. Each node represents one ship.

2. Evaluate the posterior distributions of the unobserved vessel crack initiation at the present and future timesteps.

Alternative network configurations were considered and evaluated. As will be discussed in the following section, difficulty was realized in reducing the error in the updated standard deviation. In order to attempt to increase the ability of the network to converge on a distribution with a correct standard deviation, the shape parameters for the lognormal distributions were added, as can be seen in figure 3.3. However, the addition of the shape parameter did not materially impact the updating power and these results are not presented.

It was found that the updating power of the BN with a combined A and D_{cr} node had significantly better updating power than treating these nodes separately. This finding is not surprising given that these variables are directly coupled within equation 3.3 as factors of the numerator.

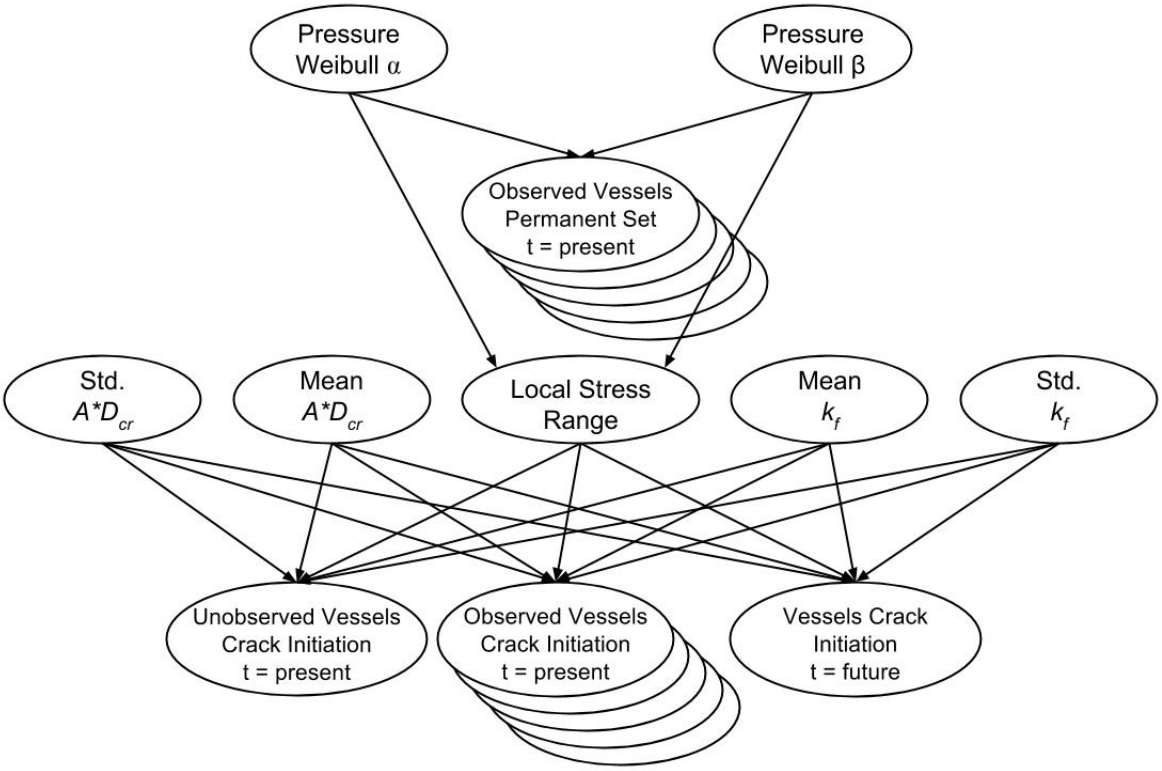

Figure 3.3: Proposed fatigue and set-updating network for observations on multiple ships

This enlarged network with each of the parent nodes including three bins resulted in a total of 729 reliability models for the network to evaluate and choose from. This is significantly larger and therefore more challenging than the network without the shape parameters, however, it was expected that the addition of the shape parameters would improve the ability to tune the resulting posterior distribution to better fit the underlying reliability model. The number of reliability models can be found by the number of bins within the parent nodes raised to the number of parent nodes. In this case, $3^6 = 729$. The results indicated that with shape parameters included, the network results from evidence updating were nearly identical to those without the shape parameters.

To explain why the inclusion of shape parameters did not benefit the updating power of the network, an investigation into the effect of the shape parameter values on crack initiation probability distributions was conducted. Figure 3.4 displays the results. Given the network architecture encodes these parent node variable each with three bins, their selected values are based upon the bin number. Each set of three bars along the x-axis represents the selection of a bin value for the three nodes while the other variable bins are held constant within the first bin. For example when the shape parameter value is equal to two, the first bar in the series of three represents the probability of no cracks initiating given the shape parameter node of k_f is set to a value in the second bin while the other random variable nodes are held constant with values lying in the first bin. The last bar in each set of three shows the probability of no cracks initiating when both $A * D_{cr}$ and k_f bins are set to the value indicated on the x-axis. Thereby we are able to observe the effect on the crack initiation probability from changing values on the shape parameter nodes for $A * D_{cr}$ and k_f individually and together. Also displayed are scale value selections to compare to the relative change with shape values. Evaluating the differences in probabilities, it can be gathered that the effect of changing shape parameter values is small relative to the effect of changing scale parameter values. Thereby we can conclude that the network does not benefit from the addition of the shape parameter random variable nodes because they offer a limited influence on the crack initiation probability relative to the means. For a nine time increase in the number of reliability models encoded by inclusion of the shape parameters, a lesser updating influence is observed when compared to the scale parameters.

3.5 Case Study

3.5.1 Considered Structure

To serve as a proof of concept test case, a simple yet applicable structural component was needed. The structure considered for use within the models presented herein is from a 5415

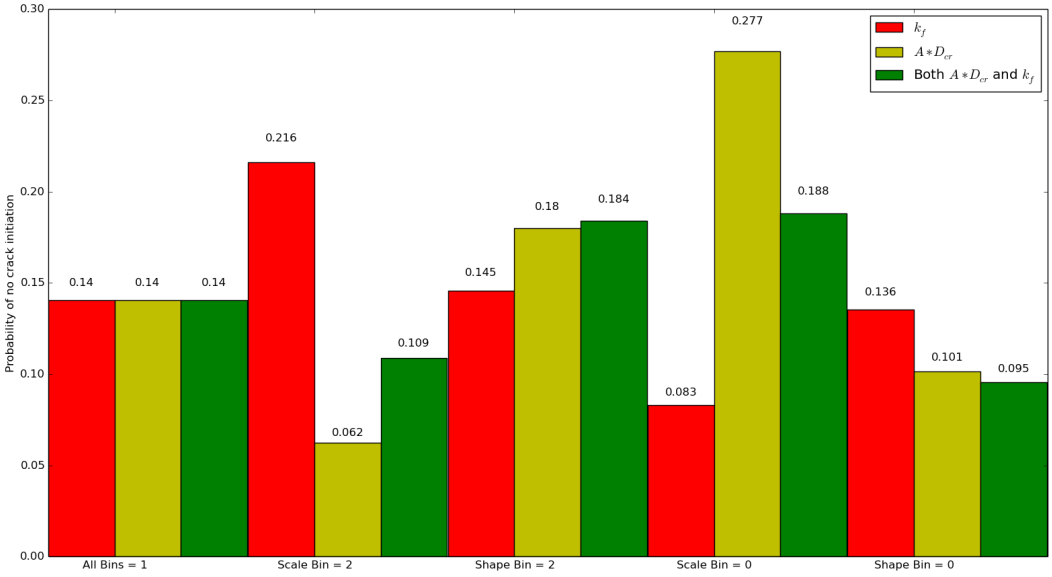

Figure 3.4: Evaluation of the effects of the shape parameter random variable nodes included in the network architecture.

hull midship section, figure 3.5, Ashe (2009) . The highlighted details correspond to a two dimensional view of the chosen grillage. Figure 3.6 depicts a three dimensional view of a typical shell grillage. This particular grillage was chosen for consideration because of its location on the midship section puts it on the waterline, the area most likely to provide visually observable permanent set from wave impact loads. Table 3.2 provides the dimensions for the grillage components. Of particular importance is the distance between transverse frames and stiffener frame spacing. These dimensions are critical to relating permanent set to the stress experienced on the shell plate.

Web Thickness	4.8
Web Height	12.07
Flange Thickness	5.3
Flange Width	101
Plate Thickness	6.35
Stiffener Spacing	400
Transverse Frame Spacing	1,905

Table 3.2: Panel dimensions (mm)

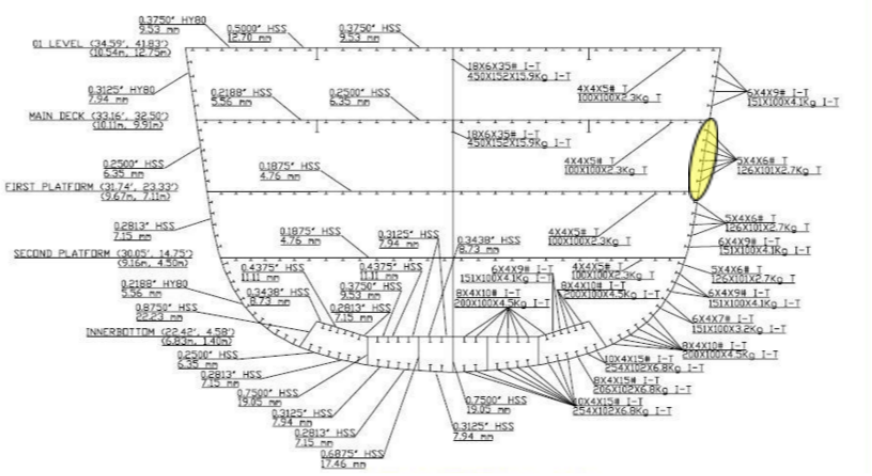

Figure 3.5: Hull 5415 Section 10 longitudinal scantlings Ashe (2009)

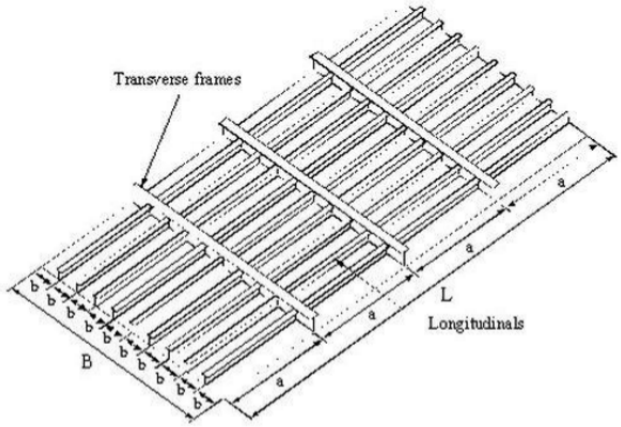

Figure 3.6: Typical stiffened panel, Paik (2003)

For simplicity, the grillage was modeled with 100 similar fatigue prone details. Details were chosen as the junctions between stiffener and transverse frames. These locations are most likely to experience fatigue cracking due to stress concentration from geometric discontinuities, residual stresses from welding, and micro flaws along the weld line. Geometric discontinuities include those inherent to the overall geometry of welding pieces at hard angles, and the notch effect at the location of weld filler material.

Assuming uniform pressure on the hull shell, the stress at these detail locations is calculated by dividing the grillage into equally sized T-panel elements, figure 3.7. This combines sections of the outer shell with the web and flange. Now, the elements can be treated as fixed-fixed beams with uniform loading to compute the maximum stress experienced on the cross section.

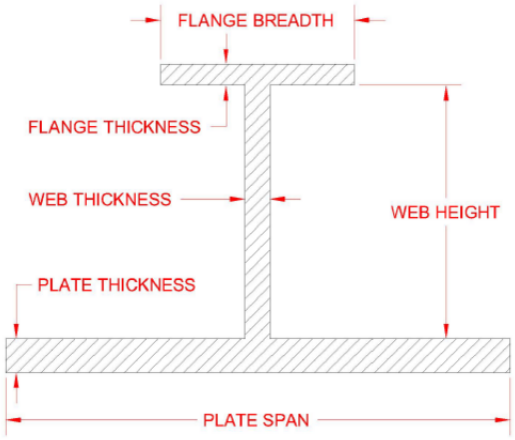

Figure 3.7: Grillage T-panel subdivision, Devine (2014)

3.6 Fleet Wide Support

The BN outlined in (figure 3.3) was tested using synthetic inspection data. The synthetic inspection data was generated via Monte Carlo simulation of permanent set and fatigue crack initiation models presented in the previous section. Five hypothetical ships were simulated from a larger fleet of vessels subject to low-cycle fatigue. The Monte Carlo

seeds and distribution parameters were identical for all result cases shown below. The simulated data was generated at two timesteps. The present timestep at which the initial inspection results would be provided as evidence to the network was $3 * 10^4$ stress cycles. Additionally, a future timestep of $5 * 10^4$ stress cycles was simulated, so that the future structural performance predicted by the network could be compared to the simulation. Over the simulated five ships, an average of 23 initiated cracks out of 100 possible details were simulated in the synthetic data with a standard deviation of 5 cracks; Monte Carlo simulated data for permanent set and fatigue crack initiation can be seen in table 3.3. A cumulative probability distribution is displayed for one of the vessel crack imitation nodes prior to any asserted evidence and with uniform prior distributions across the root nodes in figure 3.8 As 23% cracking is high level of damage, the number of cycles at inspection for one case, or the present timestep, was reduced to $1 * 10^4$ so that fewer cracks would be present. Extreme value Gumbel distributions were also generated for the inspection timestep to simulate a level of permanent set in the plating. The CDF of three of the nine potential Gumble distributions for the three levels of the Weibull scale and three levels of the Weibull shape parameters are compared to the plating permanent set equation in figure 3.9.

Ship	1	2	3	4	5
No. of initiated cracks	19	21	26	24	27
Permanent Set (mm)	0.4	1.5	1.1	0.8	0.2

Table 3.3: Monte Carlo Simulated Data Set

Several different evaluations of the network were made. First, the network as presented in figure 3.2 was tested. Then, parent node bin sizes were varied to examine the effects on updating power. Additionally, the inspection point in time is made earlier in the lifecycle to evaluate the network's ability to update with limited data. An analysis of the network updating power for each of the provided evidence sets is investigated for both the present and future points in time.

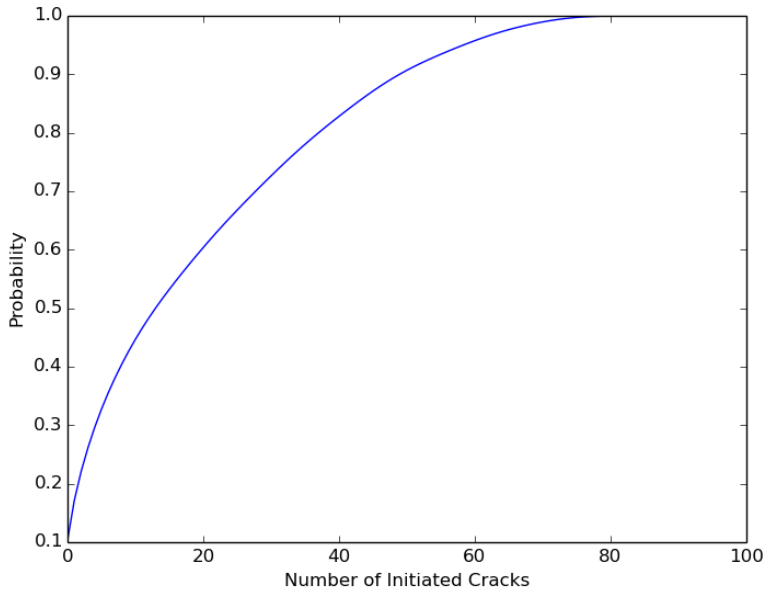

Figure 3.8: Cumulative probability distribution for a vessel crack initiation node with uniform distributions across the root nodes

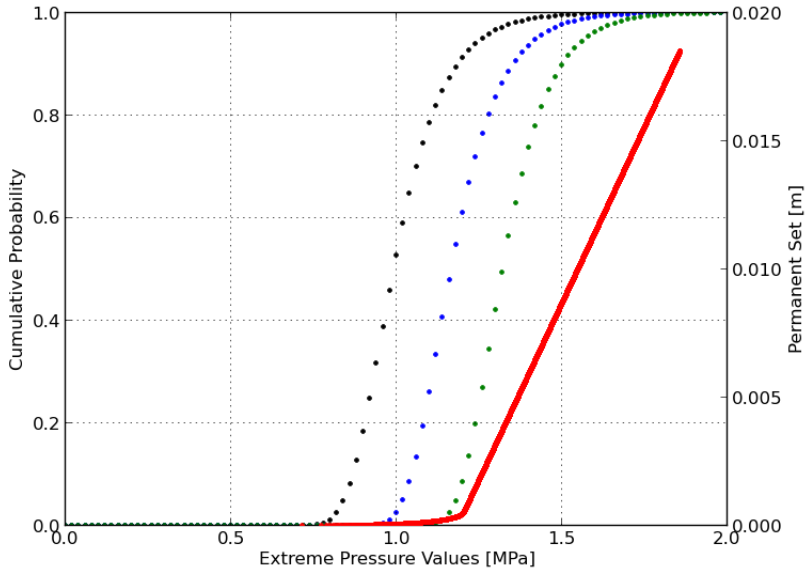

Figure 3.9: Gumbel extreme pressure distribution CDFs vs. plating permanent set - extreme low, mean, and extreme high combinations

3.6.1 Initial Fatigue Network Updating

Figure 3.2 displays the evaluated BN representing 81 potential reliability models, and table 3.4 provides the results for all three combinations of applied evidence. The first two data rows in table 3.4 cover the situation with no evidence. The "synthetic data" row represents the raw data from the Monte Carlo simulation of damage. The "design prior" row represents the predicted value of cracking from the BN without evidence, with the uniform prior on all the root nodes of the network. The columns in the table indicate the mean and standard deviation of the cracks either observed or predicted at two different times - the time of the inspection, and a future timestep at 1.6 times the number of fatigue cycle as the inspection timestep. Over the five ships that had simulated inspections, an average of 23 initiated cracks were observed with a standard deviation of 5 cracks. This compares to a prediction of 20 cracks, and a higher standard deviation of 19 cracks. Permanent set was observed in the lowest bin for each of the five ships.

The final three rows in the table present the the results from the network after providing different evidence sets - sets a, b, and c. For set a, only the number of observed fatigue cracks was updated. For set b, only the permanent set observations were provided to the network. For set c, both sets of data were provided for the network. After the evidence was provided, the network re-forecasts the predicted number of cracks at both the present time (representing ships in the same fleet that were *not* inspected) and the future time (representing all ships in the fleet in the future). For both the design prior and all three evidence sets, the percentage error from the Monte Carlo (simulated truth) data is listed in parentheses after the value.

Evidence	Case	Time of Inspection, no. of Cracks (% error)			
		Present		Future	
		Mean	Std Dev	Mean	Std Dev
	Synthetic Data	23	5	39	5
	Design Prior	20 (14%)	19 (285%)	33 (16%)	25 (400%)
1a)	Fatigue	23 (1%)	5 (8%)	42 (7%)	6 (14%)
1b)	Perm Set	8 (64%)	12 (130%)	16 (58%)	17 (244%)
1c)	Fatigue, Perm Set	23 (1%)	4 (12%)	41 (4%)	5 (4%)

Table 3.4: Results of updating with scale parameter parent nodes and five ships of simulated Monte Carlo evidence. The presented case represents the uninspected ships at present point in time and future is for all vessels.

3.6.2 Fatigue Network Updating with Parent Node Bin Sizes Increased by 50%

To evaluate the network's ability to model and update a larger space of potential true reliability models, the BN's parent node bin sizes were increased in size by 50%. Increased bin size nodes include the scale parameters for the fatigue distribution and the scale and shape parameters of the Weibull distribution. This impacts both the fatigue damage and the level of permanent set that will be observed. The three curves, as shown in figure 3.10, depict the extreme pressure values, Gumbel distributions similar to figure 3.9. By increasing the bin size by 50% for the scale and shape parameters of the Weibull distribution, the associated Gumbel distributions cover a greater range over the extreme pressure values. The plotted Gumbel distributions are representative of three of the nine possible scale and shape parameter combinations, the lowest of each, the highest of each, and their mean values.

Applying the same Monte Carlo simulated evidence, the results can be seen in table 3.5. Note that while the Monte Carlo simulation remains the same as in table 3.4, the design prior changes as now the bins in the network cover a larger range of potential values. The same three sets of evidence a, b, and c, were provided here as in table 3.4, and the results are listed in the last three rows of the table.

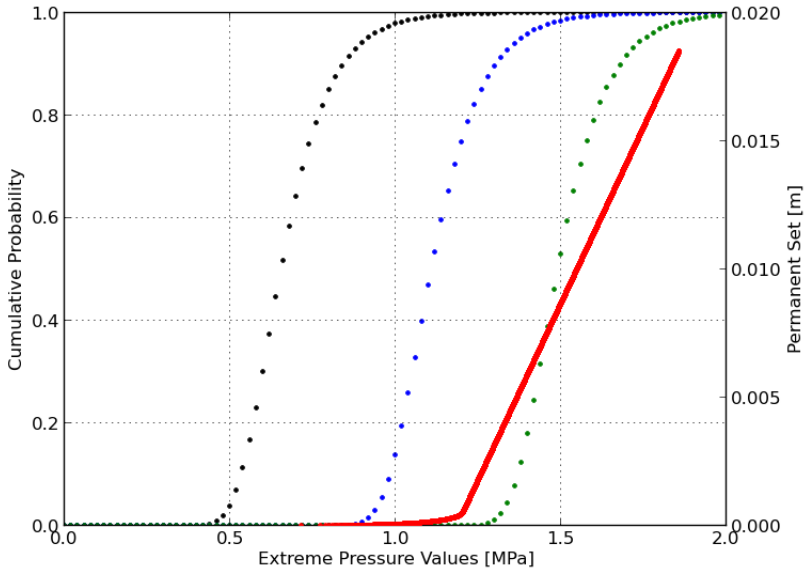

Figure 3.10: Gumbel extreme pressure distributions with 50% increase in bin sizes

Evidence	Case	Time of Inspection, no. of Cracks (% error)			
		Present		Future	
		Mean	Std Dev	Mean	Std Dev
	Synthetic Data	23	5	39	5
	Design Prior	27 (19%)	28 (454%)	38 (1%)	32 (544%)
2a)	Fatigue	24 (4%)	5 (5%)	42 (9%)	6 (22%)
2b)	Perm Set	9 (61%)	16 (211%)	15 (61%)	21 (319%)
2c)	Fatigue, Perm Set	23 (0%)	4 (10%)	41 (4%)	6 (20%)

Table 3.5: Results of updating with scale parameters and 50% increase in parent nodes

3.6.3 Updating the Original Network with Lower Deterioration

If the inspection takes place early in the vessel's lifecycle when few details have cracked, or if the vessel is deteriorating at a much slower rate than anticipated, the network would encounter data starvation. Few details would have initiated cracking, and permanent set would be minimal. To test this case, the same Monte Carlo seeds and governing parameter values are used; however, the first inspection is performed at $1 * 10^4$, resulting in an average of four cracks with a standard deviation of two. The results of updating in this case can be seen in table 3.6. Note that the future timestep was kept the same, and now represents five times as many cycles as the initial inspection time. Thus, in this table the extrapolation required for the future time is also much larger. The same three evidence sets, a, b, and c, were used for the updating.

Evidence	Case	Time of Inspection, no. of Cracks (% error)			
		Present		Future	
		Mean	Std Dev	Mean	Std Dev
	Synthetic Data	4	2	39	5
	Design Prior	4 (4%)	7 (231%)	33 (16%)	25 (400%)
3a)	Fatigue	4 (10%)	2 (1%)	45 (16%)	8 (59%)
3b)	Perm Set	2 (41%)	5 (135%)	24 (39%)	22 (333%)
3c)	Fatigue, Perm Set	4 (12%)	2 (0%)	44 (12%)	8 (57%)

Table 3.6: Results of updating with original size scale parameter parent nodes and a starved evidence set

Tables 3.4, 3.5, and 3.6 show the power of the BN approach to fuse data and make improved predictions. Across all tables, the future cracking prediction for updated case "c" shows significant improvement in the prediction - normally lowering both the mean error and the standard deviation error, and always lowering at least one significantly. Interestingly, the network formulation with a design prior estimate leads to relatively large standard deviations in the predicted cracking levels. This is a result of the network effectively averaging over 81 equally-likely reliability models. The uniform prior here was taken as the

most conservative and challenging assumption. It would be interesting to further explore the network with informative priors, perhaps with stronger belief near the mean values of the reliability parameters. In all cases, providing evidence to the network dramatically reduced this standard deviation error.

In all cases, we can clearly see the BN's ability to fuse data. In tables 3.4-3.6, rows 1c, 2c, and 3c, contain at least two of the best estimates for the present and future mean or standard deviation. Thus, half of all best estimated values occur when evidence from both permanent set and fatigue is provided. Modeling over a 50% larger space of reliability models, table 3.5, demonstrates that the data fusion capability of the network is nearly unaffected with the future standard deviation being the only estimate with increased error. When starving the network of evidence, as shown in Table 3.6, it is observed that although a combination of data provided yields slightly less incremental updating power, updating with both fatigue and permanent set produced the best estimates in all but the present mean value.

Fatigue evidence alone compared to permanent set evidence alone consistently demonstrated superior updating accuracy. Providing evidence on the desired and evaluated variable will always have greater evidence value than a proxy variable. Additionally, permanent set is a very imprecise measurement. A single set value is related to a whole range of extreme pressure values. For the lower pressure values where visible set doesn't occur, the evidence provided to the network is of limited value. Despite the shortcomings of set as an indicator of load, set is an easily observable non-destructive measurement. The addition of set reduces the standard deviation error in both present and future points in time in all three tables. When combined with fatigue evidence, it not only reduces the standard deviation error, but also the mean error.

In all but table 3.5, the design prior error was greater for the forecasted mean and standard deviation than the present case. However, updating the network with combined data produced errors that were better or equal one third of the time and significantly worse for

the future prediction's standard deviation in the starved data set. Examining the improvement from the design priors to the combined evidence case, we can conclude that updating power of synthesized data is greater for future time prognosis than for updating the model to the present point in time.

By providing synthetic evidence from five ships to this network, the network was able to reduce both the mean and standard deviation of the error in predicting future cracking. Fusing multiple data sources, including even imprecise permanent set data, often but not always outperformed single-source updating. In general, the positive performance of this approach was not significantly impacted by either the size of discretization bins or changes in the amount of data observed.

3.6.4 Updating the Original Network with Varying Numbers of Vessels

The following was largely taken from Groden, Liu, and Collette (2016) and is entirely the work of the author with the assistance of Mr. Yan Liu for data collection. With vessels operating on different deployment schedules and operational states, it is worth investigating the ability to leverage data from fewer than five ships. All of the above investigated updating was done with five vessels. If fewer ships are inspected or if only one ship is inspected, would the framework still be capable of synthesizing inspection data with a meaningful reduction in the state of the reliability's uncertainty model? In addition, does the nature of the inspection data contribute to the synthesis capability, i.e. observation of deterioration mechanisms indicative of minimal to no health degradation? These questions are the next worth answering in the development of the BN data synthesis framework.

The same Monte Carlo simulated data and timesteps were used to evaluate the network with fewer ships. Each set of three rows in the table 3.7 present the the results from the network after providing different evidence sets - sets a, b, and c. For set a, only the number of observed fatigue cracks was updated. For set b, only the permanent set observations

Evidence	Case	Time of Inspection, no. of Cracks (% error)			
		Present		Future	
		Mean	Std Dev	Mean	Std Dev
	Synthetic Data	23	5	39	5
	Design Prior	20 (14%)	19 (285%)	33 (16%)	25 (400%)
1a)	Fatigue	19 (16%)	5 (10%)	37 (6%)	7 (43%)
1b)	Perm Set	15 (34%)	17 (239%)	27 (32%)	23 (360%)
1c)	Fatigue, Perm Set	19 (17%)	5 (10%)	37 (7%)	7 (43%)
2a)	Fatigue	20 (12%)	5 (3%)	38 (2%)	6 (23%)
2b)	Perm Set	12 (46%)	15 (202%)	23 (42%)	21 (323%)
2c)	Fatigue, Perm Set	20 (13%)	5 (3%)	38 (3%)	6 (23%)
3a)	Fatigue	22 (5%)	5 (6%)	40 (3%)	6 (15%)
3b)	Perm Set	11 (54%)	14 (173%)	20 (49%)	20 (293%)
3c)	Fatigue, Perm Set	22 (5%)	5 (8%)	40 (2%)	6 (11%)
4a)	Fatigue	22 (3%)	5 (8%)	41 (4%)	6 (12%)
4b)	Perm Set	9 (60%)	12 (150%)	18 (54%)	18 (267%)
4c)	Fatigue, Perm Set	22 (3%)	4 (11%)	40 (3%)	5 (6%)
5a)	Fatigue	23(1%)	5 (8%)	42 (7%)	6 (14%)
5b)	Perm Set	8 (64%)	12 (130%)	16(58%)	17 (244%)
5c)	Fatigue, Perm Set	23 (1%)	4 (12%)	41 (4%)	5 (4%)

Table 3.7: Results of updating with evidence sets from one through five ships. Row numbers indicate the number of ships that were inspected

were provided to the network. For set c, both sets of data were provided for the network. After the evidence was provided, the network re-forecasts the predicted number of cracks at both the present time (representing ships in the same fleet that were *not* inspected) and the future time (representing all ships in the fleet in the future). For both the design prior and all three evidence sets, the percentage error from the Monte Carlo (simulated truth) data is listed in parentheses after the value. The number in the leftmost column represents the number of ships that evidence was observed on, or the number of ships that were inspected. In all cases, ships were inspected for both permanent set and fatigue crack initiation.

Effective data synthesis of fatigue evidence and permanent set evidence can be seen across all cases. The updated set with the least error is with five ships and both fatigue and permanent set evidence. As the number of ships on which evidence is provided increases, the error for mean and standard deviation in general decreases.

The effectiveness of evidence proposed to the network is measured by its ability to predict and reflect the structural state of fatigue crack initiation. Thus, fatigue crack evidence will always be the most powerful at reducing error. As the number of inspected ships increases, updating with permanent set alone actually increases the mean error while decreasing the error in standard deviation. When synthesized with the fatigue evidence, the future standard deviation error is consistently less or the same as the case where fatigue evidence is provided alone. Despite the relatively high error in standard deviation for updating with permanent set alone, its diminishing error with more inspected ships is suspected as the reason for its ability to produce the most accurate update and prognosis when combined with fatigue for five ships.

The law of diminishing marginal returns applies to the number of inspected ships. If inspecting less than three ships, fatigue evidence alone is observed to produce the most accurate update. However, for three through five ships, the additional inspection of permanent set is able to reduce the standard deviation prognosis error that fatigue updating alone is unable to accomplish.

In all the presented results the number of ships inspected for fatigue is the same as that for permanent set. Given fatigue's inability to reduce the standard deviation prognosis error, which is remedied when synthesized with permanent set for greater than or equal to three ships of inspected evidence, updating power of evidence from inspections that did not include both fatigue and permanent set were investigated. Evaluating cases where fatigue initiation was only inspected on one ship while permanent set was inspected on one through five ships demonstrated that permanent set evidence alone in greater quantity is unable to reduce the error. This is particularly interesting. Despite the fact that fatigue evidence

does not improve, the updating power with a greater number of inspected ships, evidence is necessary to reap the benefit of additional permanent set inspections.

When the framework, figure 3.4 presented herein was first conceived it was expected that the most difficult updating case would be when minimal structural deterioration occurs, i.e. few initiated cracks and little to no permanent set. However, previously presented results indicated this did not pose a more difficult updating case. Herein we observe that data starvation and limited updating accuracy are experienced when fewer ships are inspected. Data starvation is proportional to the number of pieces of evidence, not the nature of the evidence.

3.6.5 Alternative Network Configurations

Prior to developing the networks presented above, a slightly different network architecture was conceived, figure 3.11. This network was designed with a slightly less intuitive updating strategy. By averaging the posterior distributions of applied individual evidence cases and providing the averages as priors, it was thought to be fusing the evidence from multiple ships operating in a fleet. Updating this original network was accomplished by doing the following:

1. With uniform prior distributions on the parent nodes, provide evidence on either fatigue or permanent set on the nodes for the present timestep.

2. Find the posterior distributions of the parent nodes governing the underlying reliability model.

3. Store the posterior distributions.

4. Initialize the network again with uniform parent node distributions.

5. For each additional ship on which evidence was observed, repeat the above steps.

6. Take an average of the posterior parent node distributions over their respective bins.

7. Apply the average posterior distributions to the original network replacing the uniform prior distributions.

8. Solve the posterior distributions for crack initiation at both present and prior locations.

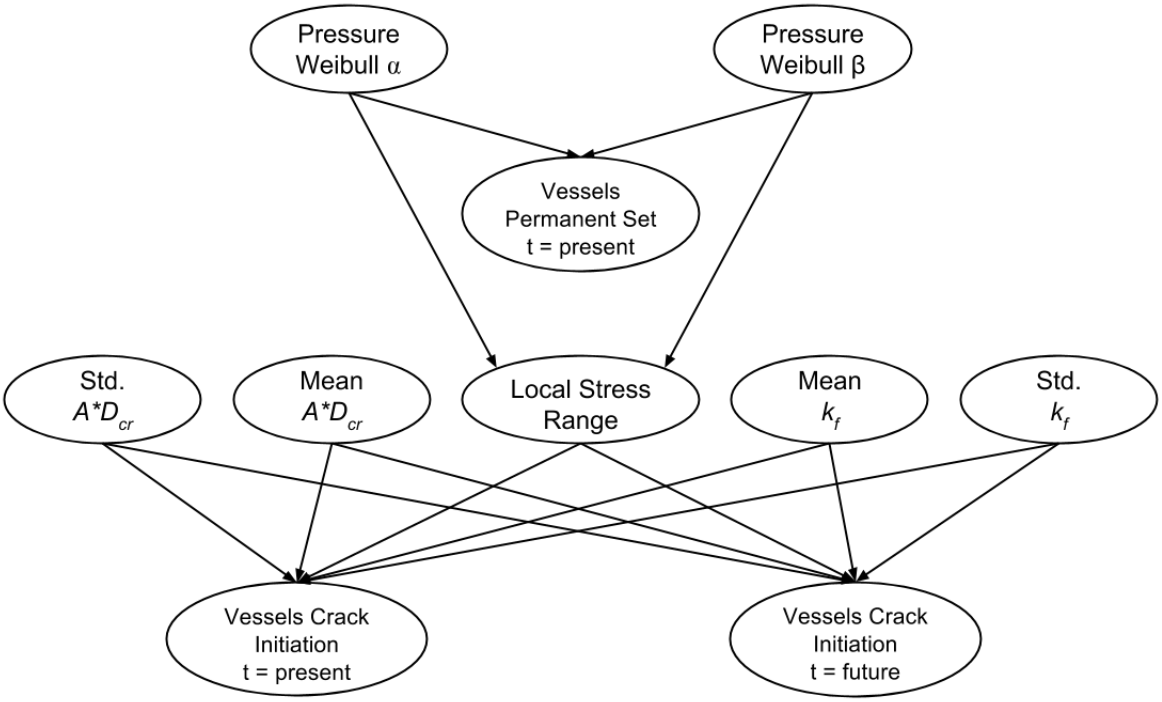

Figure 3.11: Proposed fatigue and permanent set updating network for observations on multiple ships

The key difference between the updating schemes and network architectures is that in the initial framework, the parent node's posterior distributions were averaged for each piece of evidence and averages of the posteriors were provided as priors. This updating scheme was later discovered to produce results that deviated somewhat from those produced by figures 3.3, and 3.2. After contemplating the results of the networks, it was decided that the architecture presented in figure 3.11 was not representative of the multiple ship or fleet wide case that a model was being sought. This modeling approach is better suited as a

representation of similar vessels built at different yards with sources for their materials (sister ships).

3.7 Inspection Extent Support

This section is taken from Groden and Collette (2015) and is entirely the work of the author. A natural extension of better structural prognosis and understanding of the underlying deterioration model is to inform inspection decision-making. The Bayesian framework augmented with decision and utility nodes creates an ID to determine the optimal number of details to inspect for fatigue crack initiation in the present and future inspection points. The present and future nodes are characterized by the number of stress cycles experienced. This affords the ID the ability to provide decision support for an inspection at any point in the vessel's life cycle, figure 3.12.

The utility function was developed and constructed to account for the cost associated with each inspected detail, the cost of an initiated crack, and the cost of failing to inspect a detail which was in fact cracked. Equation 3.23 outlines the structure of the utility function. Additive construction was chosen as *HUGIN* treats utility functions on the same DAG additively.

$$U(\delta, \gamma, \tau) = p(\delta, \gamma, \tau, x) + \left(\frac{\delta - \gamma}{\delta}\right) * \alpha + \left(\frac{\delta - \tau}{\delta}\right) * \beta \tag{3.23}$$

Where δ is the number of total details on the grillage, γ is the number of expected cracks, τ is the number of inspections, and α and β are weighting parameters. The first factor, p, represents the hypergeometric distribution whose probability density function is presented in equation 3.24. The second and third factors account for the cost of cracking and detail inspection respectively.

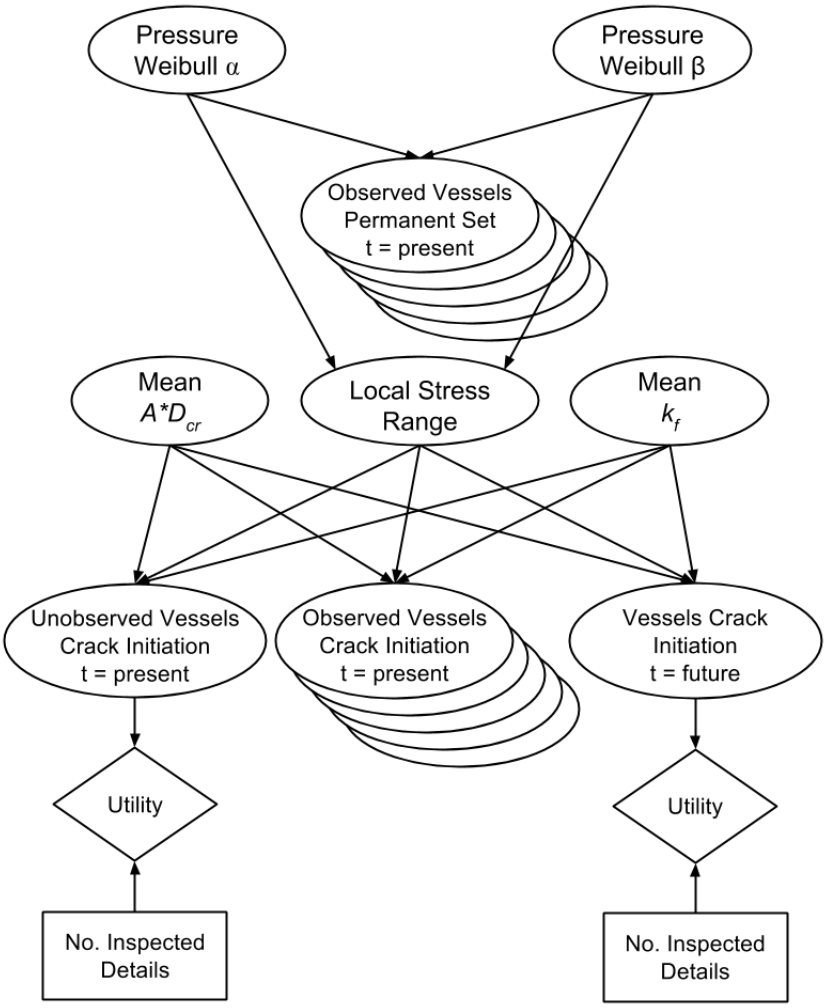

Figure 3.12: Proposed inspection extent decision support network fusing fatigue and permanent set observations on multiple ships

$$p(\delta, \gamma, \tau) = \frac{\binom{\gamma}{x}\binom{\delta-\gamma}{\tau-x}}{\binom{\delta}{\tau}} \tag{3.24}$$

A hypergeometric distribution is a no replacement extension of the geometric distribution. Here x is the number of successes for which the probability is being calculated. For this model, x is determined as the lesser value between the number of cracks and the number of inspected details. This represents discovery of the maximum number of cracks for a given number of inspections and some number of actual details which have cracked. An additional component to this logic placed on the utility function is, if the number of inspections is less than the number of cracks, the utility function value is zero. This ensures inspection for a number of details greater than or equal to the number of locations that have cracked.

The decision nodes encode inspection extent strategies for ranges of detail sets. It is assumed that details that have been inspected in the present inspection will either be repaired or do not require inspection in the next successive inspection.

The same Monte Carlo simulated data set was provided to the network for testing as in the prior section. The most accurate updating case was used, table 3.4 row 1c. Table 3.7 provides the optimal policies and their results. The utility function weighting terms are provided in the first column followed by the optimal number of details to be inspected in the present and future cases. The % of total inspected locations compares the total number of inspected details to two complete inspections, or 200 inspection points, which is the conventional technique. The last column provides the expected percent of total cracks found using the prescribed policies. This value was calculated based on a probability of finding a crack that is dependent upon the number of details which remain as undiscovered cracks, equation 3.25.

$$Cd\% = \frac{I_f * C_f - Cd_1}{100 - (I_p * C_p/100)} \tag{3.25}$$

Where $Cd\%$ is the expected percent of cracks that were discovered after both inspections, I_p and I_f are the number of details inspected during the present and future points of inspection, C_p and C_f are the number of cracks that exist in the present and future points in time, and Cd_1 is the number of cracks expected to be found during the first inspection after inspecting the optimal, prescribed, number of locations.

Within table 3.7, the effects of changing utility function parameters is evaluated. α weights the cost of a crack occurring, and β the cost of each detail that is inspected. Both weighting terms are used to provide some relative weight to the cost a crack occurring and being undiscovered, as represented by the hypergeometric distribution term. In all cases, between 66% and 73% of cracks that occur are discovered. That is despite inspections which are only, at most, 70% of the conventional complete inspection. The utility function behaves as expected with case 2 producing the greatest inspection extent at 70% when the weighting term on crack occurrence is increased, $\alpha = 3$. When the weighting term on the inspection extent is increased to three in case 3 the inspection extent, as expected, decreases. Interestingly, the case with the highest utility is third, where the ratio between the number of discovered cracks to total inspection extent is the highest. Therefore, the tuning of the utility function and its composition are critical to the strategy suggestion and further investigation of parameter sensitivity is necessary.

		No. Details Inspected		Results	
Case	Utility Fcn.	Present	Future	% of total inspected	% of cracks found
1	$\alpha = \beta = 1$	50	50	50%	69%
2	$\alpha = 3$	60	80	70%	73%
3	$\beta = 3$	40	50	45%	66%

Table 3.8: Inspection policies for updating with evidence from five ships using the same Monte Carlo evidence and network as evaluated in row 5c table 3.7. Varying the utility function construction produced modified policies as expected.

3.8 Conclusion

An approach to update the structural performance and reliability models of marine structures has been presented and evaluated for varying numbers of inspected vessels within a fleet. Using only physical observations including permanent set and fatigue crack initiation, bayesian updating was performed on a parametrically encoded framework. The updating power of the network was evaluated for one through five inspected ships with different evidence combinations. Effective data fusion of permanent set and fatigue crack initiation was observed reducing error to a greater extent than either piece of evidence alone. The network demonstrated its ability to quickly converge on a more accurate prognosis and underlying model without requiring many inspected vessels. Error in standard deviation of the prognosis was observed to benefit the most from an increasing number of inspected vessels and fatigue crack initiation evidence was shown to reduce error more significantly than permanent set.

This approach can be modified to include the addition of evidence beyond that which is physically observed and would likely provide greater updating power and decreased overall error. The accuracy of sensing systems compared to visually observed deterioration would likely significantly reduce the number of vessels needed to be inspected for the same updated accuracy. Future work can modify the model to provide additional strategy suggestions in the form of inspection timing. Additional, investigation of the sensitivity to the utility function weighting parameters should be further explored. Finally, investigation of updating techniques to reduce standard deviation error can also be completed.

CHAPTER 4

A Strain Sensing Solution for the Maritime Industry

4.1 Introduction

Sensor arrays are a fundamental part of monitoring the health of a structure. A number of different types of sensors can be employed depending on the particular application. Strain gauges, accelerometers, and temperature and acoustic emission sensors are the most commonly used for structural health monitoring. The monitoring location and data requirements are the most critical to sensor type and technology selection. Considerations for environmental conditions such as noise, humidity, isolation, and the presence of potentially explosive gasses all influence sensor technology selection. Depending on the location being monitored, the preferences and requirements for key sensor characteristics such as range, sensitivity, accuracy, stability, repeatability, and static and dynamic characteristics can vary. Across all structural health monitoring applications, the sensor system must be able to take measurements without doing any harm or damage to the system it monitors. In addition, sensor arrays need to be able to operate for extended periods of time reliably and without human intervention.

Structural degradation and resulting reliability are critical pieces of information. Strain gauges are widely used in marine, civil and aerospace applications for structural monitoring purposes Gagliardi, Salza, Avino, Ferraro, and De Natale (2010). Commercially

available strain gauges have limitations when used to monitor a marine structure. The most common strain gauge uses piezoelectric circuits applied to the material being measured which requires a central amplifier along with power and data cables to for support. Extension of conventional piezoelectric capabilities relying on energy harvesting and wireless data transmission are in development but are challenging to implement on a large marine structure divided by watertight compartments. Monitoring locations confined by metallic enclosures necessitates the sensor to be truly stand-alone. Additionally, while managing damage situations, a rapidly deployable sensing option would be of benefit; this capability presently does not exist.

Many sensing methods for monitoring structural degradation have been proposed. Technology is moving from wired, conventional, piezoelectric strain gauges towards wireless nodes with data transmission and stored energy to wireless nodes with energy harvesting capabilities Kane, Peckens, and Lynch (2014). Remote wind turbine blade monitoring Kristensen and Forskningscenter Riso (2002) demonstrated that wired conventional strain gauges would be sufficient for damage detection. However, routing of data and power cables down the blades' internal structure is necessary and installation of such a system after final turbine assembly would be difficult. Even for bridges, which are large static structures easily instrumented post construction, wired systems are expensive to implement Yi, Li, and Gu (2010). The wireless transmission systems' energy expenditure limits the longevity of devices with stored energy. Haksoo Choi, Sukwon Choi, and Hojung Cha (2008) proposed a cost-effective wireless transmission that uses multi-hop data transmission between nodes to mitigate this energy tax. Furthering the development of a truly stand-alone strain sensor, McCullagh, Galchev, Peterson, Gordenker, Zhang, Lynch, and Najafi (2014) proposed a vibration harvesting method for long term monitoring of bridges. These advances move sensing technology closer to a cost-effective sensor network that one day could be implemented on a marine structure.

Strain sensors are applied on structural detail locations that are infrequently the same.

Ideally, sensors would be manufactured with characteristics for the specific monitoring location. Additive manufacturing provides a cost-effective method to produce dissimilar parts each batch. Recent advances in additive manufacturing technology have enabled construction with increasing repeatability and accuracy Bak (2003) Bogue (2013) extending the utility of additive manufacturing from rapid prototyping to an approaching viable option for large scale production. Stereolithography is a additive manufacturing technique proposed in the late 1980s. Many alternative approaches have been proposed and developed since. In the past ten years there have been significant advances in photoinitiated polymerization Yagci, Jockusch, and Turro (2010), which have provided stereolithography the highest fabrication accuracy Melchels, Feijen, and Grijpma (2010). With increasing additive manufacturing capabilities and the U.S. Navy evaluating its use on board vessels for replacement part construction, the strain sensing solution presented herein was developed using stereolithography as the manufacturing technique.

In Chapter 3, it was recognized that permanent set's extreme stress was not sufficient to update the reliability model accurately. A method of stress distribution data collection with greater resolution would be required without necessarily providing perfect or complete data. Thus, a patented stand-alone mechanical strain gauge that optically records strain in real-time is presented within. First, the design considerations and overview of the development of the 3D-printed manufacturing technique are discussed, followed by sensor calibration, repeatability testing, manufacturing variability testing, and a weld test. In the weld test, the Strain Amplification Sensor (SAS) is evaluated for its ability to provide real-time deformation measurement. Finally, future work extending the SAS technology and conclusions are discussed.

4.2 Design of the Strain Amplification Sensor

4.2.1 Design Objectives

A sensor well suited for the marine environment was determined to have the following characteristics:

- Stand-alone - be capable of operating without requiring wired transmission of data to a central Data Acquisition System (DAQ) and be free of power and data cable requirements
- Intrinsically safe - many marine environments, especially offshore oil operations, require systems to be intrinsically safe as they must operate in environments with potentially explosive gases
- Cost-effective - marine structures are large with many locations on which data should be collected, each sensor must be inexpensive enough to provide a cost-effective solution for the entire vessel
- Easily adaptable - many measurement locations are dissimilar, necessitating a sensor that can be easily modified for each location's requirements
- Non-destructive installation and removal
- Capable of rapid installation and removal
- Strain time history recording

This list is for both structural monitoring during the vessel's life cycle and for sensor deployment post-damage.

Figure 4.1: PPSS principle overview. Left and right towers with the sensor arm between.

4.2.2 Preliminary Solution: The Passive Peak Strain Sensor

The novel solutions presented within this chapter are entirely the work of the author. Research assistants Kaihua Zhang, Allison Ward, and Jiaxi Chen were vital to the prototype development and testing presented herein.

The first solution invented within this body of work is called the Passive Peak Strain sensor (PPSS). The PPSS is a 3D printed, plastic assembly with only mechanical methods to record strain. The PPSS records maximum strain through a sensor arm progressing down a pyramid-like geometry as strain is imposed between the sensor arm's mounted location and the pyramid; both points being fixed to the surface of the material for which strain is being measured.

The PPSS sensor operates off of basic physical properties. When the length between the two fixed elements increases large enough such that the sensor arm is free to fall to the next shelf, the pretension in the sensor arm forces it to do so; the resting position of the sensor arm providing no internal stress is in the location resting on the lowest step, figure 4.1. Thus the maximum deflection is recorded by the location of the sensor arm's position on the steps. The configuration displayed only records the maximum strain due to tensile loads.

Given the maximum change in length and the initial distance between the two points fixed to the material, using equations 4.1 through 4.3 the maximum stress experienced can be found on the specimen.

$$\eta_{max} = \frac{\Delta L_{max}}{L} \tag{4.1}$$

$$\eta_{max} = \frac{\sigma_{max}}{E} \tag{4.2}$$

$$\sigma_{max} = \frac{\Delta L_{max} * E}{L} \tag{4.3}$$

During the design of the PPSS, there were a couple of considerations regarded as key to its success. First and foremost is the ability to accurately fix the two towers the correct distance from one another on the material being monitored. Next, the step's end points needed to be incremented such that each step ended a distance successively further from the pivot point and mounting location of the sensor arm. Otherwise, steps may be missed in entirety as the sensor arm passes downwards as the towers are pulled apart, or some steps may hold greater value of observed stress than others. Ideally, each step's seated location of the sensor arm correlates to a predetermined and linearly increasing value of observed strain.

Limitations associated with 3D printing technology were at the forefront in PPSS design constraints. The machine used to manufacture the PPSS was only capable of printing with a resolution accuracy of $50\ \mu m$. The minimum overall length of the PPSS and step increments were determined based off of this limitation. Additionally, due to the additive nature of 3D printing, structural scaffolding needed to be printed between surfaces on the same vertical axis. Scaffolding was to be cut away in the final manufacturing process' step. This necessity resulted in the design of a jig instead of manufacturing the PPSS as one unit. Finally, in order for the sensor arm to fall down each successive step it was manufactured in the final step's resting position, resulting in pretensioning when placed on the first step. This, in effect, created a cantilever beam bending problem with limited ability to calculate the effective shortening of the sensor arm due to non-linear deflection when an end force was imposed. Therefore it was decided that the arm would be manufactured over nearly its entire length as rigidly as possible except at the pivot point, which also serves to provide

Figure 4.2: PPSS isometric overview. Again with left and right towers with the sensor arm between.

pretensioning to the arm. Figure 4.1 depicts this concept as can be seen on the right hand side of the sensor arm, there is no vertical 'T' component. An isometric view of sensor arm and assembly can be seen in figure 4.2.

Early design iterations quickly realized that there was no way to print the unit as one part due to the structural scaffolding. Since the part was to be printed such that the end of the steps were upward facing to ensure highest accuracy in printing resolution, there would need to be scaffolding built on top of the steps extending to the other tower on which the sensor arm is mounted. At the end of the manufacturing process scaffolding is to be cut away, which would leave burrs on the stair ends. This was unacceptable considering the stair ends needed to be manufactured with an accuracy of $50\ \mu m$. Burrs would create lengthened stairs by arbitrary amounts and cutting them away could produce divots deviating too significantly from the $50\ \mu ms$. Thus, it was determined that a jig needed to encapsulate the two towers and fix them during adhesion to the monitored surface. First jig iterations called for an exterior shell that was to be printed around both towers and provide exit pins for release of the jig once bonding was completed. However, it was found that 3D printing is not capable of printing two parts, i.e. jig and tower, less than $50\ \mu m$ from one another without melding them into one. The final design utilized two alignment rails manufactured on a breakaway jig to the stair tower. The sensor arm tower has rail receiv-

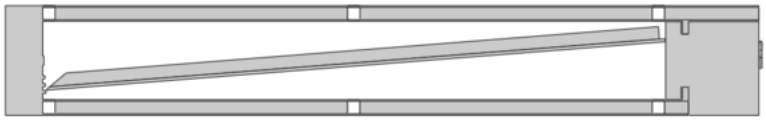

Figure 4.3: Cutaway jig assembly utilizing a 3-point bending configuration for easy removal after installation.

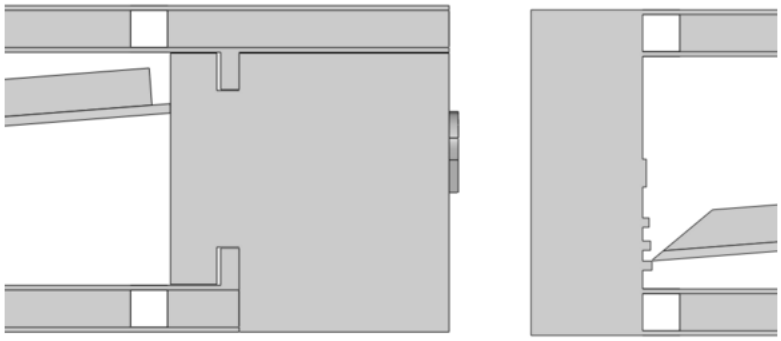

Figure 4.4: Jig rail interface (left) and jig stair tower mounting (right).

ing channels that allow the two towers to be accurately placed. A side view of its design can be seen in figure 4.3. The six slots of material voided in the I-beam jig horizontal components serve to aid cut away and in effect create a 3-point bending scenario when a force is applied in the middle of the jig, easing removal. The alignment rail interface posed an interesting problem in that it was necessary for the rails aligning the sensor towers be accurately aligned to within $50\ \mu m$, however, when printing the female component $50\ \mu m$ larger than the male, the rails would not seat into the sensor tower. Figure 4.4 depicts this seating arrangement and tolerance adaptation.

The other end of the jig assembly and its connection to the stair tower are depicted in figure 4.4. Note that the sensor arm is manufactured in this position, resting on the last stair. Figure 4.5 is an isometric 3D view of the entire sensor arm, stair tower, and cut away jig. In order to measure stress in increments of 40 MPa on aluminum, the PPSS had a required minimum overall length of 10 cm. The length is directly proportional to print accuracy and the material's young's modulus. Figure 4.6 shows the corresponding principle dimensions

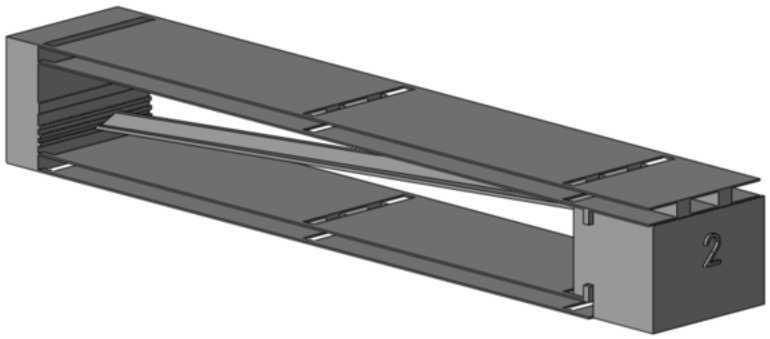

Figure 4.5: Complete PPSS assembly with cut away jig.

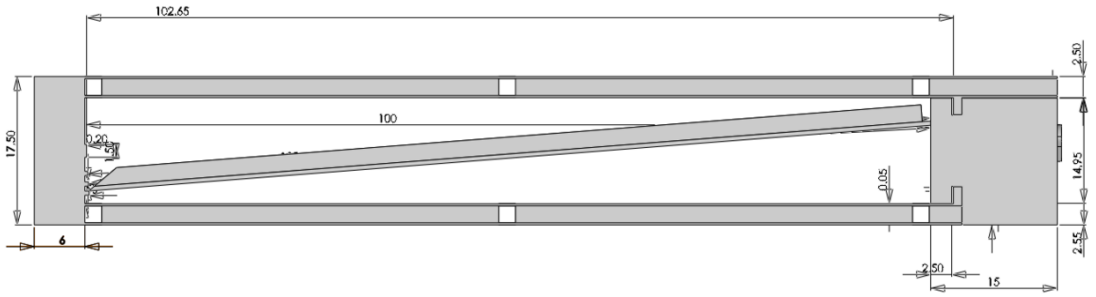

Figure 4.6: Principle dimensions (mm) of PPSS for measurement of 40 MPa increments on aluminum.

in millimeters.

The PPSS final prototype design was tested on a Mark-10 Pull Tester, figure 4.7. Using a thin strip of aluminum as the test material, PPSS was mounted on the device and put in tensile strain. It was found that the poor dimensional tolerances of PPSS manufacturing processes limited its ability to respond in a reliable manner to strain. In addition, the mechanism's sensitivity to out of plane bending was significant.

It was realized through this process that a different solution type would be needed to accurately and repeatedly measure strain using a 3D printed mechanism. First, some method of amplifying strain motion would be necessary, as 3D printing tolerances were not capable of discerning motions less than the best achievable tolerances. This led to to the Strain Amplification Sensor described in the next section.

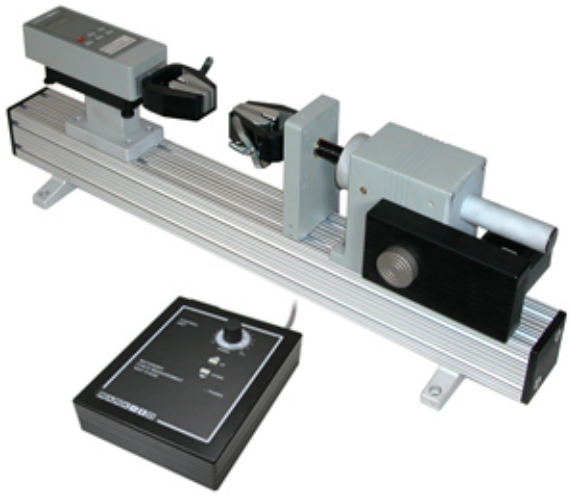

Figure 4.7: Mark 10 Pull Tester

4.2.3 Final Design Solution: The Strain Amplification Sensor

4.2.3.1 Design

The 3D printer's unsatisfactory resolution capabilities limited the PPSS's ability to record strain with a high level of accuracy. Realizing that features could not be additively manufactured on the order of the displacement experienced due to strain, it was determined that amplifying the motion would be necessary.

Using a series of levers to amplify strain displacements, the SAS is a 3D printable assembly using only mechanical methods to record strain, figure 4.8. The SAS records strain in both tension and compression through a sensor arm that activates a series of three amplifying lever arms. Because it is purely mechanical, it is intrinsically safe. In real-time the SAS responds to strain observed on the measurement material and displays the reading on the sensor face. This means that SAS is stand-alone and does not require a power or data acquisition system.

SAS operates by measuring the change in displacement between two mounting locations. A rigid, cantilevered beam extends from one side to the other. As the material being measured deforms, the rigid bar places force on the other side of the SAS assembly. This

force is translated to motion of a mechanical system and the mechanical reaction divided by the known distance over which the cantilevered bar spans produces the basis for strain measurement.

By being 3D printable, the SAS can easily be tuned to different sensitivities and detection ranges. Present testing is based upon magnetic attachment of the SAS. Magnetic attachment affords the user rapid installation and removal. 3D printing each sensor allows for tuning with respect to not only the detection and measurement of strain, but also for the mounting configuration. The SAS's base can be modified and adapted to the contours of any surface or mounted between two nearby positions on a structure that are not necessarily continuous.

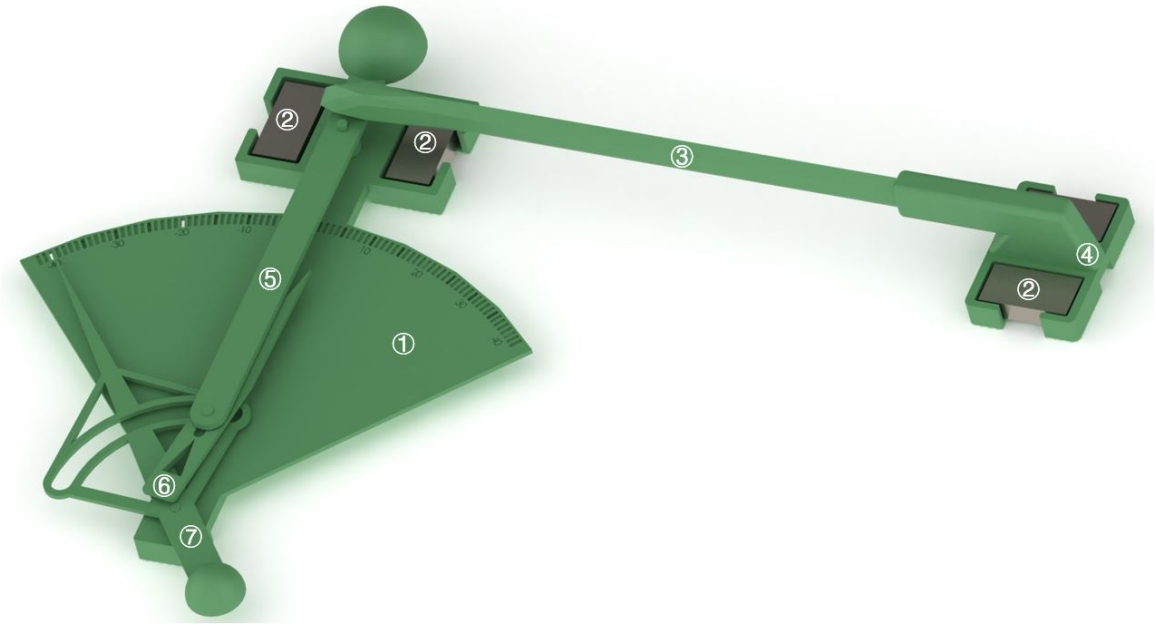

Figure 4.8: 3D model of SAS (① Sector Base Plate ② Magnet ③ Long Sensor Arm ④ Sensor Arm Base Plate ⑤ Actuator Arm ⑥ Pointing lever ⑦ Measurement Pointer)

The principle dimensions of the version of SAS tested are presented in table 4.1.

To transform displacement due to strain into a visually observable phenomena, significant amplification of the underlying motion needs to take place. SAS achieves this in two ways. For each of its three levers, the fulcrum is placed closer to the lever end on which the excitation is being received, making the opposing end of the lever move over a larger dis-

Length Overall	123 mm
Width	84 mm
Height	14 mm

Table 4.1: SAS principal dimensions of the version evaluated herein

tance proportional to the relative distance between the end points and the fulcrum. Second, the attachment location of the second lever arm to the third and final lever arm induces opposing relative motion between the second lever arm and the third. This interaction further amplifies the motion providing a total amplification on the order of thousands of times.

As the distance between the two base plates increases or decreases, the lever amplification system is activated. Figure 4.9 demonstrates the lever system reaction to a decreasing distance between the two base plates or a compressive force. The arrows indicate the moving directions of each individual part. The actuator arm and pointing lever move towards the system while the measurement pointer moves away from system. Conversely, when the distance between two base plates increases, the actuator arm and pointer move away from system while the measurement pointer moves towards system. That is to say, the actuator and pointer move in the same direction opposite of the measurement pointer's movement.

4.3 Testing and Evaluation

4.3.1 Evaluation of the 3D Printed Assembly

With 3D printing technology still maturing, much time was spent realizing something close to the CAD models in material form. Resolution capabilities for stereolithography were found to be significantly poorer than those advertised across the industry. In addition, feature accuracy was found to decrease with smaller feature sizes. Stereolithogrpahy prints in layers, which makes printing rounded shapes such as pins and holes somewhat challenging. The majority of the prototyping man hours were spend iterating through variations of the true dimensions until CAD input dimensions produced parts that were within dimensional

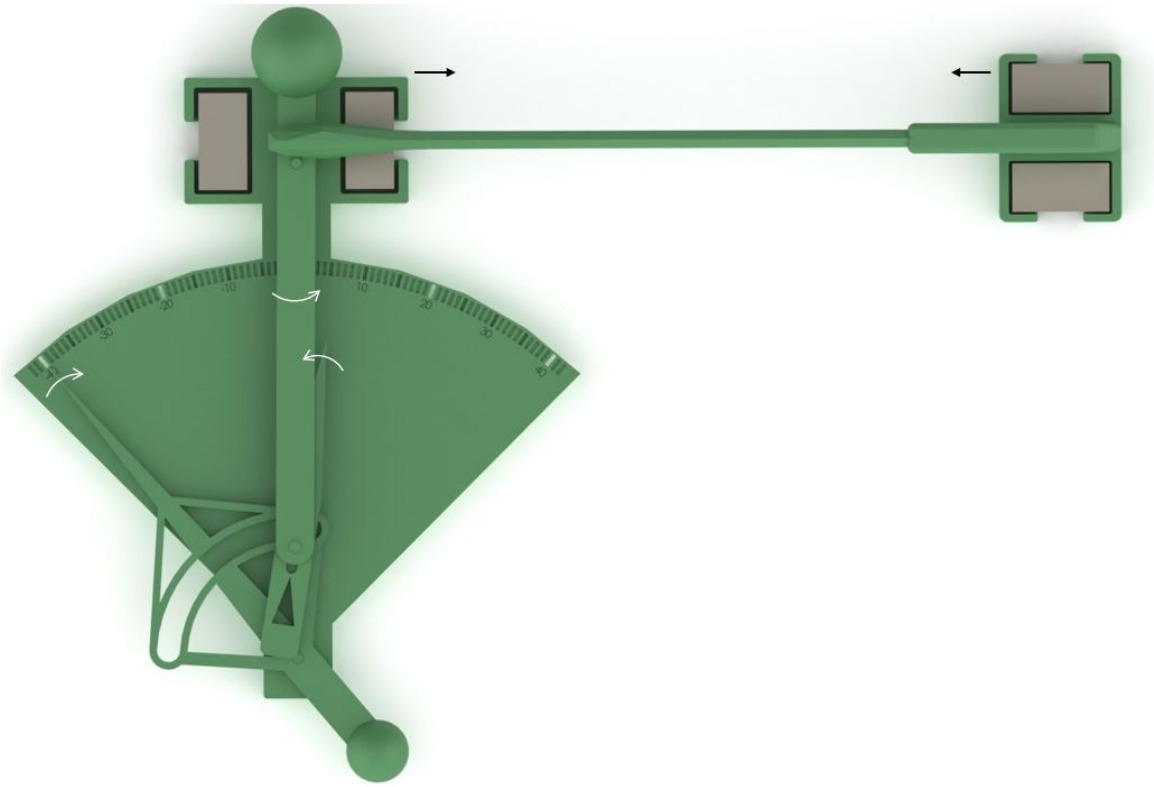

Figure 4.9: SAS movement illustration, initially in tension and showing movement as compression begins

tolerance.

SAS comprises of two mechanical joint types, pin to hole, and pin to slot, figure 4.10. Both connection types require snug but smooth interfaces. If SAS's mechanism causes too much internal stress, it seizes. And failure to transmit motion through connections dramatically reduces the sensitivity and accuracy of the design. Prior to print iteration, SAS was unable to detect a change from tension to compression or vice versa of less than 6 μm; after prototype iteration, this transition gap became nominal.

To further reduce internal stresses, each of the levers was balanced about its point of rotation. Balance was accomplished by adding counter weights in the form of half spheres for longer levers and placing lightening holes on the longer side of shorter levers.

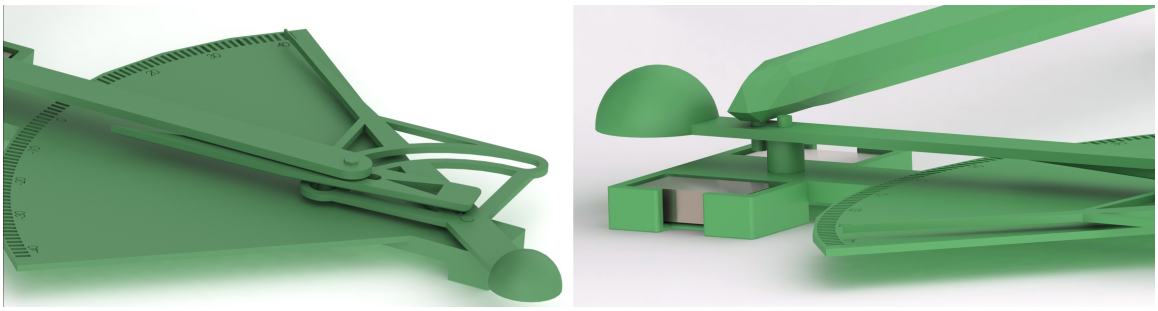

Figure 4.10: Pin and slot connections (left) and pin and hole connections (right)

It was found that a significant source of error in early designs rested on the deflection of the long sensor arm, both along its length and local to the driving pin at its end. To mitigate this deflection problem topology optimization was conducted on the cantilevered beam or sensor arm to reduce the deflection from vertical orientation of the end located pin used to drive the mechanism.

In total, more than 30 unique prototypes were needed to realize the sensor as it was tested in the following sections. SAS was manufactured using the material with characteristics outlined in table 4.2. The 3D printer used was the 3D System Viper. Its specifications can be seen in table 4.3.

ASTM Method	*Property Description*	*Metric*	*English*
D638M	Tensile Modulus	2,100 MPa	305,000 psi
D638M	Tensile Strength at Break	44.9 MPa	6,500 psi
D638M	Elongation to Break	6.1%	6.1%
D790M	Flexural Strength	74.3 MPa	10,770 psi
D790M	Flexural Modulus	2,200 MPa	329,000 psi
D2240	Hardness (Shore D)	85	85
D256A	Izod Impact (Notched)	0.23 J/cm	0.46 ft lb/in
D570-98	Water Absorption	0.7%	0.7%
E831-05	C.T.E. -40°C-0°C (-40°F 32°F)	74.1 μm/m-°C	41.2μin/in-°F
E831-05	C.T.E. 0°C-50°C (32°F 122°F)	96.3 μm/m-°C	53.6 μin/in-°F
E831-05	C.T.E. 50°C-100°C (122°F 212°F)	141.8 μm/m-°C	78.9 μin/in-°F
E831-05	C.T.E. 100°C-150°C (212°F 302°F)	182 μm/m-°C	101.3 μin/in-°F
D150-98	Dielectric Constant 60 Hz	3.16	3.16
D150-98	Dielectric Constant 1 KHz	3.12	3.12
D150-98	Dielectric Constant 1 MHz	2.94	2.94
D149-97a	Dielectric Strength	14.89 kV/mm	378 V/mil
E1545-00	Tg	49°C	120°F
D648	HDT @ 0.46 MPa (66 psi)	59°C	138°F
D648	HDT @ 1.82 MPa (264 psi)	50°C	122°F

Table 4.2: 3D printed material's mechanical and thermal/electrical properties ((D638M) to (D570-98) are mechanical properties. (E831-05) to (D648) are thermal/electrical properties.)

Equipment	*Max Build Extents*	*Layer Thickness*	*Min Feature Size*
3D Systems Viper	5"×5"×2.5"	.001"	.002"

Table 4.3: 3D printer technical specifications

4.3.2 Test Apparatuses

The objectives of the battery of tests that were performed included: characterizing SAS's behavior by determining its response to incrementally increasing strain, which serves as calibration, determining the repeatability of the measurements recorded by SAS and their accuracy, and finally, determining the differences in SAS's performance between different 3D printed batches.

Before testing the entire SAS assembly, the amplification mechanism was isolated and evaluated. Using a P-603 Piezo Movement Actuator from Physik Instrument (PI), material strain displacement was simulated from both tension and compression, figure 4.11.

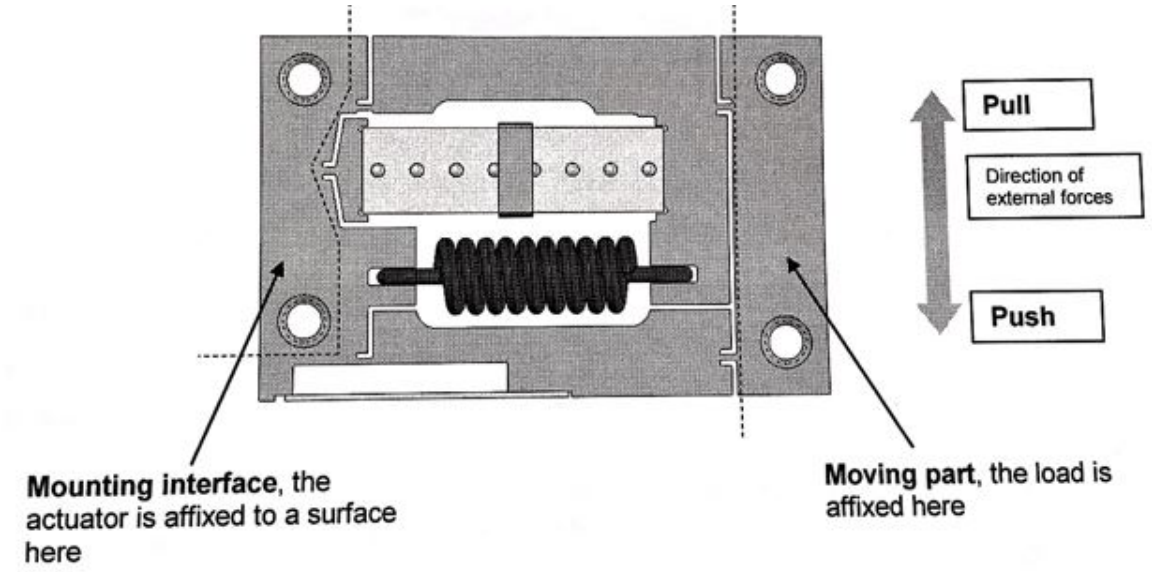

Figure 4.11: *Plan view of P-603 Piezo Actuator*. 2014. Technical Note of P-603 PiezoMove OEM Flexure-Guided, Lever-Amplified Actuators. Physik Instrument(PI). Germany

This test bed served as the basis for calibration, repeatability testing, and manufacture deviation evaluation between batches.

From the plan view depicted in figure 4.11 of the P-603 piezo actuator, the basis for driving SAS can be gathered. Fixing the left screw holes to a surface, the moving part on the right side pulls or pushes the SAS's sensor arm to simulate material tension or compression. An aluminum base plate was used to connect the SAS mechanism to the left

side while another aluminum base was used to fix the driving side to a 3D printed driving bar on the left side. Figure 4.13 shows the SAS mounted. A 3D printed driving bar was chosen as opposed to extending the aluminum base to drive the mechanism to ensure proper simulation of the internal stresses between all joints, including the cantilevered beam.

LABVIEW was used to activate the piezo motor, through a E-709 Digital Piezo Controller. The time between cycle repetition can be set in *LABVIEW* program. By commanding "MOV 1 1" or "MVR 1 1" in write buffer, the piezo actuator moved to a specific position or moved continuously with specific steps and timesteps. This served as the basis for command inputs for all testing completed on this device.

Figure 4.12 is the flowchart of testing process based on piezo actuator. *LABVIEW* receives input commands and transfers them to piezo controller which can control the piezo actuator's movement. The piezo controller and piezo actuator make up a feedback system to implement precise movement.

After evaluating the amplification mechanism alone on the piezo actuator, an assembled SAS was tested on a pull tester. An aluminum test specimen was placed in the jaws of the pull tester device and SAS along with a conventional piezo electric wheatstone bridge were place in the center of the specimen, figure 4.14.This test set-up allowed for testing of the entire SAS mechanism and sensor arm system in tensile stress.

4.3.2.1 SAS Calibration

To calibrate the SAS, the piezo motor was given commands to move the mechanism at increments on the order of $< 1\ \mu m$. Time between each step was varied and the sensor's response to variation in time between induced motion was evaluated.

While testing with several different steps, it was discovered that if the step was too small or too large, SAS would react in an unpredictable manner. For the version of SAS tested, if step sizes were smaller than $0.4\ \mu m$, negligible movement resulted from SAS and over many of such steps, significant variability in cumulative motion would result.

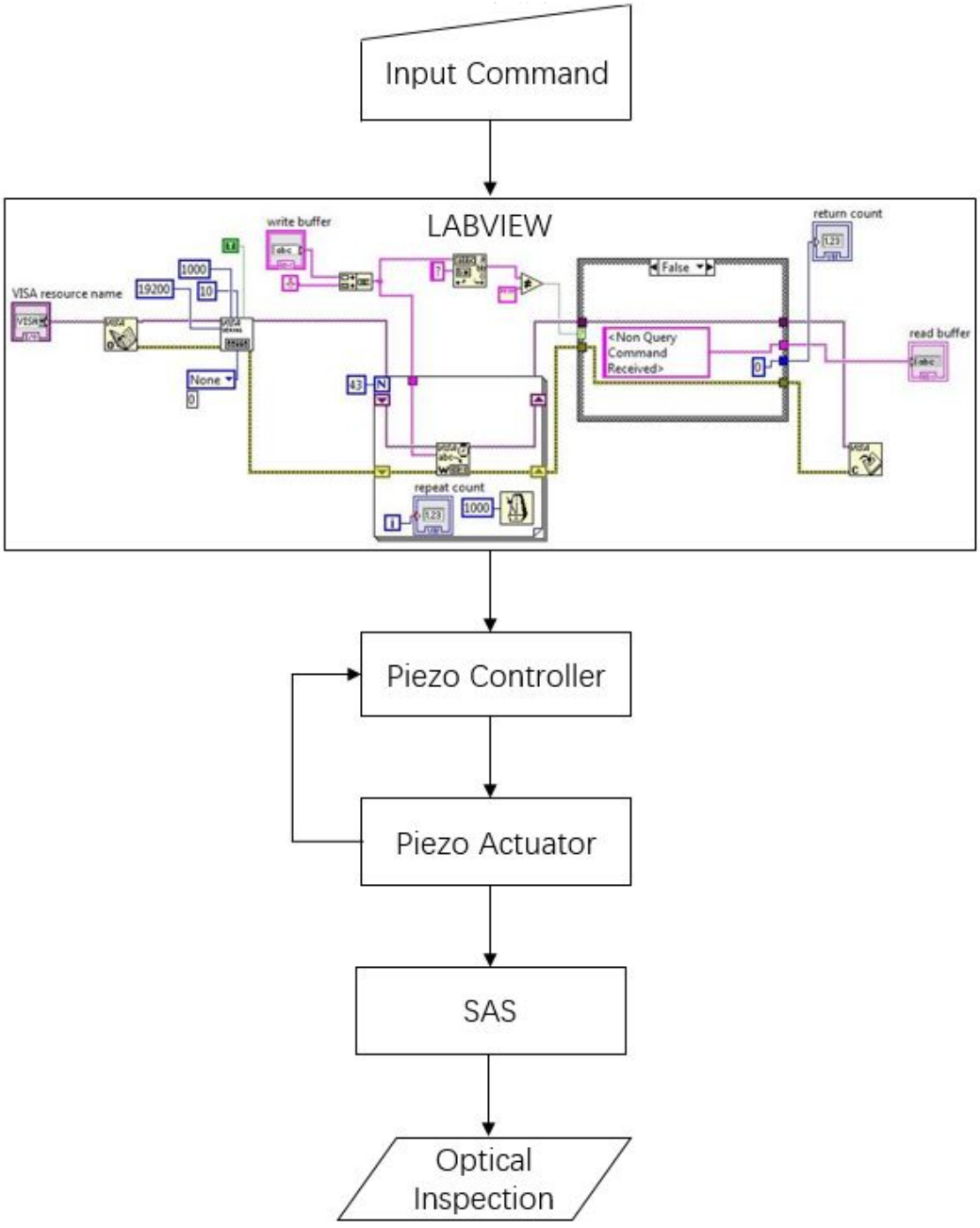

Figure 4.12: Flowchart for piezo actuator based test

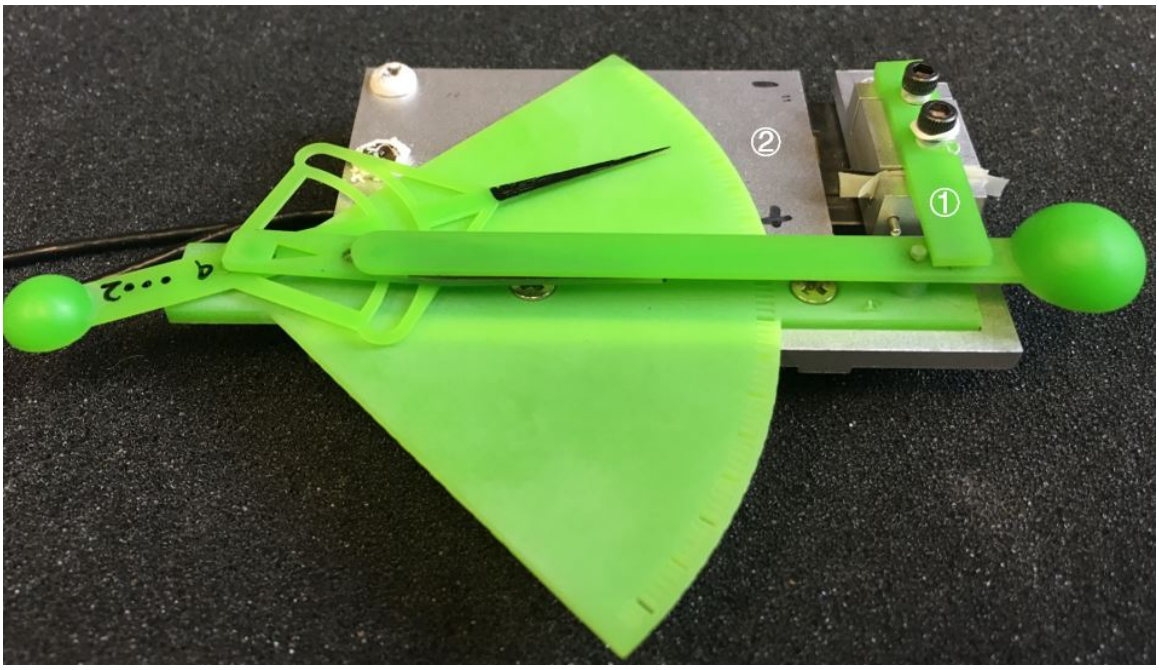

Figure 4.13: SAS with aluminum base on piezo actuator (① Short Sensor Arm ② Aluminum Base

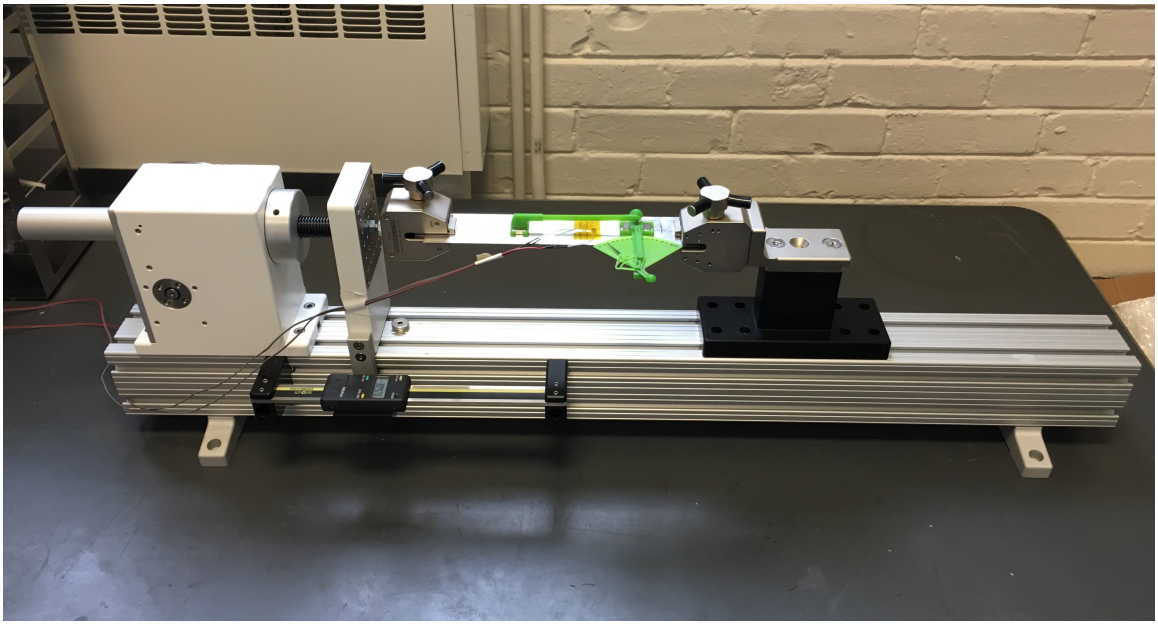

Figure 4.14: SAS on pull tester

This is because, for this sensor configuration, $0.4\ \mu m$ is less than the minimum detectable movement. Inability to control the rate of motor motion resulted in SAS variability for larger step sizes. The motor motion rate is akin to a shock loading and not representative of gradual strain experienced during welding or on a ship, except for slamming conditions. For larger steps, $1\ \mu m$ - $2.5\ \mu m$, the high rate of the applied displacement would result in SAS passing the correct position and rebounding back to a location of lesser representative value. With this in mind, calibration step sizes were evaluated between $0.2\ \mu m$ to $2.5\ \mu m$. Finally it was found that 0.6 μm was most suitable for calibration.

When operating on a perfectly flat plate and installed with proper alignment SAS is a mechanical system with one degree of freedom: translation of the long sensor arm towards or away from the mechanism side. Thus, the device's natural frequency is entirely dependent upon the principle dimensions and build material. The rebounding effect and sensitivity described herein are specific to the SAS configuration being tested. Revising SAS for different ranges of sensitivities, rebounding characterization would need to be re-evaluated. Thereby, it would be possible to avoid this phenomenon given an objective measurement strain rate range. Strain rate ranges would need to be characterized for each application, e.g., hull girder bending, welding processes, and salvage operations. SAS could be designed to minimize rebounding for a given range of strain rate.

For all of the tests performed below including calibration SAS experienced some sticking in the mechanism's range of movement. Sticking is defined as the mechanism failing to react to a change in input displacement for one increment. Applying another increment of displacement would result in a reaction that represents the total input displacement over the past two inputs. This effectively meant SAS would "catch up" and again correctly represent the input displacement. The frequency of this occurrence over all test data points was approximately 5%.

Using $0.6\ \mu m$ as the movement step, five complete passes through tension and compression ranges were conducted, figure 4.15. During each step, the pointer rotation angle

had been recorded in terms of commanded displacement. Plotting the data and fitting with a 4^{th} order polynomial function, the relation between displacement and pointer angle was acquired, figure 4.15. By dividing displacement by the sensor arm's length, the relation between rotation angle with strain is determined.

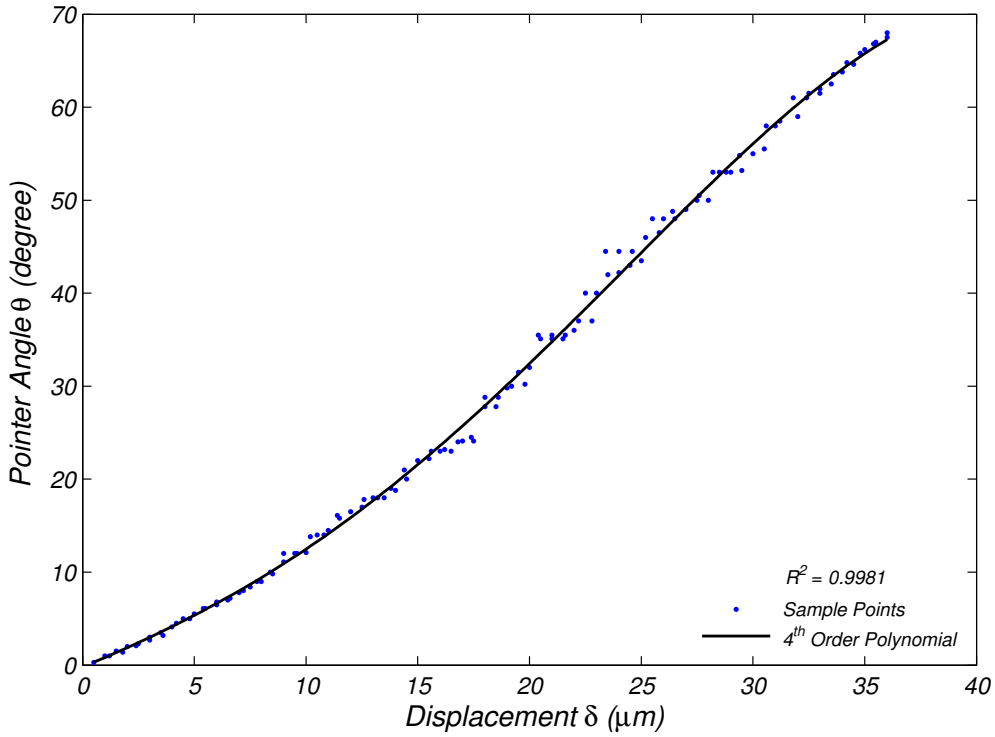

Figure 4.15: Calibration of the SAS mechanism on the piezo motor at 0.6μm step sizes ($\theta = -4E^{-5}\delta^4 + 0.0016\delta^3 + 0.0138\delta^2 + 1.0056\delta - 0.1977, R^2 = 0.9981$)

This polynomial provides the basis for measurement of strain using SAS. For an observed pointer angle and known distance between the two sensor bases (or length of the sensor arm) with strain being:

$$\eta = \frac{\Delta L}{L} \tag{4.4}$$

where Δl is the material length change undergoing tension or compression and l is the original length between two SAS base plates, Δl can be solved for given an observed SAS pointer angle reading.

4.3.3 Repeatability

The repeatability of the results obtained during calibration was examined. Over time, the SAS's mechanical system could be subjected to wear and the measurements could deviate from those at the beginning of its life-cycle. To simulate cyclic deterioration, a total of 50 cyclic stress cycles were induced on the piezo motor test bed. At every 10^{th} cycle the measurement accuracy of SAS was evaluated. Figure 4.16 displays the measurements from SAS at every 10^{th} cycle. SAS consistently is within 5% error from the values measured during calibration.

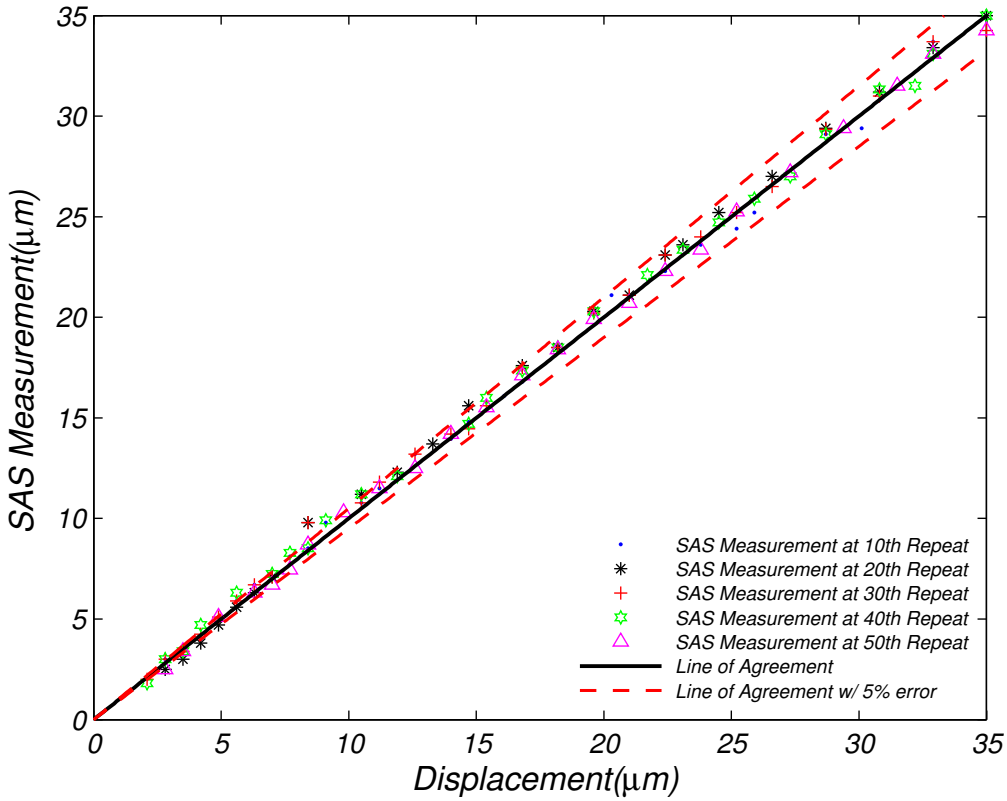

Figure 4.16: Repeatability test over 50 cycles

As can be seen in figure 4.17, the measurement's standard deviation tends to decrease as the number of cycles increases. This is likely because there is something of a break-in period for the 3D printed plastic. Rough edges are smoothed with repeated passes. It

is expected that over time the standard deviation will continue to decrease asymptotically before increasing at some point when the mechanism begins to deteriorate.

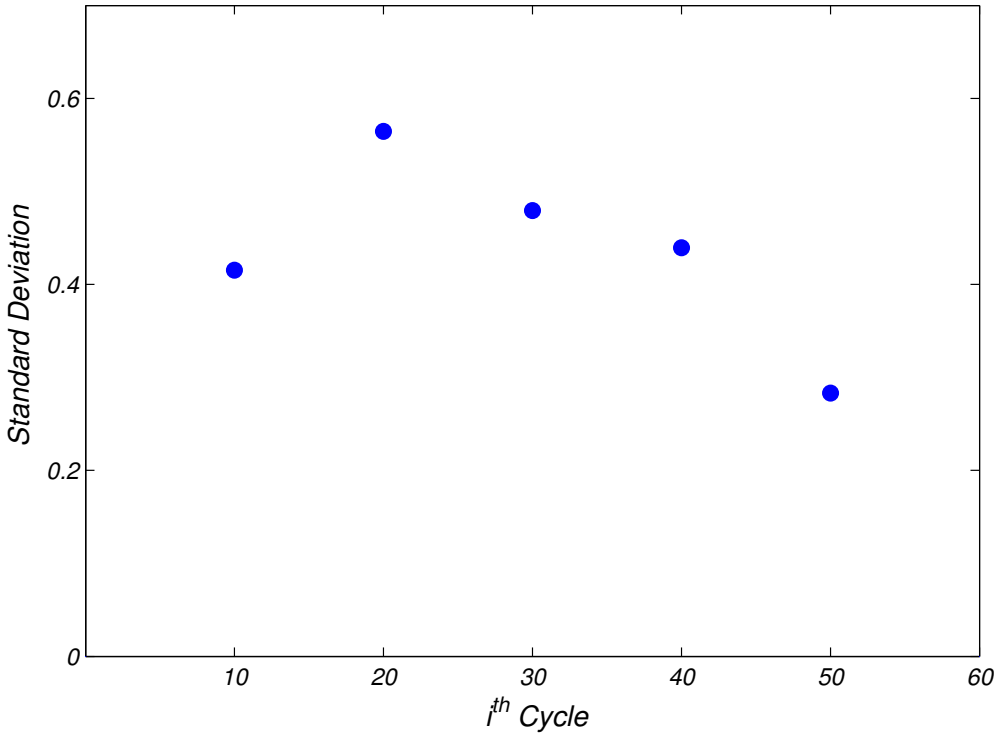

Figure 4.17: Standard deviation of the considered cycle

4.3.3.1 Manufacturing Variability

Since SAS is 3D printed, it is necessary to examine the variation between prints. Four SASs were printed in the same batch and compared. The variability for each SAS after 50 cycles was evaluated.

Figure 4.18 shows the standard deviation of the repeatability test for the four sensors. The results show that three sensors are close in their standard deviation while one is significantly different. This may be attributed to the manufacturing tolerances which are +/- $0.05\ mm$. This pin tolerance range is sufficiently large to induce a loose or tight pin-hole connection.

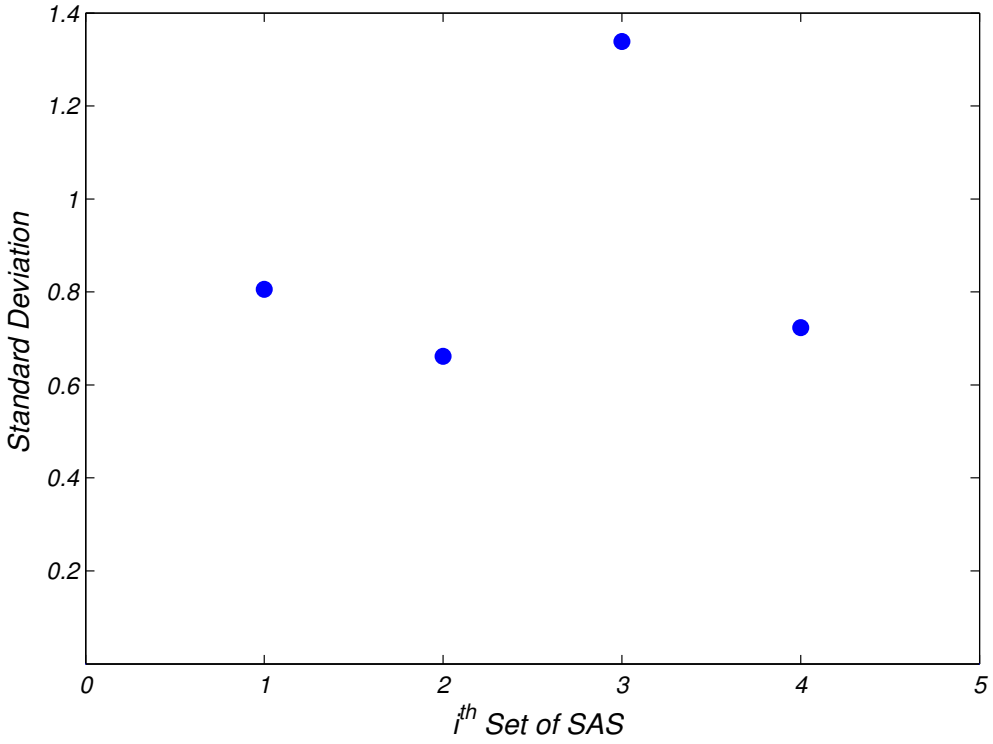

Figure 4.18: Manufacturing variability standard deviation results

4.3.4 Pull Tester Validation

The complete SAS assembly was tested on the pull tester in tensile stress to validate the calibration conducted on the piezo motor. SAS measurements were compared to data from two perpendicular strain gauges accompanied by a 1/4 wheatstone bridge configuration, figure 4.19. Perpendicular strain gauges can offset the temperature influence and wheatstone bridge is capable of measuring small resistance change in strain gauges. A strong agreement between the measurements was observed. The average difference in measurement was 5%.

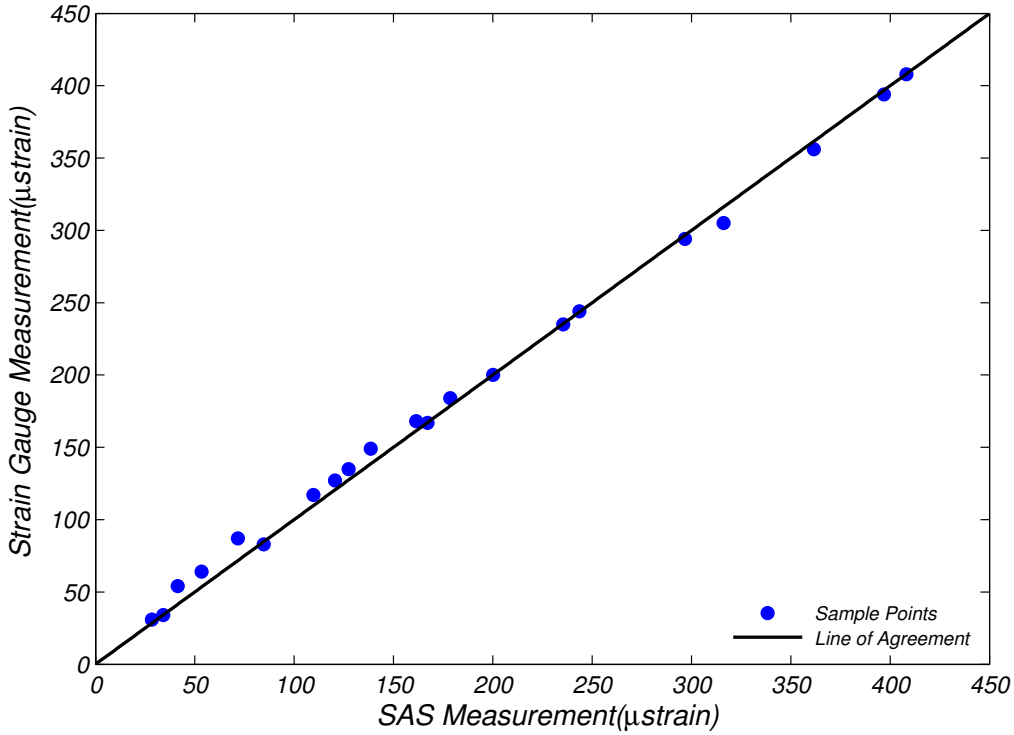

Figure 4.19: Pull tester result

4.3.5 Weld Trial

Weld distortion during fabrication processes can result in significant misalignment of shipbuilding assemblies Mandal and Biswas (2011). Assembly or grand block misalignment

rework is a significant cost during shipbuilding Huang, Harbison, Kvidahl, Niolet, Walks, Christein, Smitherman, Phillippi, Dong, DeCan, Caccese, Blomquist, Kihl, Wong, Sinfield, Nappi, Gardner, Wong, Bjornson, and Manuel (2016). Welders and fabricators need to leave their workstations and bring blow torches and sledge hammers to the issue location and force the fit. By placing SAS adjacent to a weld, stresses that the material experiences are measured in in real-time. Additionally, the residual stress from the weld can be determined. This information can translate to procedural changes and quality control checks that reduce the likelihood of misalignment in the dry-dock and overall rework from weld deformation. To determine if SAS would be capable of strain measurements during welding, a weld trial was conducted.

Two $1/4$ inch thick, 12 inch-across square low carbon steel plates were butt tig welded together with a single pass. Two perpendicular strain gauges with 1/4 Wheatstone bridge were placed at the center of one of the plates. The SAS's sensor arm was centered over top and served as the locator for the rest of the sensor mechanism's installation. Given its proximity to the weld (6 inches), a copper bar was fixed beneath the plate and adjacent to the weld location to help reduce the heat transferred to SAS during the weld process. Figure 4.20 shows the installation setup.

SAS reacted in real-time during the welding process and cool down. Figure 4.21 shows a time lapse of the movement while the weld bead was being laid and thereafter. During welding, the assembly compressed along the weld axis and SAS's measurement corresponded. During cooling, the material's internal compression decreased, and the SAS measured the reduction of stress. SAS remarkably followed the entire strain change process and made it visibly observable without requiring external power, computer, or data acquisition system.

Figure 4.22 compares the SAS measurement and the Wheatstone bridge measurement from the cool down process. SAS and the Wheatstone bridge measurements have similar trends, but with different slopes. This is likely attributed to the difference in measurement

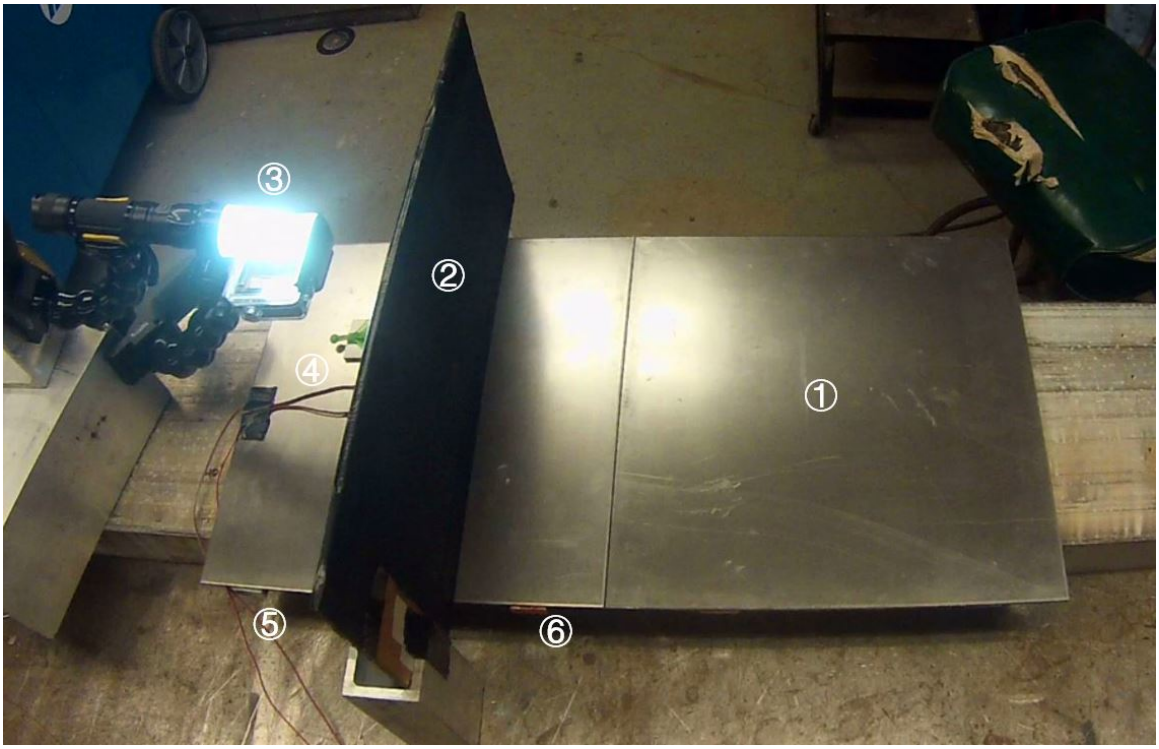

Figure 4.20: Welding preparation (① Steel Plate ② Protection Wall ③ Light and Camera ④ SAS ⑤ Aluminum Bar ⑥ Copper Bar)

characteristics of the two sensor types. An extensiometer would be a better suited benchmark for SAS as it is measuring the strain a $10\ cm$ distance, whereas the Wheatstone bridge is measuring strain over a displacement distance of less than $1\ cm$. In addition, SAS is more susceptible to changes in material topography resulting from deformation. Significant out of plane deformation of the tested plates certainly contributed to the discrepancy.

4.3.6 U.S.C.G. RBM Installation

Measurement data from the SAS costs significantly less to acquire than a conventional strain gauge but is less accurate, making its data well suited for updating the marine structural reliability data synthesis framework capable of interpreting imprecise data. Using permanent set as a sensor for maximum experienced pressure is effective should the maximum pressure experienced yield permanent set. If pressure values remain on the lower regime of the hockey stick trend, permanent set does not have the sensitivity to deduce the

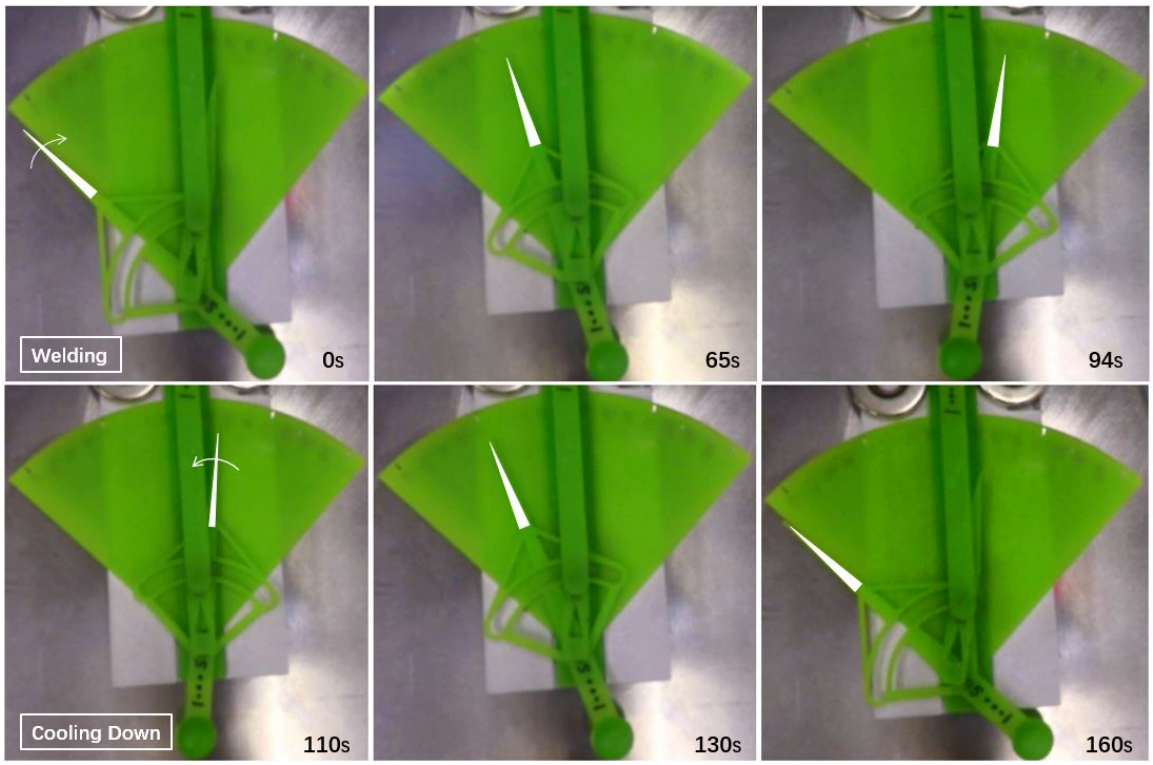

Figure 4.21: SAS movement during welding test (the first row indicates pointer was moving clockwise and steel was compressing during welding; the second row shows pointer was moving back counterclockwise which means steel was relaxing during the cool down process.

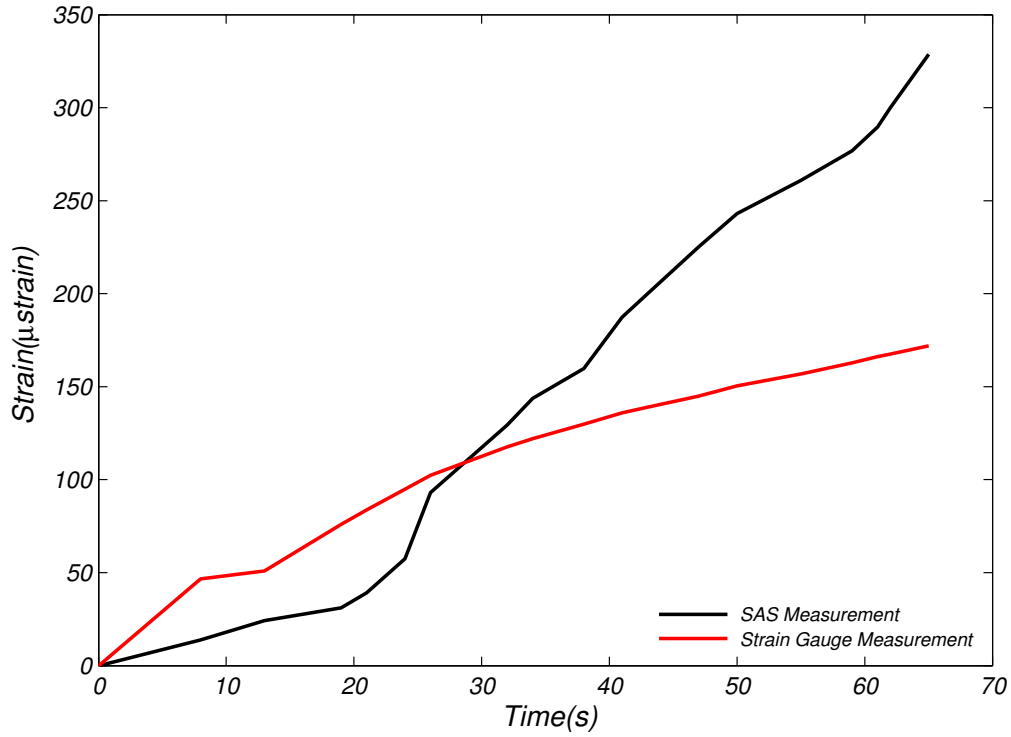

Figure 4.22: Distortion due to welding as measured from the piezoelectric strain gauges and SAS during cool down.

maximum pressure. The SAS effectively fills in this lower maximum pressure data gap. Contributing to the low data acquisition cost is the simplicity of installation and data acquisition; figure 4.23 depicts the conventional system and support equipment on the left and the complete SAS system on the right.

Figure 4.23: Equipment caparison, conventional system to the left and SAS to the right

On October 13th, 2014 at Cape Disappointment, Oregon, a U.S. Coast Guard Response Boat-Medium (45RBM) was instrumented with three Strain Amplification Sensors. The 45RBMs are designed to operate safely in seas up to 12 feet with 50 knot winds with 100 tons of displacement in tow load. There is concern for the structural integrity of the vessel operating in seas over 8 feet. Of particular concern is the bow region which sustains significant stresses in slamming when operating in higher sea states.

In collaboration with Professor Jerry Lynch's group and as a part of a Naval Engineering Education Center project, the sensors were mounted in the auxiliary machinery compartment alongside a string potentiometer measuring displacement between frames. Two SASs were mounted on the shell plating between the stiffeners and one was mounted on a

cantilever bridge spanning two frames, figure 4.24.

The three sensors were identical except for a hole location on the actuator arm which provided an increased or decreased 30% range of strain amplification from the standard sensor. Since a larger displacement was expected to be experienced over the span between the frames, the lower amplification was placed on the bridge while the 30% increased amplification and baseline were placed on the shell plate. Designs for augmentation of the SAS to record maximum experienced strain existed at the time of testing, however, further iterations in prototype manufacturing were necessary to realize a functional prototype. Thus, a camera was mounted with all three sensors in the frame of view and video was recorded throughout testing. Review of the footage to examine the location of the pointer arm on the measurement face was then completed to determine an approximate experienced strain. Unfortunately, the material used for the string potentiometer proved to stretch itself and resulted in imprecise comparison data. However, based on the successful bench test and weld test, it is likely SAS's data would perform with similar reliability as experienced in the lab environment.

It was determined that SAS could successfully operate on-board a marine structure during operation. SAS's ability to properly measure strain was not confirmed; however, it was discovered that increased amplification would be necessary to observe strain on the particular details being monitored. This has been achieved with subsequent SAS designs producing amplification on the order of 6000 times in comparison with the 300 time amplification design tested on the RBM.

4.4 Conclusion

The patented SAS is the world's first 3D-printable strain gauge. SAS provides real-time strain measurement with tunable sensitivity, measurement range, and attachment orientation. SAS is stand-alone; it requires no energy source for operation, can be rapidly installed

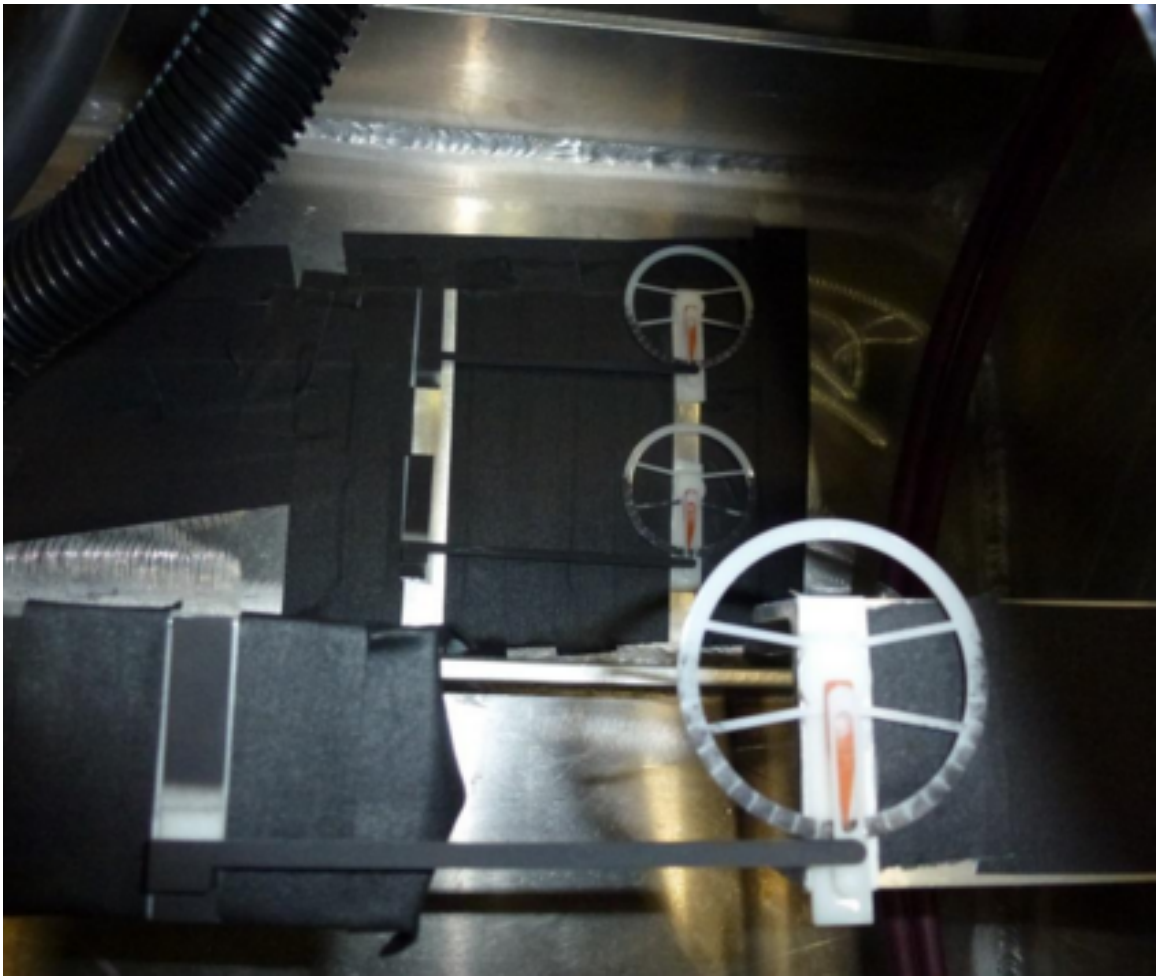

Figure 4.24: SAS installation on side shell and cantilever bridge between frames 8 and 9

using magnets, and is intrinsically safe. SAS is a cost-effective solution for monitoring large vessel structures or residual stresses during welding processes. The above presented calibration, repeatability testing, and manufacturing variability testing all demonstrate that the SAS, in a small footprint, can accurately and repeatedly measure strain measurement on the order of single microstrain.

Future work will further evaluate the reaction of SAS to significant topology changes on the material being measured, temperature compensation, a robust mechanical maximum value recording technique and a mechanical time history recording capability.

CHAPTER 5

Fusing Structural Damage Measurements for Route Planning Decision Support

5.1 Introduction

Assessing and managing a damaged ship is one of the most man power intensive activities onboard. As modern ships continue to reduce manning, optimal decision-making in the event of damage is critical. As was demonstrated in Chapter 3, fusing data with significant uncertainty can be accomplished within BN frameworks. Extension of static BNs to DBNs generates the basis for modeling a dynamic system, and further extension to an ID yields dynamic decision support in the form of a DID. Chapter 4 presented SAS, a tool that can be deployed rapidly for framework updating with relevant evidence. Combining the rapid data collection capability of SAS with an interpretive and data fusion enabling framework produces a real-time decision support tool. Real-time decision support is particularly relevant to situations after vessels sustain damage. Very limited application of data fusion frameworks and decision support tools has taken place within the realm of marine DCS. Post-damage decisions are presently made with a very limited understanding of the structural state of the vessel as well as the decision's effect on the future state of the structure.

5.2 Literature Review

A range of damage support tools exist to analyze ship stability post-damage. These tools provide the user with strategies to prolong the eventual loss of stability and predict the time until instability occurs. Stability loss usually leads to vessel capsize or sinking. Thus, an evacuation plan can be developed from the tool's prognosis. However, unlike stability, the structural failure mode and amount of time available to evacuate the ship may not be predicted easily and may lead to indecision (Bole 2007). Additionally, emergency response crews often have limited access to information pertaining to the vessel's structural state and, therefore, are unable to make informed decisions that range from abandonment, stabilization activity, structural reinforcement, or changing course.

Modern ship complexity and limited manning requires the use of a DCS to aid crew in the event of an accident or hazardous situation. For events such as fire, flooding, chemical contamination, or threats to critical systems, the DCS aims to provide crew with situational awareness and recommendations for counteractions and reconfiguration. Santos and Soares (2011) identified that survivability can be best determined from the damage condition, loading condition, sea state at the time of accident, and location of damage in three axes. The location and type of damage, and sea state require stochastic descriptors. Thus, combining problem identification and action planning while accounting for uncertainty is necessary to provide this information. However, there has been very limited application of decision support and expert systems to DCSs to ensure the safety and operational stability of modern ships Calabrese et al. (2012). Of the systems in place, most address stability but fail to consider structural integrity and the compounding effect the loss of structural integrity can have on stability Bole (2007). Further, there is a lack of investigation into decision-making or support thereof for a damaged vessel's route planning.

Calabrese et al. (2012) presented a hybrid KDSS integrated into a DCS for identification and management of events that could result in vessel damage or the endangerment of the crew. A decision-making system was proposed by Balmat et al. (2011) using a fuzzy

approach to evaluate the maritime risk to safety at sea, and more particularly pollution prevention. For flooding decision support, Hu et al. (2013) presented an M-H (Ma Kun and Hu Li-fen, family names of the method's developers) method-based decision support system (MHDSS) to evaluate survivability and provide real-time decision-making assistance. However, none of these works consider the vessel's structure in DCS decision support strategies. This work introduces a DID for course selection post-damage decision support. This preliminary network fuses data from a novel 3D printable strain gauge, the SAS, that can be rapidly deployed to critical locations on the structure, and visually inspected measurements of crack growth. Optimal decision policies for both speed and heading are produced to advance the vessel towards a target line.

There has been limited but successful implementation of DBNs and IDs in the realm of deterioration and route planning. Strauss and Frangopol (2013) introduced a DBN that leverages a structure akin to a DID in order to produce an algorithm for optimal risk-based planning of inspection. Lou, Yin, and Li (2011) proposed the only other application of BNs to path planning–an interactive DID framework with communication capabilities, called Com-I-DIDs, focused on the communication and coordination of cooperative agents in a dynamic environment. However, this work does not apply to a single agent system where the agent aims to maximize its own utility as is the case of a damaged ship.

A BN framework allows for data synthesis and input of inspection evidence for more accurate prognosis. Chapter 3 demonstrated the ability of the framework to effectively fuse data gathered with uncertainty and demonstrated the framework's ability to provide decision support based upon the updated, more accurate models. By extending this framework to a DID, it is capable of providing decision support in real-time. The 3D printable SAS has been tested and proven to be a rapidly deployable, robust, and inexpensive alternative to piezo-electric conventional strain gauges. Uniting evidence from the SAS and crack length with a DID (DBN augmented with utility and decision nodes) produces the basis for damage state decision support strategies.

The DID model presented in this work demonstrates the routing decision support from evidence provided by the SAS measuring extreme stresses and visually inspected crack propagation. The fatigue crack propagation is modeled using Paris' law. The vertical bending moments that are experienced based on speed and heading decisions follow Jensen's method Pedersen and Jensen (2009). Extreme vertical bending distributions are based on Mansour's upcrossing analysis Mansour (1994). The BN model is instantiated for each timestep where a heading or speed decision is made and evidence including stress from the SAS, and crack length are fused through Bayesian inference. Routing choices based on evidence from both the SAS and visually inspected crack length are evaluated together and separately. The network's ability to adapt the aggressiveness of the chosen route provided evidence is demonstrated.

This section will proceed by giving a brief overview of the fatigue model, probabilistic loading, as well as of network structure. The network's ability to fuse extreme stresses from the SAS and crack propagation measurement for better routing decisions is investigated and compared to routing policies without evidence. Examples that impose evidence for strain gauges, and fatigue crack propagation, individually and in combination, will be shown followed by a discussion of the results and conclusions.

5.3 Proposed Framework

The framework includes the use of a probabilistic extreme vertical bending moment model, a deterministic vertical bending moment model based upon a chosen heading and speed, a deterministic crack growth model, and an additive utility function. These models are integrated into a BN framework and coupled with the utility functions and decision nodes to produce an ID. With network instantiations at timesteps for each inspection or routing decision point, a DID is created. Bayesian inference is performed at each timestep to interpret evidence of crack growth and SAS maximum strain measurement to provide optimal

routing decision policies.

5.3.1 Fatigue Crack Growth Model

The deterministic fatigue model used herein is the Paris-Erdogan law for crack growth, Stephens and Fuchs (2001). The stress is assumed to be homogeneous and uniaxial with constant cyclic stress range S. Stresses are intensified at the crack tip. Based on linear elasticity theory, a stress intensity factor, $\sqrt{\pi x}$, is introduced where x is half the crack length. The crack modeled herein is located on the center of a deck plate.

$$\Delta x = C(\sqrt{\pi x}S)^m \tag{5.1}$$

C and m are experimentally determined constants and considered to be $8.47 * 10^{-14}$ and 3.5 respectively. If the crack length increment is considered small compared to the variation of $x^{(m/S)}$, Δx can be idealized to the differential quotient dx/dn where n is the number of cycles. Thus, equation 5.1, becomes a differential equation where x and n can be separated, resulting in equation 5.2 Ditlevsen and Madsen (1996).

$$X(n) = \left[(1 - \frac{m}{2})C * \pi^{m/2}S^m n + X_1^{1-m/2}\right]^{(1-m/2)^{-1}} \tag{5.2}$$

Where X_1 is the initial crack length.

5.3.2 Vertical Bending Moment Models

Two models for VBM were used. A deterministic model produces the RMS VBM value for a chosen speed and heading, and a stochastic model determines the extreme vertical bending moment distribution. Combining these two models in the BN framework provides a synthesized expected crack length from a chosen heading and speed with or without evidence from the present or prior crack lengths and extreme strain values produced by the SAS.

Assuming a short period of time, ocean waves can be modeled as a stationary Gaussian process with zero mean Mansour (1994). Given a linear marine structure, the load process is also Gaussian and the extreme load distribution can be found using methods such as upcrossing analysis and order statistics. For the case of a narrow-band process, Mansour recommended use of the upcrossing analysis due to its ease and accuracy. The corresponding equations are shown below.

$$F(x) = exp\left(- \upsilon_0 T e^{-0.5\left(\frac{x-m_s}{\sqrt{m_0}}\right)^2} \right) \tag{5.3}$$

$$\upsilon_0 = \frac{N}{T} \tag{5.4}$$

Where m_s is the still water bending moment, $\sqrt{m_o}$ is the RMS wave bending moment, T is the considered period, and N is the number of wave moment peaks in the period T. Equation 5.3 produces the extreme bending moment cumulative density function distribution which is encoded as a prior distribution in the network.

Since the network aims to provide support for heading and speed decisions, it is necessary to understand the implication of a chosen heading and speed on stress and ultimately safety through the resulting crack growth provided by equation 5.2. Sorensen (2011) provided a closed form semi-analytical method that produces both frequency response functions and standard deviations for the wave-induced bending moment for mono-hull ships. The method assumes a homogeneously loaded box-shaped vessel and yields the basis for the frequency response function by using linear strip theory. Correction factors for speed, block coefficient, and oblique seas are then added. The resulting standard deviation of the wave-induced bending moment amidships is:

$$s_m^2 = (F_v(Fn)F_{Cb}(C_b))^2 \int_0^\infty \Phi_M^2(\omega) S(\omega) d\omega * |cos\beta|^{1/3} \tag{5.5}$$

Where F_v, F_{Cb} , Φ_M, and $S(\omega)$ are the speed correction, block coefficient correction for values less than or equal to one, the frequency response function, and the frequency dependent wave spectrum respectively. Waves are modeled by a Person-Moskowitz (ISSC) wave spectrum. The appended cosine term is the oblique seas correction.

5.3.3 Dynamic Influence Diagrams

Dynamic systems operating with real-time feedback require adaptation of the conventional static BN to produce relevant information. A BN is a probabilistic graphical model representing a set of random variables and their conditional dependencies via a DAG compactly encoding full joint probability distributions Kjaerulff and Madsen (2008). A DBN interprets past static networks instantiated for each instance in time and adds new networks for each future time slice. This representation is known as unrolling the dynamic model for the desired number of timesteps. For a given point in time, a DBN is static as it consists of a discrete set of static networks representing all past time slices and future points in time for which a prognosis is desired.

Through the addition of utility functions and decision nodes, it is possible to use BNs as a decision support tool. Networks augmented with the utility functions and decision nodes are known as IDs and are compact representations of a joint expected utility function. The solution to a decision problem is a matter of determining the strategy that will provide the highest utility value to the decision maker. Therefore, construction of a utility function accurately representing the value of the potential strategies is critical to the effectiveness of the influence diagram's ability to provide decision support. Similar to a BN, IDs rely on the chain rule for finding the expected utility for each action, a, in determination of $P(h_j|\epsilon)$, with ϵ as evidence, and h hypothesis.

$$EU(a_i) = \sum_j U(a_i, h_j) P(h_j|\epsilon) \tag{5.6}$$

Utility functions provide a utility value for each combination of related node states. After performing inference with the provided evidence, the maximum expected utility value is determined and the corresponding strategy states are selected and presented as the optimal decision given the evidence provided.

5.3.4 Framework Construction

Using a BN topology to produce path planning support requires careful construction to minimize likelihood of intractable results. Should each timestep require exact knowledge of the position of the vessel, all prior decisions for speed and heading would need to be known. If the location's exactness is loosened and the navigable area is covered by a grid discretization, the prior location and last speed and heading decision are still necessary pieces of information. This method still becomes increasingly intractable as the number of timesteps increases. This is because the number of states for each location node is required to be the number of grid bins by the number of heading angles by the number of speeds; and sufficient discretization of the navigable area requires on the order of hundreds of location bins.

Figure 5.1 depicts the initially conceived and intractable DID conceived for route planning. Initially, the network was aimed at path planning to a specific point instead of a line of safety. To do this, the network needs to be aware of the vessel's location. Location awareness requires knowledge of every prior heading and speed decision made since the initial starting position was established. Thus, the following network was constructed to represent such a model. Intractability was created by the edges entering utility functions. Each utility function requires the knowledge of all prior decisions made for both heading and speed and edges are placed accordingly. Therefore, the number of dimensions within the utility function increases exponentially over time. This network also included crack growth parameters which were later rolled in to the random crack variable a. It was realized that the utility function construction would need to be such that it is independent of

prior decisions. This led to the line of safety objective which is discussed below. Since the position of the vessel relative to the line of safety does not affect the associated value for speed and heading decision-making, this construct was recognized as tractable.

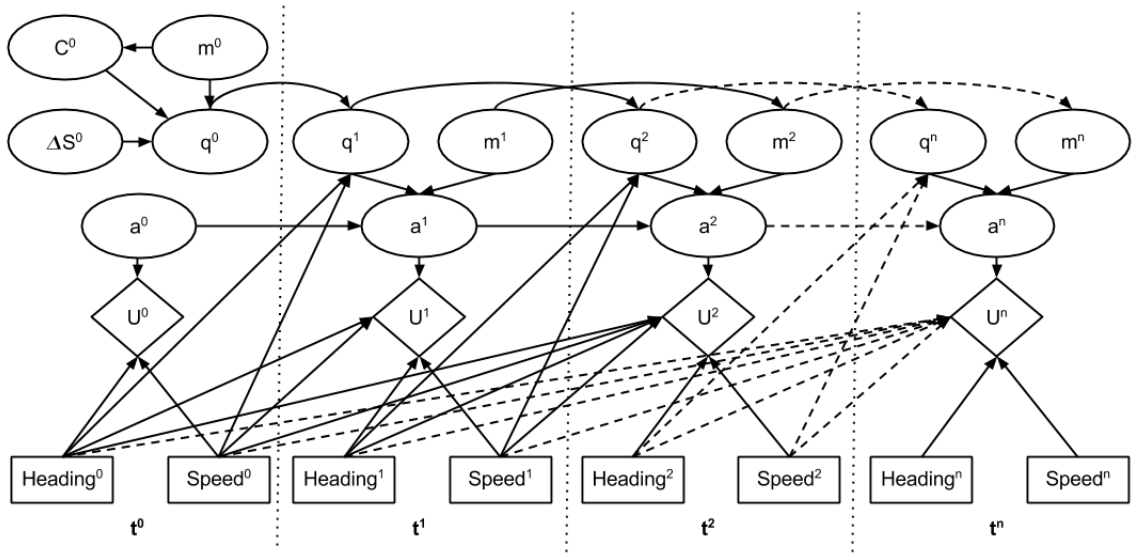

Figure 5.1: Route planning DID with location dependent utility functions.

Since equation 5.5's method accounts for both speed and heading in VBM calculations, both were initially considered as decision nodes. Two problems arose with this construction. First, the *HUGIN* engine uses a greedy search algorithm to evaluate the DID which suffers from sometimes inaccurate policy selection. Of particular challenge to the greedy algorithm, which aims to maximize its gains on each search layer, is a utility function with two decision nodes to be determined simultaneously. This made results unclear as to whether the algorithm had converged upon a global or local optimum. Additional runs were not sufficient to determine optimality as the solution would often get stuck at local optima and require insertion of evidence to shift the search. Removal of evidence to yield the same conditions prior to its application would often lead to different optima locations.

Second, it was discovered that the trade space between speed and heading governed by equation 5.5's VBM formulation always favored reducing the aggressiveness of the heading over reducing speed to lower the VBM. In other words, within the operational profile of the

tanker, the fastest speed it can travel should always be chosen and adjustment to heading should be used to control the experienced VBM.

The partials of RMS VBM with respect to speed and heading can be easily ascertained from figure 5.2 and we can gather that the heading angle contributes twice as much to the RMS VBM as does the speed per degree and knot respectively. The final plot shows the relationship between speed, heading, and advancement towards the target. In this case we can see speed contributes more than heading to advancement. Since speed has half the effect on the VBM's RMS value when compared to heading, and contributes to advancement more significantly, it is always in the best interest of the operator to maximize speed and toggle heading until the maximum allowable RMS VBM value is reached.

By removing utility function dependence upon location, the network was constructed in a manner that does not require knowledge of location at each timestep. This is possible because the objective is to pass through a line of safety, figure 5.5, and consideration is not given to the vessel's particular point of crossing, i.e. motion parallel to the line of safety. In addition, the proximity to the line of safety does not effect the utility.

The software, *Hugin Researcher*, used to solve the DID assumes additive utilities between the timesteps. To remain consistent within the boundaries of a timestep, the utility function was also constructed as an additive function. Expected utilities from different timesteps are summed to determine the optimal decision within a DID. The utility function can be seen in equation 5.7 with weighting parameters as factors on the two components. It was constructed to account for the diminishing safety as the crack length increases, a, relative to a critical length of $4000\ mm$, and the cost of the route relative to most expeditious option, advancement.

$$U(speed, heading, a) = Safety(a) * \alpha + Advancement(speed, heading) * \beta \quad (5.7)$$

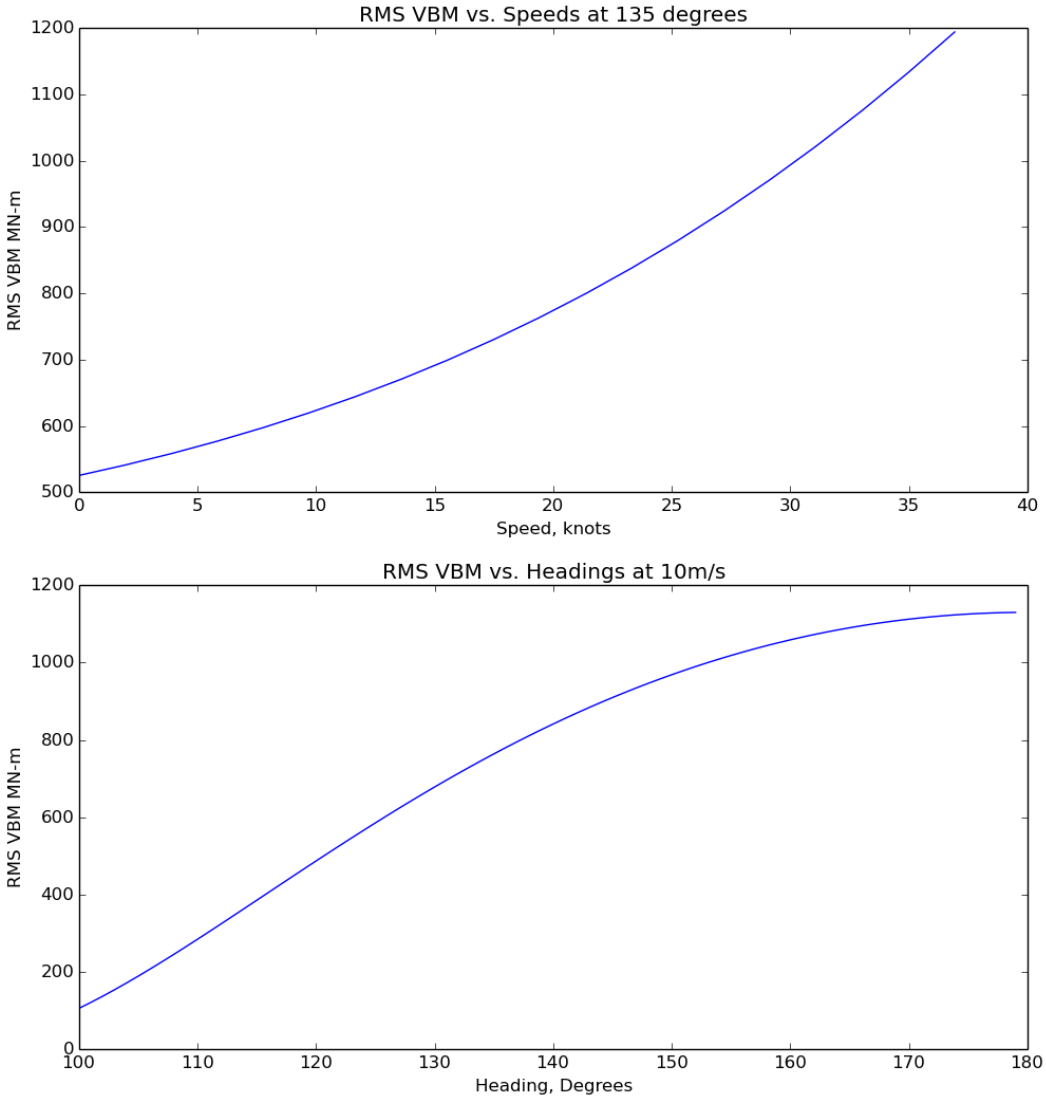

Figure 5.2: RMS VBM vs. speed and heading for Mansour's tanker in two dimensions

The safety function is governed by a exponentially decaying curve, equation 5.8. Alternative linear and sigmoidal functions were considered; however, since safety diminishes at an increasing rate with crack growth, this was thought to be the most suitable representation. Critical crack length was assumed to be $4000\ mm$. Within the network, only the crack length bin can be used to evaluate the utility function. Thus, instead of using $4000\ mm$ and the actual crack length, their corresponding bins are used as input into the safety function.

$$Safety(crackbin) = crackbinCritical^2 - \left[\frac{crackbin}{crackbinCritical}\right]^2 \tag{5.8}$$

Advancement is governed by a linear function–the ratio of advancement for a given speed and heading to the range between the maximum and minimum possible advancement. Maximum advancement for the chosen speed is at an 81 degree heading and the minimum at 0 degrees, equation 5.9. Figure 5.3 displays the advancement relationship over a range of speeds and headings.

$$Advancement(speed, heading) = \frac{cos(heading)speed - cos(81)speedMax}{cos(0)speedMax - cos(81)speedMin} \tag{5.9}$$

Thus, the BN graph naturally falls out from the utility function construction to produce edges from the heading decision nodes depicted as rectangles to the utility function, a diamond, figure 5.4. The VBM function node is dependent upon the chosen speed and heading following equation 5.5. RMS VBM in addition to a prior crack length and an error term produce a distribution for the crack length. From one timestep to the next, temporal links from an error term carry a belief in conditions being more or less severe than modeled. Larger stress cycles, a greater number of stress cycles between timesteps, material resistance to fatigue crack propagation, or any other factor that may cause the crack propagation rate to deviate from the encoded model, is accounted for via updating of the

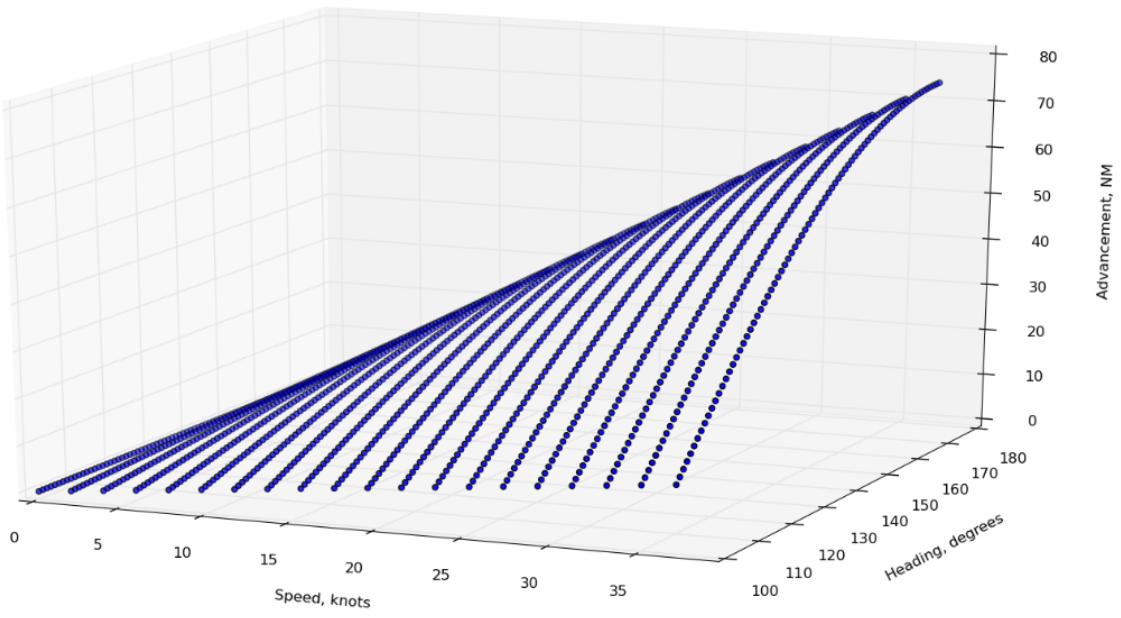

Figure 5.3: Display of the utility function advancement term over a range of speeds and headings.

error node. Both crack length and SAS measurements are as a result of the environmental conditions and therefore are children to the error term. Temporal links are between crack length and error nodes. All elliptical nodes are random variables except for the VBM node which is a function node.

Initially, the error node follows a normal distribution and the crack length follows a right-skewed Gumbel continuous random variable with scale = 0.35. Table 5.1 displays the discretization of the network nodes. Error values are multiplied by the crack length bin and VBM value to shift their distributions accordingly. The network is very sensitive to the discretization technique used for crack growth. This sensitivity is due to the utility function's dependence upon the crack bin number and not the underlying crack length, and the network's ability to recognize differences in crack growth for heading choices. To achieve encoding that would best discriminate between possible crack lengths within the constructs of the network, the best fit polynomial function of an ordered list of all possible crack lengths for the decision combinations encoded was used as the interval boundary

function.

Variable	Probable Range	Number of States	Interval Boundaries
a (mm)	3000-40000	50	$0, 3008 + 12bin - 0.25bin^2 + 3.7e - 03bin^3, \infty$
SAS (MPa)	45-450	50	$0, 45(450/45)^{bin/50}, \infty$
Error	0.6-1.4	9	$0, 0.6 : 0.1, \infty$
Heading (degrees)	0-81	10	$0 : 9 : 81$

Table 5.1: Route Planning Network Dicretization

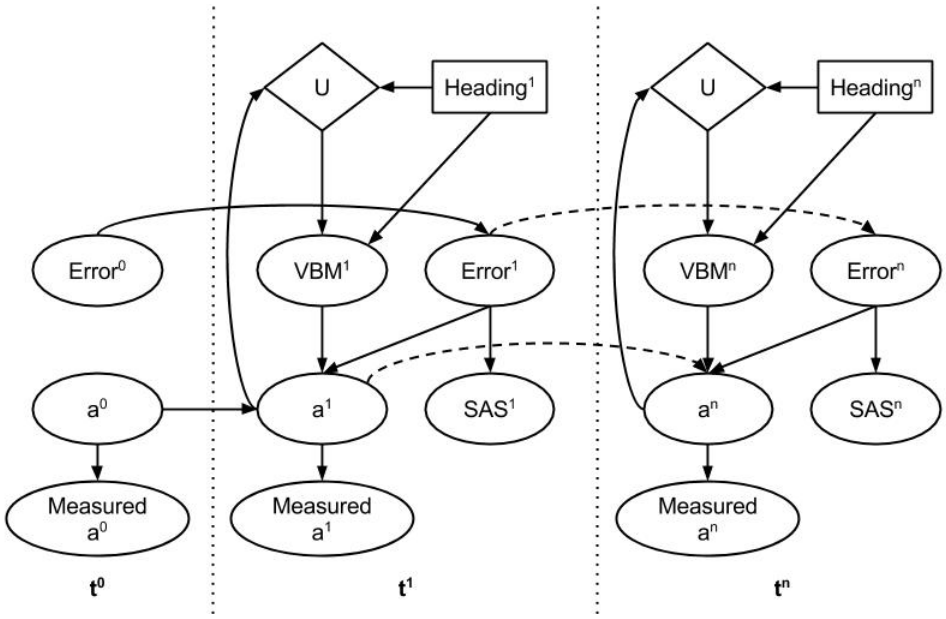

Figure 5.4: Route planning DID with location independent utility functions. The diamond nodes are utility functions, rectangles are decision nodes, and ellipses are random variables.

The network construction shown in figure 5.4 is the version that was finally chosen and found to be tractable. Speed was removed from network encoding as was the specific location of the vessel. A line of safety objective was introduced instead which allows for tractable computation for decision support of route planning.

5.4 Case Study

5.4.1 Considered Vessel

The tanker from Mansour (1994) was used as the considered ship operating in a storm and after sustaining damage. Damage was assumed to degrade the midship's moment of inertia to 80% of the intact condition and the operating speed was fixed at 10 knots. Table 5.2 provides particulars for the vessel and storm operating conditions.

Length (m)	232.6
Depth (m)	16.6
Beam (m)	32.1
Draft (m)	12.2
Block Coefficient (Cb)	0.82
Still Water Bending Moment (SWBM) (MN-m)	1814.8
Crack distance from N.A. (m)	7.5
Wave Height (m)	6.1
Wave Period (s)	12

Table 5.2: Considered Vessel and operating conditions

The detail being monitored for crack growth was located 6.1 meters from the vessels neutral axis and was subjected to in plane cyclic stresses governed by equation 5.5's VBM formulation.

5.4.2 Real-Time Route Planning Decision Support

The BN outlined previously (figure 5.1) was tested using simulated evidence sets of fatigue crack growth and SAS readings. Five network timestep initiations were considered where each timestep was 90 minutes. In all cases, the vessel's objective was to pass a line of safety running perpendicular to the direction of the sea, as shown in figure 5.5. Optimal decisions are produced with and without evidence. When evidence is provided on crack length or SAS nodes, it is required that the decisions prior to the evidence timestep be made. In all cases, the decisions made are those that maximize expected utility.

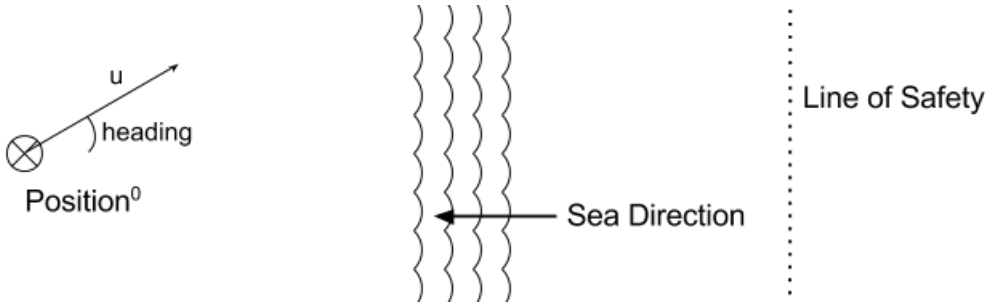

Figure 5.5: Objective diagram

First the network was evaluated without evidence from the SAS or the crack growth length , table 5.3. Next, the network was evaluated with evidence from both crack measurements and SAS measurements in combination and separately. Evidence was provided on each timestep after the previous timestep's heading decision was made. To evaluate the reaction of the decision-making to either high or low measurements of the crack length and SAS, consistent high and low pieces of evidence were provided at all timesteps. For crack length, a "high" piece of evidence is a crack that is longer than the mean. A "high" SAS piece of evidence is a measurement indicating an extreme stress higher than the mean. Evidence was selected based on the posterior distributions from the prior timestep decisions. At the 0^{th} timestep, the damage has just occurred and it is not reasonable to expect evidence from the crack length or SAS to be available. Thus, all routes are the same initially regardless of the evidence set.

Tables 5.3 and 5.4 and figure 5.6 show the results for updating with evidence that was selected to be the bin furthest from the mean and with a probability of greater than or equal to 10%.

Evidence was also provided in the bin adjacent to the posterior mean values from prior decisions to evaluate whether there would be a shift in the optimal policy even with evidence that is not significantly different from that which is most likely, tables 5.5, 5.6, and figure 5.7.

Adjusting the utility function weighting parameters to increase the weight on the ad-

Evidence		timestep				
Type	Set	0	1	2	3	4
	1) No Evidence	-	-	-	-	-
High	2) SAS (MPa)	-	95	82	86	99
	3)Crack Length (mm)	-	3058	3104	3128	3150
	4) SAS (MPa)	-	95	86	86	99
	Crack Length (mm)	-	3058	3077	3095	3157
Low	5) SAS (MPa)	-	78	86	82	90
	6) Crack Length (mm)	-	3014	3014	3048	3135
	7) SAS (MPa)	-	78	86	82	90
	Crack Length (mm)	-	3014	3037	3058	3112

Table 5.3: Evidence values from both SAS and crack length individually and in combination with evidence in bins with a greater than or equal to 10% posterior probability. Utility values $\alpha = \beta = 1$

	Course Result	
Evidence Set	Crack Length (mm)	Advancement (NM)
1)	3107	49
2)	3053	41
3)	3053	41
4)	3040	38
5)	3384	65
6)	3622	72
7)	3765	78

Table 5.4: Resulting mean crack lengths and advancement distances towards the line of safety for optimal heading selection given combinations of updating with evidence from both SAS and crack length individually and in combination with evidence in bins with a greater than or equal to 10% posterior probability. Utility values $\alpha = \beta = 1$.

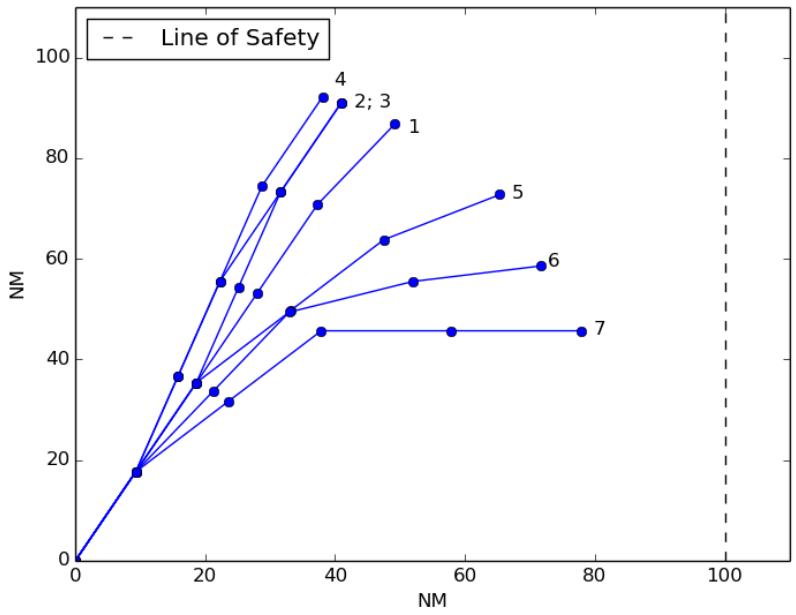

Figure 5.6: Courses from updating with evidence from both SAS and crack length individually and in combination with evidence in bins with a greater than or equal to 10% posterior probability. Utility values $\alpha = \beta = 1$

Evidence		timestep				
Type	Set	0	1	2	3	4
	1) No Evidence	-	-	-	-	-
High	2) SAS (MPa)	-	90	95	82	95
	3)Crack Length (mm)	-	3037	3068	3095	3135
	4) SAS (MPa)	-	90	95	99	99
	Crack Length (mm)	-	3037	3077	3128	3177
Low	5) SAS (MPa)	-	82	86	90	82
	6) Crack Length(mm)	-	3014	3026	3068	3120
	7) SAS (MPa)	-	82	82	82	90
	Crack Length (mm)	-	3014	3048	3058	3128

Table 5.5: Evidence values from both SAS and crack length individually and in combination with evidence in bins adjacent to the mean posterior bin. Utility values $\alpha = \beta = 1$.

	Course Result	
Evidence Set	Crack Length (mm)	Advancement (NM)
1)	3107	49
2)	3066	44
3)	3107	49
4)	3053	41
5)	3507	69
6)	3259	59
7)	3561	71

Table 5.6: Resulting mean crack lengths and advancement distances towards the line of safety for optimal heading selection given combinations of updating with evidence from both SAS and crack length individually and in combination with evidence in bins adjacent to the mean posterior bin. Utility values $\alpha = \beta = 1$.

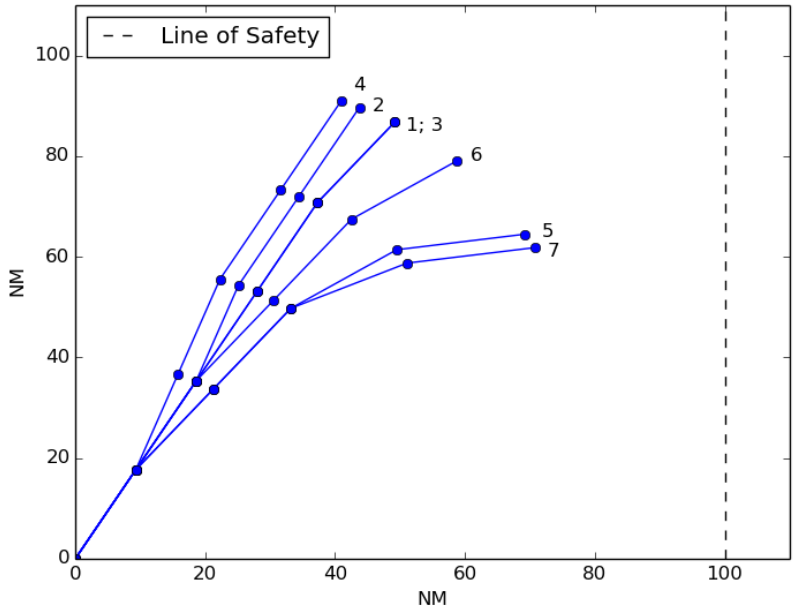

Figure 5.7: Courses from updating with evidence from both SAS and crack length individually and in combination with evidence in bins adjacent to the mean posterior bin. Utility values $\alpha = \beta = 1$

vancement term with $\beta = 1.2$, the results were evaluated with evidence in bins that were the furthest from the mean and were again greater than or equal to 10%. Optimal policies without evidence are dependent upon the utility function. These results can be seen in figure 5.8.

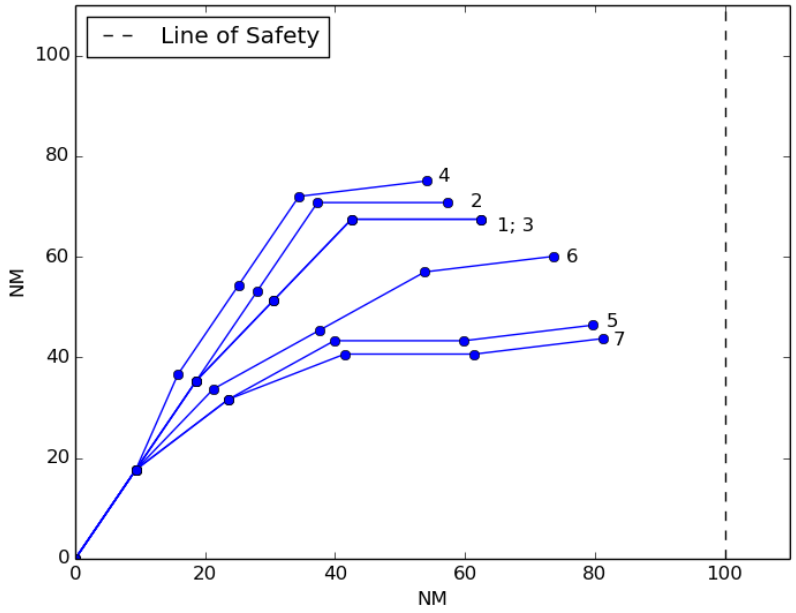

Figure 5.8: Courses from updating with evidence from both SAS and crack length individually and in combination with evidence in bins with a greater than or equal to 10% posterior probability. The utility function placed greater weight on the advancement term with $\alpha = 1, \beta = 1.2$.

In the event of damage, the optimal heading towards a line of safety is never one that is direct when the ship is operating in anything but calm seas. Without any evidence and immediately following the occurrence of damage, the optimal heading for the both utility functions with $\alpha = 1$, $\beta = 1$ and $\alpha = 1$, $\beta = 1.2$, is 63 degrees.

In all results, it was observed that high or low crack length and SAS measurements influenced heading directness individually and together, demonstrating effective data fusion. A trade space is evidence from tables 5.4, and 5.6 where greater crack length is observed with greater advancement and vice-versa. In all cases, the fusion of the crack measurement

data and SAS measurement data produced more suitable courses than with evidence from either crack length or SAS alone. Evidence from greater than 10% posterior probability and adjacent to the mean show that the greater the distance from the mean of the provided evidence, the greater the network reaction in the form of optimal heading selection. Evidence sets adjacent to the mean were consistently less volatile when compared to the no evidence case than those sets with greater than or equal to 10% posterior probability. This means that the most direct and least direct paths were observed in the 10% posterior evidence sets.

The network's tunability with utility function construction using α and β was demonstrated when β was adjusted to be 1.2 instead of 1. In figure 5.8 all courses are more aggressive than those with the same sets of evidence in figure 5.6. When the utility function weight was greater on the advancement term with an increased β, an interesting phenomenon occurred when updating with low measurements. Because the network decisions provided a course that resulted in significant crack growth, to satisfy the increased weight on advancement, the course for the 4^{th} timestep was more conservative than that provided without evidence.

5.5 Conclusions

An approach to provide damage decision support to course headings accounting for structural degradation in the form of crack propagation was presented. DID updating was performed using visual crack length inspection with uncertainty and SAS measurement of extreme stresses. Five timesteps at two hours each were evaluated. By providing synthetic evidence, both close to and far from the mean, the optimal courses were shown to become more or less direct. The ability to fuse the SAS and crack length evidence was demonstrated, as the most direct and least direct courses were observed with both sets of evidence provided. The ability to tune the optimal route was shown by varying the utility function weights.

The results presented herein demonstrate the ability of a DID to provide real-time damage decision support accounting for structural health and fusing multiple pieces of evidence. This approach could easily be scaled to include other degradation modes and additional pieces of structural health evidence. Extension of this approach could provide crew with much needed damage decision support surrounding the structural reliability and its effect on optimal course selection.

CHAPTER 6

Conclusions

6.1 Summary

The objective of this body of work was to provide a method for interpreting evidence of structural degradation gathered with uncertainty for structural reliability model updating and decision support. Marine structures operate in a harsh environment and fatigue life estimates are subject to significant uncertainty. Visual evidence from common-cause degradation mechanisms such as fatigue crack initiation are imperfect and incomplete. When integrated into a data to decision framework capable of fusing and interpreting uncertain data, the resulting information was demonstrated to be of greater value than the sum of the parts. The novel Bayesian network based data fusion frameworks developed within this body of work provide decision makers with information on the structural health of the vessel during its lifecycle as well as after sustaining damage from an incident. In both cases the frameworks were demonstrated to provide both more accurate prognoses and decision support.

Beyond fusion of visual degradation cues, integrating data from sensing instrumentation further increases the updated model's accuracy and the produced information's value. During the development of the novel Bayesian network fusion framework, it was recognized that the state of the art strain sensing options were not being adopted by the marine community due to incompatibilities surrounding data acquisition and energy storage. Rout-

ing power and data acquisition cables through these spaces is cost prohibitive. Wireless solutions struggle with signal passage through the watertight spaces. The Strain Amplification Sensor, a cost-effective stand-alone solution, was invented and developed herein as a sensing solution for marine structures. Its data is of use to both data fusion frameworks developed: through life degradation assessment for inspections and post-damage path planning.

Two case studies were conducted using simulated data to validate the proposed frameworks. In the case of the fleet fatigue model, posterior probability distribution characteristics were compared to the true values from the simulated data. It was discovered that data from permanent set and fatigue crack initiation were capable of being fused to produce more accurate updated models. For the route planning model, validity of the results was ascertained from comparison of the different produced policies reconciled with the nature of the evidence. Successful fusion of data from the Strain Amplification Sensor and crack length was observed to produce more suitable course policies. Both case studies' results indicated successful data fusion and decision support capabilities.

Testing of the SAS was performed for calibration, repeatability, and manufacturing variability assessment. In environment tests were also conducted onboard a U.S.C.G. RBM and during a laboratory welding process. The SAS design configuration tested was $123\ mm$ x $84\ mm$ x $14\ mm$ and was found capable of detecting displacements on the order of $1\ \mu m$. Repeatability testing was conducted over 50 cycles and indicated that SAS's variability and accuracy and repeatability increased with the number of cycles. For the five sensors 3D printed in a batch and evaluated for manufacturing variability, the deviations between measurements were sufficiently low. While onboard the U.S.C.G. RBM, SAS successfully demonstrated its ability to function on a marine structure. Weld process testing proved SAS capable of visually displaying, in real-time and without power or a data acquisition system, the strain experienced due to weld distortion. Testing to this point has demonstrated that the SAS is capable of suitably reliable and accurate measurement needed for fatigue

assessment onboard marine vessels and for weld distortion characterization during vessel fabrication.

6.2 Contributions

A novel framework capable of not only data fusion, but also data to decision support has been presented and developed herein. Data gathered from only visual observations during inspection has been demonstrated to provide effective updating to the data fusion framework to increase the accuracy of the underlying reliability model for decision support. The framework was demonstrated to provide decision support for inspection extent as well as route planning after damage, both of which are novel solutions themselves. To supplement the visual updating data available to the network, a novel strain gauge, the Strain Amplification Sensor was invented as a cost-effective sensing technology for marine structures.

6.3 Recommendations for Future Work

The fleet fusion framework should be extended to model the structure on a more global sense. Model construction and demonstration to this point has been focused on a single grillage. Observed deterioration on the port side of ship can be fused with observations on the starboard for example. Both port and starboard structures are subject to the same cyclic loads which are the primary driver of structural fatigue. Since a single grillage is a poor litmus test of an entire ship's degradation state, the increased modeling scale would provide better updating accuracy and thereby increased inspection decision support credibility.

The accuracy of the updated network's within could potentially be improved via different post processing techniques. It would be worth considering dropping structural reliability model combinations with the lowest posterior probabilities after asserting evidence. Though the most probable states would remain the same, the shape of the distribution would change proportional to the number of dropped combinations (bins). This could effectively

reduce the standard deviation error that was difficult to reduce throughout this body of work.

A significant difficultly with the route planning framework lies with the size of CPTs growing exponentially with the timestep number if the network is encoding the position of the vessel. Instead a line of safety objective was introduced that did not require the knowledge of the vessel position for decision-making. If the navigable space was modeled with obstacles or an objective point were included, the location of the vessel would need to be encoded. If a framework existed where CPTs can be populated in real-time based upon prior decision, the CPT exponential growth problem could be alleviated, paving the way for route planning inclusive of position encoding. Additionally, the framework solution algorithm should have inference search algorithms capable of handling multiple decision nodes with edges into a single utility function. The greedy algorithm used was incapable of considering more than one decision node into each utility function without converging on local optimums. A framework including these capabilities would be an extension to this work that could greatly increase the utility of the route planning fusion framework.

All data fusion network testing was conducted with simulated data. Further validation with data acquired from either laboratory testing or real world vessels should be completed. Laboratory testing could be from a grillage as was examined in a case study presented herein, or another coupled structure with understood fatigue properties. The challenge in getting real world data is the level of required detail. Conventional inspection logs do not provide adequate details about the structural condition.

The Strain Amplification Sensor requires further testing to prove its operational envelope and capabilities. Evaluation for temperature changes and across a spectrum of strain rates have not yet been conducted. Additionally, the effect of humidity on the measurement accuracy and repeatability have not yet been evaluated. Finally, extensions to record the strain time history and the maximum experienced values should be further explored. Conceptual designs exist and are feasible but have not yet been protected.

BIBLIOGRAPHY

G. Ashe. Naval Ship Design. In *Proceedings of the 17th International Ship and Offshore Structures Congress*, volume 2, pages 259–307, Seoul, Korea, 2009.

Bilal M. Ayyub, Karl A. Stambaugh, Timothy A. McAllister, Gilberto F. de Souza, and David Webb. Structural Life Expectancy of Marine Vessels: Ultimate Strength, Corrosion, Fatigue, Fracture, and Systems. *ASCE-ASME J. Risk and Uncert. in Engrg. Sys., Part B: Mech. Engrg.*, 1(1):011001, February 2015. ISSN 2332-9025. doi: 10.1115/1.4026396. URL http://risk.asmedigitalcollection.asme.org/article.aspx?doi=10.1115/1.4026396.

David Bak. Rapid prototyping or rapid production? 3d printing processes move industry towards the latter. *Assembly Automation*, 23(4):340–345, December 2003. ISSN 0144-5154. doi: 10.1108/01445150310501190. URL http://www.emeraldinsight.com/doi/abs/10.1108/01445150310501190.

Jean-Franois Balmat, Frdric Lafont, Robert Maifret, and Nathalie Pessel. A decision-making system to maritime risk assessment. *Ocean Engineering*, 38(1):171–176, January 2011. ISSN 00298018. doi: 10.1016/j.oceaneng.2010.10.012. URL http://linkinghub.elsevier.com/retrieve/pii/S0029801810002271.

Robert Bogue. 3d printing: the dawn of a new era in manufacturing? *Assembly Automation*, 33(4):307–311, September 2013. ISSN 0144-5154. doi: 10.1108/AA-06-2013-055. URL http://www.emeraldinsight.com/doi/abs/10.1108/AA-06-2013-055.

Marcus Bole. Introducing Damage Structural Assessment to Onboard Decision Support Tools. In *COMPIT*, Italy, 2007. COMPIT.

F. Calabrese, A. Corallo, A. Margherita, and A. A. Zizzari. A knowledge-based decision support system for shipboard damage control. *Expert Systems with Applications*, 39(9):8204–8211, July 2012. ISSN 0957-4174. doi: 10.1016/j.eswa.2012.01.146. URL http://www.sciencedirect.com/science/article/pii/S0957417412001662.

Bradley P. Carlin, Thomas A. Louis, and Bradley P. Carlin. *Bayesian methods for data analysis*. Chapman & Hall/CRC texts in statistical science series. CRC Press, Boca Raton, 3rd ed edition, 2009. ISBN 978-1-58488-697-6.

M Collette and A Incecik. An approach for reliability-based fatigue design of welded joints on aluminunn high-speed vessels. *Journal of Ship Research*, 50(1):85–98, March 2006.

M Collette and J Lynch. Lifecycle Support for Naval Ships based on Structural Health Monitoring: Data to Decisions Strategies. Arlington, VA, 2013.

Matthew Collette. Hull Structures as a System: Supporting Lifecycle Analysis: Hull Structures as a System. *Naval Engineers Journal*, 123(3):45–55, September 2011. ISSN 00281425. doi: 10.1111/j.1559-3584.2011.00329.x. URL http://www.ingentaconnect.com/content/asne/nej/2011/00000123/00000003/art00011.

G.F. Cooper. The computational complexity of probabilistic inference using bayesian belief networks. *Artificial Intellifence*, 42(2-3):393–405, March 1990.

Alberto Dec, Dan M. Frangopol, and Benjin Zhu. Reliability and redundancy assessment of ships under different operational conditions. *Engineering Structures*, 42:457–471, September 2012. ISSN 0141-0296. doi: 10.1016/j.engstruct.2012.04.017. URL http://www.sciencedirect.com/science/article/pii/S014102961200212X.

Tom Devine. Using and Interpreting the Bayesian Optimization Algorithm to Improve Design of Marine Structures, 2014.

Ove Ditlevsen and H. O. Madsen. *Structural reliability methods*. Wiley, Chichester ; New York, 1996. ISBN 978-0-471-96086-7.

You Dong and Dan M. Frangopol. Risk-informed life-cycle optimum inspection and maintenance of ship structures considering corrosion and fatigue. *Ocean Engineering*, 101:161–171, June 2015. ISSN 00298018. doi: 10.1016/j.oceaneng.2015.04.020. URL http://linkinghub.elsevier.com/retrieve/pii/S0029801815000955.

Dan M. Frangopol and Mohamed Soliman. Life-cycle of structural systems: recent achievements and future directions. *Structure and Infrastructure Engineering*, 12 (1):1–20, January 2016. ISSN 1573-2479, 1744-8980. doi: 10.1080/15732479.2014.999794. URL http://www.tandfonline.com/doi/full/10.1080/15732479.2014.999794.

Wolfgang Fricke. Fatigue Analysis of Welded Joints: State of Development. *Marine Structures*, 16:185–200, 2003.

G. Gagliardi, M. Salza, S. Avino, P. Ferraro, and P. De Natale. Probing the Ultimate Limit of Fiber-Optic Strain Sensing. *Science*, 330(6007):1081–1084, November 2010. ISSN 0036-8075, 1095-9203. doi: 10.1126/science.1195818. URL http://www.sciencemag.org/cgi/doi/10.1126/science.1195818.

gCaptain. MOL Comfort Report Coming Soon - ClassNK. *gCaptain*, 2014. URL http://gcaptain.com/mol-comfort-report-coming-soon-classnk/.

J. Goyet, A. Rouhan, E. L'Haridon, and L. Gomes. Probabilistic system approach for risk based inspection of FPSOs. In *Proceedings of the Annual Offshore Technology Conference*, volume 2, pages 1154–1163, 2011. ISBN 978-1-61839-277-0.

Mark Groden and Matthew Collette. Bayesian Networks for Model Updating and Inspection Support of Marine Structures Subject to Fatigue. In *12th International Conference on Applications of Statistics and Probability in Civil Engineering*, Vancouver, 2015.

Mark Groden and Matthew Collette. Fusing Structural Damage Measurements for Route Planning Decision Support. *Marine Structures*, Manuscript submitted for publication, 2016a.

Mark Groden and Matthew Collette. Strain Amplification Sensor, January 2016b.

Mark Groden, Liu Liu, and Matthew Collette. Fatigue Life Updating for Vessel Fleets. In *IALCCE 2016*, volume Under review, Delft, Netherlands, 2016.

C. Guedes Soares and Y. Garbatov. Reliability of maintained ship hulls subjected to corrosion and fatigue under combined loading. *Journal of Constructional Steel Research*, 52(1):93–115, October 1999. ISSN 0143974X. doi: 10.1016/S0143-974X(99)00016-4. URL http://linkinghub.elsevier.com/retrieve/pii/S0143974X99000164.

Emil Julius Gumbel. *Statistics of extremes*. Dover Publications, Mineola, N.Y., 2004. ISBN 978-0-486-15448-0.

Haksoo Choi, Sukwon Choi, and Hojung Cha. Structural Health Monitoring system based on strain gauge enabled wireless sensor nodes. pages 211–214. IEEE, June 2008. ISBN 978-4-907764-31-9. doi: 10.1109/INSS.2008.4610888.

Ernesto Heredia-Zavoni, Francisco Silva-Gonzalez, and Roberto Montes-Iturrizaga. Reliability Analysis of Marine Platforms Subject to Fatigue Damage for Risk Based Inspection Planning. *Journal of Offshore Mechanics and Arctic Engineering*, 130(4):041001–1 – 041001–9, 2008. ISSN 08927219. doi: 10.1115/1.2904945. URL http://OffshoreMechanics.asmedigitalcollection.asme.org/article.aspx?articleid=1472636.

Li-fen Hu, Kun Ma, and Zhuo-shang Ji. A MH method-based decision support system for flooding emergencies onboard warship. *Ocean Engineering*, 58:192–200, January 2013. ISSN 00298018. doi: 10.1016/j.oceaneng.2012.10.012. URL http://linkinghub.elsevier.com/retrieve/pii/S0029801812003885.

T. D. Huang, Michael Harbison, Lee Kvidahl, David Niolet, John Walks, J. P. Christein, Mark Smitherman, Mark Phillippi, Pingsha Dong, Larry DeCan, Vince Caccese, Paul Blomquist, David Kihl, Rick Wong, Matthew Sinfield, Natale Nappi, James Gardner, Catherine Wong, Michael Bjornson, and Allen Manuel. Reduction of Overwelding and Distortion for Naval Surface Combatants. Part 2: Weld Sizing Effects on Shear and Fatigue Performance. *Journal of Ship Production and Design*,

32(1):21–36, February 2016. ISSN 21582866, 21582874. doi: 10.5957/JSPD.32.1.140024. URL http://www.ingentaselect.com/rpsv/cgi-bin/cgi?ini=xref&body=linker&reqdoi=10.5957/JSPD.32.1.140024.

Owen F Hughes, Jeom Kee Paik, and Dominique Beghin. *Ship structural analysis and design*. Society of Naval Architects and Marine Engineers, Jersey City, N.J., 2010. ISBN 9780939773787 0939773783 9780939773824 0939773821.

Gareth James, Daniela Witten, Trevor Hastie, and Robert Tibshirani, editors. *An introduction to statistical learning: with applications in R*. Number 103 in Springer texts in statistics. Springer, New York, 2013. ISBN 9781461471370.

F.V. Jensen, S.L. Lauritzen, and K.G. Olesen. Bayesian updating in causal probabilistic networks by local computations. *Computational Statistics Quarterly*, 4:269–282, 1990.

Rudolph Kalman. A New Approach to Linear Filtering and Prediction Problems. *Transactions of the ASME – Journal of Basic Engineering*, 82(Series D):35–45, 1960.

M.B. Kane, C. Peckens, and J.P. Lynch. Design and selection of wireless structural monitoring systems for civil infrastructures. In *Sensor Technologies for Civil Infrastructures*, pages 446–479. Elsevier, 2014. ISBN 978-0-85709-432-2. URL http://linkinghub.elsevier.com/retrieve/pii/B9780857094322500164.

Ralph L. Keeney and Howard Raiffa. *Decisions with multiple objectives: preferences and value tradeoffs*. Cambridge University Press, Cambridge [England] ; New York, NY, USA, 1993. ISBN 978-0-521-44185-8 978-0-521-43883-4.

Uffe B Kjaerulff and Anders L Madsen. *Bayesian networks and influence diagrams: a guide to construction and analysis*. Springer, New York, 2008. ISBN 9780387741000 0387741003.

Lawrence A. Klein. *Sensor and data fusion: a tool for information assessment and decision making*. Number 138 in PM. SPIE Press, Bellingham, Wash, 2. printing edition, 2007. ISBN 978-0-8194-5435-5.

Ole J. D Kristensen and Forskningscenter Riso. *Fundamentals for remote structural health monitoring of wind turbine blades - a preproject, annex E: full-scale test of wind turbine blade, using sensors and NDT*. Riso National Laboratory, Roskilde, 2002. ISBN 978-87-550-3034-3.

S.L. Lauritzen and D.J. Spiegelhalter. Local Computations with Probabilities on Graphical Structures and Their Application to Expert Systems. *Journal of the Royal Statistical Society. Series B (Methodological)*, 50:157–224, 1988.

J Lou, H Yin, and B Li. Path planning for automated guided vehicles system via interactive dynamic influence diagrams with communication. In *9th IEEE International Conference on Control and Automation*, Santiago; Chile, 2011. IEEE. ISBN 978-1-4577-1475-7.

Anders Madsen and Finn Jensen. Lazy evaluation of symmetric Bayesian decision problems. In *UAI'99 Proceedings of the Fifteenth conference on Uncertainty in artificial intelligence*, pages 382–390, Stockholm, Sweden, 1999.

N.R. Mandal and P. Biswas. A review on development of weld induced distortion analysis. volume 2, pages 901–908, Lisbon, 2011. CRC press. ISBN 978-0-415-69808-5 978-0-415-62888-4 978-0-415-62891-4 978-0-203-10518-4.

Alaa E. Mansour. Extreme Value Distributions for Linear and Non-Linear Systems and Applications to Marine Structures. In Janos Galambos, James Lechner, and Emil Simiu, editors, *Extreme Value Theory and Applications*, pages 61–76. Springer US, Boston, MA, 1994. ISBN 978-1-4613-3640-2 978-1-4613-3638-9.

J.J. McCullagh, T. Galchev, R.L. Peterson, R. Gordenker, Y. Zhang, J. Lynch, and K. Najafi. Long-term testing of a vibration harvesting system for the structural health monitoring of bridges. *Sensors and Actuators A: Physical*, 217:139–150, September 2014. ISSN 09244247. doi: 10.1016/j.sna.2014.07.003. URL http://linkinghub.elsevier.com/retrieve/pii/S0924424714003331.

Ferry P.W. Melchels, Jan Feijen, and Dirk W. Grijpma. A review on stereolithography and its applications in biomedical engineering. *Biomaterials*, 31(24):6121–6130, August 2010. ISSN 01429612. doi: 10.1016/j.biomaterials.2010.04.050. URL http://linkinghub.elsevier.com/retrieve/pii/S0142961210005661.

Van Der Meulen and R. Hageman. Fatigue predictions using statistical inference within the monitas II project. In *Proceedings of the International Offshore and Polar Engineering Conference*, Anchorage, AK, 2013.

Kevin Murphy. *Dynamic Bayesian Networks: Representation, Inference and Learning*. PhD Thesis, Berkeley, 2002.

Jeom Kee Paik. *Ultimate limit state design of steel plated structures*. J. Wiley, Chichster, England ; Hoboken, NJ, 2003. ISBN 0471486329.

P T Pedersen and J J Jensen. Estimation of hull girder vertical bending moments including non-linear and flexibility effects using closed form expressions. *Proceedings of the Institution of Mechanical Engineers, Part M: Journal of Engineering for the Maritime Environment*, 223(3):377–390, March 2009. ISSN 1475-0902, 2041-3084. doi: 10.1243/14750902JEME143.

Stuart J. Russell, Peter Norvig, and Ernest Davis. *Artificial intelligence: a modern approach*. Prentice Hall series in artificial intelligence. Prentice Hall, Upper Saddle River, 3rd ed edition, 2010. ISBN 978-0-13-604259-4.

L. Salvino and M. Collette. Monitoring Marine Structures, 2009.

L. Salvino, C. Farrar, J.P. Lynch, and T.F. Brady. Multi-tiered sensing and data processing for monitoring ship structures. In *Proceeding of the High Performance Marine Vehicles Symposium*, Linthicum, Maryland, 2009. American Society of Naval Engineers.

T.A. Santos and C. Guedes Soares. Determininstic and probabilistic methods applied to damage stability. *Maritime Engineering and Technology*, pages 1297–1312, 2011.

Ross Shachter. Probabilistic inference and influence diagrams. *Operations Research*, 36 (4):589–604, 1988.

Joseph Edward Shigley. *Mechanical engineering design: 5th edition.* Mcgraw-Hill Classic, [S.l.], 1989. ISBN 0073027189 9780073027180.

C.Guedes Soares and A.P Teixeira. Structural reliability of two bulk carrier designs. *Marine Structures*, 13(2):107–128, March 2000. ISSN 09518339. doi: 10.1016/S0951-8339(00)00004-6. URL http://linkinghub.elsevier.com/retrieve/pii/S0951833900000046.

J.D. Sorensen. Reliability-based planning of inspection, operation and maintenance for offshore oil & gas structures and wind turbines. In *1st International Conference of Maritime Technology and Engineering*, Lisbon, 2011.

R. I. Stephens and H. O. Fuchs, editors. *Metal fatigue in engineering*. Wiley, New York, 2nd ed edition, 2001. ISBN 978-0-471-51059-8.

Daniel Straub. Stochastic modeling of deterioration processes through dynamic bayesian networks. *Journal of Engineering Mechanics*, 135(10):1089–1099, 2009.

Daniel Straub and Armen Der Kiureghian. Bayesian Network Enhanced with Structural Reliability Methods: Methodology. *Journal of Engineering Mechanics*, 136(10): 1248–1258, October 2010. ISSN 0733-9399, 1943-7889. doi: 10.1061/(ASCE)EM.1943-7889.0000173. URL http://ascelibrary.org/doi/abs/10.1061/%28ASCE%29EM.1943-7889.0000173.

Alfred. Strauss and Dan M. Frangopol. *Life-cycle and sustainability of civil infrastructure systems proceedings of the third International Symposium on Life-Cycle Civil Engineering, Hofburg Palace, Vienna, Austria, October 3-6, 2012*. CRC Press, [S.l.], 2013. ISBN 978-0-415-62126-7 0-415-62126-7. URL http://marc.crcnetbase.com/ISBN/978-0-415-62126-7.

Christopher J. Stull, Christopher J. Earls, and Phaedon-Stelios Koutsourelakis. Model-based structural health monitoring of naval ship hulls. *Computer Methods in Applied Mechanics and Engineering*, 200(912):1137–1149, February 2011. ISSN 0045-7825. doi: 10.1016/j.cma.2010.11.018. URL http://www.sciencedirect.com/science/article/pii/S0045782510003427.

M Tammer and M.L. Kaminski. Fatigue oriented risk based inspection and structural health monitoring of FPSOs. In *Proceedings of the International Offshore and Polar Engineering Conference*, Anchorage, AK, 2013.

J.A. Tatman and R.D. Shachter. Dynamic programming and influence diagrams. *IEEE Transactions on Systems, Man, and Cybernetics*, 20(2):365–379, April 1990. ISSN

00189472. doi: 10.1109/21.52548. URL http://ieeexplore.ieee.org/lpdocs/epic03/wrapper.htm?arnumber=52548.

M. L. Wang, Jerome P. Lynch, and H. Sohn, editors. *Sensor technologies for civil infrastructures*. Number number 55, 56 in Woodhead Publishing series in electronic and optical materials. Elsevier, Woodhead Publishing, Amsterdam, 2014. ISBN 9781782422440.

Yusuf Yagci, Steffen Jockusch, and Nicholas J. Turro. Photoinitiated Polymerization: Advances, Challenges, and Opportunities. *Macromolecules*, 43(15):6245–6260, August 2010. ISSN 0024-9297, 1520-5835. doi: 10.1021/ma1007545. URL http://pubs.acs.org/doi/abs/10.1021/ma1007545.

TingHua Yi, HongNan Li, and Ming Gu. Full-scale measurements of dynamic response of suspension bridge subjected to environmental loads using GPS technology. *Science China Technological Sciences*, 53(2):469–479, February 2010. ISSN 1674-7321, 1869-1900. doi: 10.1007/s11431-010-0051-2. URL http://link.springer.com/10.1007/s11431-010-0051-2.

J. Zhu, M. Groden, and M Collette. Bayesian Updating of Marine Structrual Reliability Models Based on In-Service Measurements. In *The 6th International Conference on Structural Health Monitoring of Intelligent Infrastructure*, Hong Kong, 2013.

Jiandao Zhu and Matthew Collette. A dynamic discretization method for reliability inference in Dynamic Bayesian Networks. *Reliability Engineering & System Safety*, 138: 242–252, June 2015. ISSN 09518320. doi: 10.1016/j.ress.2015.01.017. URL http://linkinghub.elsevier.com/retrieve/pii/S0951832015000277.

Boris A. Zrate, Juan M. Caicedo, Jianguo Yu, and Paul Ziehl. Bayesian model updating and prognosis of fatigue crack growth. *Engineering Structures*, 45:53–61, December 2012. ISSN 01410296. doi: 10.1016/j.engstruct.2012.06.012. URL http://linkinghub.elsevier.com/retrieve/pii/S014102961200315X.